

Utah State University

DigitalCommons@USU

All Graduate Theses and Dissertations


Graduate Studies

5-2021

Developing Advanced Electrodes and Electrolytes for Energy Storage Beyond Li Ion Batteries

Kevin V. Nielson
Utah State University

Follow this and additional works at: <https://digitalcommons.usu.edu/etd>

 Part of the [Chemistry Commons](#)

Recommended Citation

Nielson, Kevin V., "Developing Advanced Electrodes and Electrolytes for Energy Storage Beyond Li Ion Batteries" (2021). *All Graduate Theses and Dissertations*. 8080.
<https://digitalcommons.usu.edu/etd/8080>

This Dissertation is brought to you for free and open access by the Graduate Studies at DigitalCommons@USU. It has been accepted for inclusion in All Graduate Theses and Dissertations by an authorized administrator of DigitalCommons@USU. For more information, please contact digitalcommons@usu.edu.



DEVELOPING ADVANCED ELECTRODES AND ELECTROLYTES FOR
ENERGY STORAGE BEYOND LI ION BATTERIES

By

Kevin V. Nielson

A dissertation submitted in partial fulfillment
of the requirements for the degree

of

DOCTOR OF PHILOSOPHY

in

Chemistry

Approved:

Tianbiao Liu, Ph.D.
Major Professor

Lisa M. Berreau, Ph.D.
Committee Member

Alexander I. Boldyrev, Ph.D.
Committee Member

Robert S. Brown, Ph.D.
Committee Member

Jixun Zhan, Ph.D.
Committee Member

D. Richard Cutler, Ph.D.
Interim Vice Provost of
Graduate Studies

UTAH STATE UNIVERSITY
Logan, Utah

2021

Copyright © Kevin V. Nielson 2021

All Rights Reserved

ABSTRACT

Developing Advanced Electrodes and Electrolytes
for Energy Storage Beyond Li Ion Batteries

by

Kevin V. Nielson, Ph.D. of Science

Utah State University, 2021

Major Professor: Dr. Tianbiao Liu
Department: Chemistry and Biochemistry

Since the first commercialization of the Li-ion battery in 1990, we have seen new possibilities in technological advancements such as portable electronics (smart phones, tablets) and the ongoing electrification of motor vehicles. Current state of the art cathode active materials ($\text{LiNi}_x\text{Mn}_y\text{Co}_z\text{O}_2$) have reached a bottleneck in performance and contain the toxic, strategic metal Co. Metal organic frameworks (MOFs) have received ever increasing attention over the past decade as a viable alternative due to their inherent high degree of tunability with redox active metals and/or ligands. Additionally, MOFs have been rationally designed to withstand harsh chemical or electrochemical environments which are advantageous properties for battery electrode materials. Sustainability is another concern due to increased demand coupled with ultra-low crustal abundance of Li resources. Ca has received increasing attention in recent years as alternatives to Li due high earth abundance and minimized hazards compared to Li. Ca ions are divalent as well bestowing high energy density on this metal as a possible anode active material for full cell batteries.

The contents of this dissertation will contain two sections:

1. A modified synthetic method was developed for MOFs materials made up of first row transition metals and the linker molecule 2,5-dihydroxy-1,4-benzoquinone. Materials were fully characterized chemically then subjected to more in-depth electrochemical characterization including solid state cyclic voltammetry, impedance spectroscopy, and extensive full cell battery tests. Materials with energy densities comparable to Li-ion and cycling stabilities exceeding all other MOFs cathodes were discovered. Ex-situ characterization of pristine and cycled electrode materials by SEM-EDS, X-ray diffraction including soft X-ray absorption experiments was used to determine redox mechanisms and modes of decay.

2. Multivalent ion Ca electrolytes were explored and improved by chemical or physical methods. Performances of electrolytes were monitored by cyclic voltammetry determination of coulombic efficiencies, overpotentials and other important metrics. Symmetric cell batteries and full cell batteries were tested to benchmark electrolyte stabilities for energy storage applications. Further analysis of electrodes and electrolytes by NMR, FTIR, SEM-EDS provided a better view of the electrolyte stability and solvent quality.

(173 pages)

PUBLIC ABSTRACT

Developing Advanced Electrodes and Electrolytes

for Energy Storage Beyond Li Ion Batteries

Kevin V. Nielson

Electric vehicles, smart phones, and portable computers are all powered by lithium-ion batteries. This is because Li-ion batteries can store more energy in less space than other battery technologies. Also, they are rechargeable and last for a long time. The most recent 2019 Nobel prize in chemistry was awarded to John Goodenough, M. Stanley Whittingham and Akira Yoshino “for the development of lithium-ion batteries”. Through their work, they have made possible cars that do not burn fossil fuels and phones that are wireless and portable. Not only can Li-ion power your phone, it is an incredibly efficient way to store energy from renewable sources such as wind, solar, or hydroelectric.

From the introduction of the Li-ion Battery into the public market until now the fundamentals of the battery technology have remained relatively the same. This means a metal oxide electrode containing Co is combined with a Li containing electrolyte. Both Co and Li are rare elements that have sustainability issues. Replacing these components could make batteries more energy dense and sustainable for future generations.

The first part of this work describes an improved synthetic method to make battery electrodes from renewable organic materials and earth abundant elements. These electrodes were found to provide energy densities rivaling those found in current Li-ion technologies. The electrodes featured in this work make use of a type of material called metal organic frameworks (abbreviated as MOFs). The MOFs in this work were found to work well for Li batteries and last for over 1000 cycles. Spectroscopic techniques were

used to prove that it is advantageous for both the metal and the organic component of the MOFs to store energy.

The other unsustainable component of the battery is the Li electrolyte. In this work Ca electrolytes were improved and developed. Ca is a highly abundant and nontoxic element that is found everywhere. These qualities make it a highly suitable alternative to Li. Ca electrolytes have different properties than Li. Here the very important contributions of the solvent used in the electrolyte are examined. Not very many Ca electrolytes currently work for batteries. In this dissertation a new working Ca electrolyte was discovered and fully tested for its ability to work in Ca batteries. Two full functioning Ca batteries were tested with different electrolytes and electrodes. These batteries are the most energy dense Ca batteries ever reported and are directly competitive with Li-ion batteries.

ACKNOWLEDGMENTS

I would like to offer my most sincere gratitude to my major advisor Dr. Liu for hosting me in his research group for the past 5 years. I would also like to thank my supervisory committee members for their continuous help toward my graduation progress. I would also like to thank my coworkers in the lab who shared so much of their experience with me. Finally, I would like to thank the university and the department of chemistry and biochemistry for keeping me on a teaching assistant scholarship that paid for my graduate studies.

Kevin V. Nielson

CONTENTS

	Page
ABSTRACT.....	iii
PUBLIC ABSTRACT	v
ACKNOWLEDGMENTS	vii
LIST OF TABLES.....	x
LIST OF FIGURES	xi
Chapter I Introduction.....	1
1-1. Background and motivation	1
1-2. Important parameters for rechargeable batteries and electrolytes	17
1-3. Dissertation scope.....	19
1-4. References	21
Chapter II A Strategic High Yield Synthesis of 2,5-Dihydroxy-1,4-benzoquinone Based MOFs.....	29
2-1. Abstract	29
2-2. Introduction	29
2-3. Experimental.....	31
2-4. Results and discussion	34
2-5. Conclusion.....	43
2-6. References	45
Chapter III Redox Active Ni-Quinone MOFs as A Novel Li Ion Intercalation Cathode	48
3-1. Abstract	48
3-2. Introduction	48
3-3. Experimental.....	50
3-4. Results and Discussion	55
3-5. Conclusions	65
3-6. Acknowledgements	65
3-7. References	68
Chapter IV A High Capacity Iron Quinone Metal Organic Framework Featuring Metal and Ligand Redox Processes for Li Metal Organic Batteries	73
4-1. Abstract	73
4-2. Introduction	73

4-3. Results and discussion.....	74
4-4. Conclusions	87
4-5. Experimental.....	88
4-6. References	97
 Chapter V Optimizing Calcium Electrolytes by Solvent Manipulation for Ca Batteries	 102
5-1. Abstract	102
5-2. Introduction	102
5-3. Results and discussion.....	104
5-4. Conclusions	113
5-5. Experimental.....	114
5-6. References	117
 Chapter VI Perflourinated Chelate Anion Raises the Voltage Stability for Ca Batteries	 121
6-1. Abstract	121
6-2. Introduction	121
6-3. Results and discussion.....	123
6-4. Conclusions	131
6-5. Experimental.....	131
6-6. References	137
 Chapter VII Conclusion	 141
Appendices	148
Appendix A. Tables and Figures	149
Appendix B. Copyright	153
Appendix C. Curriculum Vitae	153

LIST OF TABLES

	Page
Table 2-1 Price comparison for DAHQ vs DHBQ ligand as of March 20, 2019	44
Table 3-1 Fitting parameters for the Ni K-edge EXAFS spectra of LiNiDBQ _{1.5}	67
Table 4-1 EXAFS and XANES for LiFeDBQ _{1.5}	92
Table 5-1 Composition analysis of Li(1-2x)Ca(x)FePO ₄ by EDS and ICP-MS analysis. Values are listed as atomic ratios. Li cannot be detected by EDS, so values were estimated based on the assumption of charge balance.	113
Table 6-1 Crystal data and structure refinement for Ca-FPB	134
Table A-1 An overview of MOF cathodes to date.....	150
Table A-2 An overview of Ca electrolytes to date	152

LIST OF FIGURES

	Page
Figure 1-1. A comparison of gravimetric and volumetric capacity, reduction potentials and abundance for several metallic anodes	8
Figure 2-1. Flow chart for synthesis of (A) Literature reported $\text{NBu}_4\text{Ni}(\text{DHBQ})_{1.5}$. (B) Synthesis of $\text{NBu}_4\text{Ni}(\text{DHBQ})_{1.5}$ (C) Generation of $\text{NiDHBQ}(\text{H}_2\text{O})_2$	35
Figure 2-2. X-ray diffraction data obtained from samples prepared by facile synthesis compared to simulated patterns for (A) $\text{Ni}(\text{DHBQ})(\text{H}_2\text{O})_2$ prepared by room temperature reagent combination. And hot addition reactions presented here for (B) $\text{NBu}_4\text{Ni}(\text{DHBQ})_{1.5}$ and (C) $\text{NBu}_4\text{Fe}(\text{DHBQ})_{1.5}$	37
Figure 2-3. SEM and EDS analysis of $\text{NBu}_4\text{Ni}(\text{DHBQ})_{1.5}$ and $\text{NBu}_4\text{Fe}(\text{DHBQ})_{1.5}$	38
Figure 2-4. FT-IR absorbance spectra of A) $\text{NBu}_4\text{Ni}(\text{DHBQ})_{1.5}$ and B) $\text{NBu}_4\text{Fe}(\text{DHBQ})_{1.5}$	39
Figure 2-5. PXRD of $\text{NBu}_4\text{NiDHBQ}_{1.5}$ prepared with DABQ ligand in a sealed glass vial reactor compared to the simulated pattern	39
Figure 2-6. $\text{NBu}_4\text{CoDHBQ}_{1.5}$ and simulation prepared by the high temperature addition reaction presented in this work	39
Figure 2-7. PXRD of $\text{NBu}_4\text{NiCAN}_{1.5}$ prepared by high temperature addition reaction and simulation	41
Figure 2-8. PXRD of $\text{NBu}_4\text{NiFAN}_{1.5}$ prepared by high temperature addition reaction and simulation	41
Figure 2-9. ^1H NMR of $\text{NBu}_4\text{NiDABQ}_{1.5}$ in DMSO D6	42
Figure 2-10. ^1H NMR of $\text{NBu}_4\text{NiDHBQ}_{1.5}$ in DMSO D6	42
Figure 3-1. Schematic of (A) Synthesis of $\text{LiNiDBQ}_{1.5}$ MOFs. (B) Coordination sphere of the Ni center with labelled averaged Ni-O bond distances obtained from the EXAFS studies; (C) Coordination structural model showing one DBQ ligand bridging two Ni centers, Li (purple), Ni (green), C (black) and H (white); and (D) Three dimensional structure model of the $\text{LiNiDBQ}_{1.5}$ MOFs with Li^+ ion omitted for	

clarity. (E) SEM and element mapping images of LiNiDBQ_{1.5} MOFs. (F) TEM image of LiNiDBQ_{1.5} MOFs56

Figure 3-2. Spectroscopy of (A) Ni K-edge XANES spectra of the LiNiDBQ_{1.5} MOFs and Ni foil, Ni(OH)₂, and NiO(OH). (B) Ni K-edge EXFAS spectra of the LiNiDBQ_{1.5} MOFs: experimental spectrum, (black dotted curve) and fitted spectrum (red curve); (C) IR spectra of LiNiDBQ_{1.5} MOFs, Li₂DBQ, and H₂DQB; and (D) CV of LiNiDBQ_{1.5}58

Figure 3-3. (A) Rate performance from 0.1 to 1.6 C; (B) Representative charge/discharge curves at various C rates; (C) Initial and reversible discharging/charging profiles.; (D) Discharge capacity and coulombic efficiency over cycling number at 0.4 C, inset showing charge discharge curves at specified cycle numbers62

Figure 3-4. Nyquist plots for coin cells containing (A) H₂DBQ, (B) Li₂DBQ, and (C) LiNiDBQ_{1.5}. FTIR (D), and XANES (E) and EXFAS (F) studies of the charged and discharged states of the LiNiDBQ_{1.5} MOFs cathode63

Figure 3-5. PXRD Spectrum comparison of LiNiDBQ_{1.5} compared to the reference compound NBu₄NiDBQ_{1.5}66

Figure 3-6. Photography of charged and discharged electrodes in 1.0 M LiTFSI in 1:1 V:V DME:DOL of H₂DBQ, Li₂DQB, and LiNiDBQ_{1.5}66

Figure 3-7. Thermogravimetric analysis of LiNiDBQ_{1.5} under N₂ with 10 °C per minute ramp rate.67

Figure 3-8. Fourier-transformed Ni K-edge K-space EXFAS spectra of the LiNiDBQ_{1.5}67

Figure 4-1. Schematic of (A) High resolution SEM imaging of LiFeDBQ_{1.5} particle with 10 uM scale with inset showing EDX quantification of carbon, oxygen, and iron and EDX imaging shown to the right. (B) XPS integration of Fe. (C) X-ray absorption fine structure of LiFeDBQ_{1.5} and simulated best fit. (D) X-ray absorption near edge k-space spectra comparing rising energy of LiFeDBQ_{1.5} to reference materials FeO and Fe₂O₃. And (E) Mossbauer spectrum of pristine LiFeDBQ_{1.5} containing Fe(2+) in blue and Fe(3+) in red and sum spectra in black77

Figure 4-2. (A) Illustration of LiFeDBQ_{1.5} coordination sphere. (B) FTIR spectroscopy of LiFeDBQ_{1.5} and H₂DBQ. (C) Electron paramagnetic resonance spectra of LiFeDBQ_{1.5} in the appropriate range for the

radical ligand. (D) PXRD matching of LiFeDBQ_{1.5} (Black) to the simulated Powder pattern of NBu₄FeDBQ_{1.5}79

Figure 4-3. Electrochemistry including (A) CV of LiFeDBQ_{1.5}/Li from a three-electrode setup. (B) to (D) Battery data of the LiFeDBQ_{1.5}/Li battery. (B) Rate performance (C) Representative charge/discharge curves at various C rates; (D) Long term cycling for LiFeDBQ_{1.5} in the 1.5 to 3.9 V window; (E) Long term cycling for LiFeDBQ_{1.5} in the 1.8 to 4.0 V window with inset showing charge/discharge profile at different current densities82

Figure 4-4. Spectroscopy including (A) XANES rising energy at pristine, charged, and discharged states. (B) Mossbauer of charged state sample and (C) discharged state sample. (D) EIS Nyquist plot at different states of charge. (E-F) FT-IR spectra of Charged and Discharged state samples84

Figure 4-5. A Thermogravimetric analysis of LiFeDBQ_{1.5}92

Figure 4-6. Solid cyclic voltammetry set-up.....93

Figure 4-7. Mossbauer spectroscopy of LiFeDBQ_{1.5} and tabulated results.....93

Figure 4-8. Solid electrolyte cell cycling performance and charging/discharging voltage versus time curve.....95

Figure 4-9. XPS integration of Fe(2+)/Fe(3+) in different states of charge. Including XPS survey of different states of charge.95

Figure 4-10. SEM-EDS analysis of freshly prepared electrode96

Figure 5-1. Cyclic voltammetry of a 0.25 M Ca[B(hfip)₄]₂/DME electrolyte solution with a glassy carbon rod counter electrode and a Ca reference electrode for A) Glassy carbon working electrode with Coulombic efficiency shown. B) Al working electrode with three cycles of decreasing current shown.C) Cu working electrode with limited reversibility and oxidation stability. D) Pt working electrode with inset showing accumulation of charge and Coulombic efficiency.106

Figure 5-2. Cyclic voltammetry of a 0.25 M Ca[B(hfip)₄]₂/DGM electrolyte solution with glassy carbon rod counter electrode and a Ca reference electrode for A) Glassy Carbon working electrode. B) Al working electrode with inset showing accumulation of charge and Coulombic efficiency. C) Cu working electrode with Coulombic efficiency inset. D) Ptworking electrode with Coulombic efficiency inset. All samples were cycled at 100 mV/s scan rate.....107

Figure 5-3. Symmetric cell evaluation of $\text{Ca}[\text{B}(\text{hfiP})_4]_2$ in different solvents with Ca deposited on Cu serving as both electrodes for A) DGM, B) DME, C) THF. D) Test time and current density for the three cells, E) end cycling for DGM cell, and F) initial cycling of G) DGM cell.108

Figure 5-4. Post analysis by SEM and EDX elemental mapping of Cu current collectors from Ca|Ca symmetric cells for A) the cell using THF comprising mostly CaF_2 deposits, B) the cell using DME solvent with dendrites measured by a scale bar, and C) the cell using DGM solvent with smooth particle deposition morphology.110

Figure 5-5. Electrochemical performance of a Ca| FePO_4 rechargeable battery with a 0.25 M $\text{Ca}[\text{B}(\text{hfiP})_4]_2/\text{DGM}$ electrolyte at 10 mA/g for charging and discharging processes. A) Charging and discharging capacities and Coulombic efficiency. B) Representative charging/discharging curves of the seventh cycle. C) Charging/discharging Voltage profile over testing time.111

Figure 5-6. Cyclic voltammetry of 0.25M $\text{Ca}(\text{B}(\text{hfiP})_4)_2$ in THF solvent with a Pt working electrode. (A) Sweeping to negative 300 mV vs CA with 68% coulombic efficiency and 3.25 V anodic stability. (B) Scanning to negative 1.0 V vs Ca with a complete loss of reversibility. (C) Cyclic voltammetry of 0.25M $\text{Ca}(\text{B}(\text{hfiP})_4)_2$ in DME solvent with a Pt working electrode, GC counter electrode, and Ca reference electrode by sweeping to -700 mV vs Ca. Coulombic efficiency is shown in the insets with decreasing coulombic efficiency observed for increasingly negative CV sweeping voltages.112

Figure 5-7. SEM-EDS post analysis of the FePO_4 electrode.113

Figure 6-1. Synthesis and crystal structure for Ca-FPB123

Figure 6-2. Electrochemical analysis of a 0.8M Ca-FPB electrolyte by Cyclic voltammetry for ten cycles with Pt working, Ca reference, and glassy carbon rod counter electrodes. Scan rate 100 mV/s. Inset showing tenth cycle Coulombic efficiency. (A) Linear sweep voltammetry using labeled material as work electrode. (C) Reversible areal capacity on a Pt disc working electrode at 0.12 mA/cm² current density.125

Figure 6-3. Characterization of deposition products from Ca-FPB by SEM EDS of a SS substrate deposited to 1.2 mAh/cm². (A) EDS spectra, lower left, show Ca the major deposition product and (B) Powder X-ray diffraction comparing the Ca deposits (black)

to simulated spectra for CaF_2 (Blue) and Ca metal (orange)126

Figure 6-4. Battery tests with Ca-FPB using (A) a Ca|Ca symmetric cell tested at varying currents galvanostatically with polarization curve. Inset showing 500-hour longevity of the cell. And (B) A Ca| $\text{Fe}(\text{CN})_6$ battery cycled between 2.0 and 3.5 V at 15 mA/g with inset showing 5:5 voltage profile128

Figure 6-5. (A) Electrochemical desodiation process for $\text{NaFe}_2(\text{CN})_6$. (B) Charge/discharge profile taken from the first cycle for the Ca|Ca-FPB| $\text{Fe}_2(\text{CN})_6$ battery. (C) Post analysis of the $\text{Ca}_x\text{Fe}_2(\text{CN})_6$ electrode by scanning electron microscopy and electron dispersive spectroscopy. The electrode was harvested from the cell in the discharged (2.0 V) State. (D) Powder X-ray diffraction pattern of Prussian Blue electrodes that were pristine (blue), charged Galvanostatically to 4.0 V (orange), and discharged to 2.5 V in a Ca|Ca-FPB|PB cell (grey).129

Figure 6-6. (A-B)Cyclic voltammograms of 0.8 M Ca-FPB using a flooded Ca electrode setup i.e. working, counter, and reference electrodes were Ca metal. Scan rate 100 mV/s. (C) Cyclic voltammetry showing full voltage window -1.0 V to 5.0 V versus a Ca metal reference electrode. Scan rate 20 mV/s. (D) Electrochemical impedance spectroscopy Nyquist plot. Data were collected interim galvanostatic deposition stripping processes performed in figure 6-1D.....130

CHAPTER I

INTRODUCTION

1-1. Background and motivation

Conductive MOFs Electrodes

Li-ion batteries are highly energy dense systems that provide power to portable electronics and electric vehicles. The complete electrification of motor vehicles would represent a tremendous decrease in fossil fuel dependency.¹⁻³ Decreased use of fossil fuels is crucial to mitigating the hazardous effects of greenhouse gas concentrating in the atmosphere so long as the electricity is generated via renewable resources such as wind or solar.⁴⁻⁶ Fortunately for Li-ion batteries, due to their high energy density, they are also increasingly used as grid energy storage devices.⁷⁻⁸ A bottleneck has been reached in this technology; specifically regarding the transition metal oxides (e.g. LiCoO₂) that occupy the seat as state of art electrode active materials in the positive terminal of the battery (cathode).⁹⁻¹⁰ There are also ethical concerns related to Co mining.¹¹⁻¹² Redox active organic cathode materials represent renewable, abundant alternatives to transition metal oxides.¹³⁻¹⁶ The most significant obstacle to realizing organic powered batteries is the tendency of organic molecules to dissolve in the presence of organic-solvent based electrolytes, thereby losing contact with the current collector and becoming a spectator within the electrochemical cell.¹⁶ The second most significant obstacle with organic electrodes comes from the insulating nature of organic molecules which diminishes the cycling ability of batteries.¹⁴

An effective strategy to overcome these obstacles is to incorporate redox active organic molecules into bulk materials that are both stable in organic electrolytes and

maintain favorable electron transport with repeated cycling.¹ Metal Organic Frameworks (MOFs) represent a highly tunable class of bulk materials with regards to porosity, conductivity, and redox activity.^{14, 17-21} MOFs can be composed of any metal ion and bridging organic moiety making the number of possible MOFs materials limitless. MOFs for use as Li-ion battery cathode materials would ideally have the following properties; 1. High electronic conductivity to facilitate efficient electron mobility, 2. High porosity to facilitate ion migration through the host material, 3. High energy density – meaning the number of reversible redox reactions is not dwarfed by the mass or volume of the materials repeating units. 4. Contain only first row, earth abundant transition metals adequate to meet the global demand for environmentally benign organic based energy storage devices.

The structure tunability and built-in porosity of MOFs makes them promising electrode materials to host metal ions. However, the use of redox active MOFs as metal ion (such as Li⁺ and Na⁺) storage electrode materials still remains largely underdeveloped since first MOFs electrode report by Li et al. of the Zn based MOF-117 as an anode in 2006.¹⁸ Li's report and over 50 studies in the following decade described MOFs low voltage anode materials that utilized irreversible electrochemical conversion reactions.²² Since then, MOFs anode materials based on Co₂(OH)BDC and Co/hexaminebenzene have demonstrated promising prospects including improved charge capacities and relatively stable cycling performance.^{20, 23-24} Nevertheless, the development of MOFs cathode materials is still a forbidding challenge as reported MOFs cathode materials only demonstrated limited capacities (< 150 mAh/g) and unsatisfactory cycling performance (< 100 cycles). In addition, reported MOFs materials primarily

employ metal based redox activity and do not fully take advantage of the structural features of MOFs materials such as structural tunability, intercalation properties, and ligand based multi-redox processes.

Most of reported MOFs cathodes only use metal based one electron redox activity. Specific examples of metal-only redox mechanisms are found in the well-known MIL-53 and MIL-68 MOFs studied by Ferey' et al.²⁵⁻²⁶ These were the first examples of MOFs cathodes having reversible redox reactions. Both examples made use of MOFs containing Fe nodes and benzene dicarboxylate struts. Only the Fe^{2+/3+} mechanism was found to contribute to the capacity; thus, their capacities were low (< 100 mAh/g, <0.6 e⁻/Fe) as ligands were dead materials. This study helped to demonstrate MOF materials can intercalate ions with quasi-reversible (<70% Coulombic efficiency) electrochemistry without decomposition of the host framework as in previous studies. This type of MOF utilized the Fe^{2+/3+} mechanism where up to 60 percent capacity utilization was achieved. Materials designed with greater electronic and ionic conductivities was proposed to improve the overall low Coulombic efficiencies and capacity utilization. Regardless of certain shortcomings, these preliminary results piqued interest to develop other metal Ligand systems that may not function by decomposition or exchange reactions.²⁷

There have been only a few examples of MOFs electrode materials using ligand based redox activity. Among them, the Cu(2,7-AQDC) MOFs represents the first MOFs cathode utilizing the two-electron redox process of its bridging dicarboxylate anthraquinone ligand.²⁸ In 2014 Zhang, Yoshikawa et al introduced a 2D MOF Cu(2,7-AQDC) as a positive li-ion electrode material. Anthraquinones are redox active via the quinone/enolate facile mechanism and have already received widespread investigation in

energy storage devices such as redox flow and static batteries.²⁹ Incorporating anthraquinone linkers into a Cu^{2+} node MOF material allowed for reversible utilization of both the $\text{Cu}^{2+/1+}$ (3.4-2.4 V vs. Li) and $\text{AQDC}^{2-/4-}$ (2.4-1.7 V vs Li) redox events. The Cu oxidation states, investigated at different states of charge by in-situ XANES, were found to contribute one electron per formula unit to the two electrons process for the quinone moiety providing a total theoretical capacity of approximately 162 mAh/g. In the first discharging cycle, 147 mAh/g could be achieved and still 107 mAh/g remained after 50 cycles. This MOF had low ionic conductivity forcing the authors to use only 10 percent active material in their composite electrodes. Introduction of thin films, nanocrystals or different metals were methods proposed to overcome this inherent weakness of the MOFs electrode.

Following up on this research, in 2016 Zhang, Yoshikawa substituted Cu^{2+} for Mn^{2+} to prepare a MOF formulated as $\text{Mn}_7(2,7\text{-AQDC})_6(2,6\text{-AQDC})(\text{DMA})_6$ (Mn-MOF, DMA = N,N-dimethylacetamide).³⁰ By oxidizing Mn^{2+} to Mn^{3+} this MOF could intercalate a PF_6 anion for charge balance. Coupled with the two-electron reduction and oxidation of the quinone moiety, this material could also store three electrons per formula unit and have a theoretical gravimetric capacity of 190 mAh/g. During initial discharge, 205 mAh/g could be achieved in the voltage window (1.5 V to 4.5 V) with negligible capacity fading over 50 cycles. The authors successfully demonstrated a “bipolar charging mechanism containing both faradaic (capacitive) and coulombic (redox) energy storage in the same material. The ionic conductivity was also low in this material, so the author only used 10% active material in the electrode. Although the active material loading was low, impressive capacity (150 mAh/g) could be demonstrated at a high

current density of 5 mA. Again, nanosizing the materials and conductive polymers were discussed as modes of action to address low conductivity and low mass loading. Most notably this work serves as a proof of concept for MOF electrodes materials design to further utilize oxidative anion intercalation mechanism to boost energy storage capability. It is reasonable that highly porous MOFs may be uniquely capable of intercalating large anions currently inaccessible to nonporous transition metal oxide materials.

To raise the voltage and building upon the bipolar charging mechanism, Fang et al investigated a high voltage MOF for material for reversible sodium ion storage. Through a simple room temperature synthesis CuTCNQ phase II (TCNQ=7,7,8,8-tetracyanoquinodimethane) was prepared and fashioned into electrodes.³¹ Functioning as anion intercalation material upon oxidation of Cu^{1+} to Cu^{2+} and a Na^+ cation intercalation material upon reduction of ligand, a dual ion system was tested. With three reversible electron processes this material boasted a high gravimetric capacity of 255 mAh/g and a high median voltage of 3.3V. The MOF material readily disassociated to metal and ligands when oxidized making the as assembled cells very unstable. By means of a very detailed UV-Vis analysis the mode of decomposition was found to occur when Cu^{1+} is oxidized to Cu^{2+} . The authors entrapped the cathode in a polypropylene film to prevent solvation of disassociated ligands and metals. By this method 50 cycles in the voltage window 2.0 to 4.0 were demonstrated with minimal capacity loss. This study further increased the energy storage limits capabilities of redox active MOFs materials by incorporation of a high voltage $\text{Cu}^{1+/2+}$ redox active metal. The metal-based oxidation and resulting anion intercalation led to rapid active material decomposition that required advanced electrode entrapment techniques to mitigate. It was suggested by the authors

that perhaps the cycling stability could be improved by use of a high oxidation state metal that would first undergo reduction rather than oxidation. This mechanism would result in a complete cation intercalation mechanism that could result in more facile ion diffusion. Better materials design is required to further enhance the energy storage capability of MOFs electrodes while simultaneously endowing them with good electrochemical reversibility and structural stability.

We have envisioned that the MOFs design consisting of redox active ligands (Lredox) as MOFs “strut” and earth abundant transition metals (TM, e.g. Ni, Fe, and Mn) as MOFs “node” could lead to high performance MOFs cathode materials for rechargeable batteries. Potential technological advantages of redox active TM-Lredox MOFs as cathode materials include (1) high stability and complete insolubility through strong metal-ligand dative coordination bonding, which is desired to mitigate capacity loss and the shuttle effect of dissolved redox active molecules, (2) high ion mobility through well-defined ion channels in MOFs structures, (3) high charge capacity benefited from low weight and multi-redox changes of redox active ligands, (4) high electrical conductivity through delocalized MOFs networks, and (5) tunability through Lewis acidity of transition metals and substituent effects of redox active ligands. Recent studies have shown the outstanding stability of TM-Lredox MOFs as capacitor materials and anode in sodium ion batteries, implying their potential as battery cathode electrode materials. The intrigues of using MOFs materials as cathode active materials has resulted in a handful of proposed structures.^{22, 25-28, 30-32} The current MOFs examples in the literature have suffered from decomposition (short cycling life), low conductivity requiring low mass loading, and overall low energy densities. Furthermore, the synthetic

methods for obtaining MOFs materials are often challenging/dangerous and often deliver incredibly poor yields. To address these issues, it is of paramount importance to design MOFs for the application at hand and to find improved methods for safe, effective synthesis protocols.

Ca Electrolytes

Li ion batteries have been proved the most influential and successful battery technology, which is witnessed by their extensive applications in portable electronics, power tools, and electrical vehicles. Notably, the 2019 Nobel Prize in chemistry was awarded to three prominent pioneers of Li ion batteries, John B. Goodenough, M. Stanley Whittingham, and Akira Yoshino. However, the increasing demand of Li ion batteries evokes strong concern due to the very limited abundance of lithium in the earth's crust (< 0.1 pg/kg). Political and economic concerns are common as to how the future energy storage system can be accomplished when there are not enough Li resources for Grid energy storage and electric vehicles considering the ever-growing population.³³⁻³⁶

To move beyond Li-ion, the battery research community welcomes efforts to develop next generation rechargeable batteries utilizing abundant elemental alkali and alkaline earth metal anode materials including Na, K, Mg, and Ca.³⁷ Particularly, a renewed interest in Ca metal batteries has been observed in recent years.³⁸ Ca metal has a reduction potential close to Li (+0.172 V vs Li) much lower than Mg (+0.67 V vs Li). Ca metal also has the distinct advantages of divalent redox couple Ca^{2+}/Ca giving it a high volumetric capacity (2099 mAh/cm³). Ca with its small radius and low Lewis acidity is believed to be promising for intercalation chemistries applied in Li ion batteries.³⁹⁻⁴⁰ The elusive rechargeable Ca metal battery has still not been realized even in a laboratory

setting to date. This may be primarily due to the historical lack of suitable electrolytes for Ca batteries. Unlike the Li and Na analogous electrolytes that can be used for reversible plating/stripping of ions at an electrode surface, early studies on various simple Ca salt electrolytes (CaX_2 , $\text{X} = \text{TFSI}$, PF_6 , BF_4 , and ClO_4) by Aurbach's research group indicates that reversible Ca deposition and stripping is impossible due to a passivation layer on the electrode thus disabling further cycles.⁴¹ As recently as 2015, Ponrouch and coworkers discovered that at 100 °C calcium plating and stripping could be achieved with low over potentials (100 mV) by using an electrolyte consisting of 0.45M $\text{Ca}(\text{BF}_4)_2$ in a mixture of ethylene carbonate and propylene carbonate.³⁵ And for the first time, a $\text{Ca}(\text{BH}_4)_2$ electrolyte in THF was demonstrated for reversible calcium deposition and stripping at room temperature by Bruce and Wang et al.⁴² Low polarization (<0.1 V) and high coulombic efficiencies (~95%) were achieved for calcium ion deposition/stripping onto a Gold electrode. Gewirth and coworkers et al. further investigated $\text{Ca}(\text{BH}_4)_2$

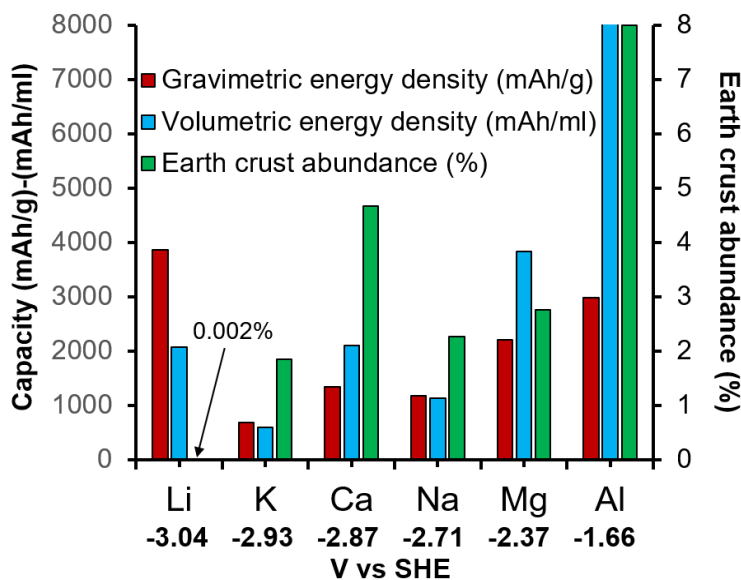


Figure 1-1. A comparison of gravimetric and volumetric capacity, reduction potentials, and abundance for several metallic anodes.^{33, 35}

THF electrolyte on Gold and Platinum micro-electrodes to better understand this unique electrolyte.⁴³ They found that the plating process is governed by a chemical/electrochemical process whereby CaH_2 forms first on the electrode surface followed by electrochemical reduction of $\text{Ca}^{2+}/\text{Ca}^0$ at the interface. Their results found the chemical step to be 10 times faster on Pt than gold. While these results are a major discovery, the BH_4^- anion is unstable at oxidizing voltages greater than 3.0 V vs Au and highly reductive, severely limiting its applications in full batteries.

A breakthrough in room temperature, reversible Ca^{2+} deposition/stripping was made recently by Zhao-Karger and Nazar research groups simultaneously. Both groups reported calcium tetrakis(hexafluoroisopropoxy)borate, $\text{Ca}[\text{B}(\text{hfip})_4]_2$, a new electrolyte capable of the reversible plating and stripping of Ca/Ca^{2+} at room temperature.⁴⁴⁻⁴⁵ Rationale for this electrolyte design was readily provided by the previous success with a magnesium electrolyte paired with the same anion, $\text{Mg}[\text{B}(\text{hfip})_4]_2$.⁴⁶ Li et al demonstrated the $\text{Ca}[\text{B}(\text{hfip})_4]_2$ in DME could achieve ca. 80% coulombic efficiency after a few conditioning cycles on a platinum electrode. The observed high anodic stability above 4.0 V vs Ca echoes the previous studies that the strong C-F bonds of the fluorinated alkoxide ligand (hfip) have previously been proven stable at highly oxidizing voltages up to 5.0 V vs Li. Equally significant, this borate-based electrolyte showed oxidative stabilities of 4.2 V and 4.8 V for stainless steel and Al which are common current collectors found in rechargeable batteries. This group further demonstrated a high conductivity of a 0.25M solution in DME (8.3 mS cm^{-1}) and a high thermal stability of the $\text{Ca}[\text{B}(\text{hfip})_4]_2$ salt ($>120^\circ\text{C}$). Both properties are necessary for the possibility of use in full cell applications. In a Ca|Ca symmetric cell that operated over 250 hours, however,

the polarization of the cell was high (>500 mV, 0.5 mA cm⁻²) but may be improved with further optimizations of electrolyte. Two simultaneous reports were recently published on Ca(B(hfip)₄)₂ in DME as a reversible calcium electrolyte at room temperature with high anodic stability. While the analyses are informative, they are still at the proof of concept stage. For the current reports, cyclic voltammetry was only reported for one type of precious metal working electrode either Pt or Au and with lower coulombic efficiencies (80-92%) than what can be reasonably translated into high performance Ca metal batteries. The electrolytes were also only tested in one solvent (DME) and at one concentration for each paper leaving much space for optimization on the table. Going forward there are many research opportunities afforded by these reports dealing with the solvents, electrodes, concentrations, additives, and full cell studies. For instance, the oxidative stability of Ca(B(hfip)₄)₂ is high enough for this electrolyte to be paired with cathode materials with high redox potentials such Prussian blue (c.a. 3.2-3.5 V vs Ca)⁴⁷⁻⁴⁸ and polyanionic Ca_{0.5}FePO₄ (c.a. 3.3-3.5 V vs Ca)⁴⁸ for full cell testing. Additionally, it is reasonable to expect that other low coordinating anions demonstrated in Mg electrolytes hold promise for the development of new calcium electrolytes.^{46, 49} In brief, the discussed studies on Ca(B(hfip)₄)₂ and other calcium electrolytes give hope to the possibility of Ca full cell batteries with high cell voltages and energy densities in the foreseeable future.

In light of the shortage of suitable electrolyte chemistry for Ca metal batteries, research efforts have been primarily focused on discovering and testing positive electrode materials that can reversibly intercalate/deintercalate Ca ions with beneficial properties compared to commercial Li-ion technologies such as high voltages, discharge capacities, coulombic efficiencies, and cycling stability. V₂O₅ was first investigated for Ca ion

intercalation. As early as 2004, Sakurai et al tested crystalline V_2O_5 electrochemically with Ca ions inserting for a first discharge capacity of 450 mAh/g. Further cycling was not shown but the authors did identify a reversible transformation of the crystalline phase by charge state analysis with ex-situ XRD studies.⁵⁰ The viability of V_2O_5 derivatives for Ca ion battery electrode active materials was recently explored by Vo et al. Through a simple solvothermal process $NH_4V_4O_{10}$ was prepared and tested as a Calcium ion cathode host.⁵¹ 125 mAh/g was reversibly produced during discharge for over 100 cycles. The research went farther, by controlling the size of the particles to 400 nm, 150 mAh/g could be delivered from the cell for over 100 cycles. A full cell was even assembled with a Mn-BDC MOF anode that could consistently deliver 80 mAh/g over 100 cycles. Although the coulombic efficiency was below 80, the authors demonstrated how size control of the particles improves the capacity utilization by increasing the active area of the electrode active material. In a similar vein : Xu et al reported on a bilayered $Mg_{0.25}V_2O_5 \cdot H_2O$ with ultra-stable structure for Ca ion intercalation.⁵² This same Mg pillared hydrated structure has also been explored by other research groups and found to reversibly intercalate divalent ions in the cases of both Magnesium and Zinc. With an initial interlayer spacing of 10.76 angstrom, the authors found that during the electrochemical Ca^{2+} ion insertion step the lattice d-spacing is only altered by 0.09 angstrom – maintaining its structure and allowing for 500 stable cycles with 86.9% capacity retention. This small change in interlayer spacing requires more investigation by considering the ionic diameter of a Ca^{2+} ion is approximately 2.0 angstroms and the solvated ion would be even larger. The small change in interlayer spacing doesn't accommodate the large Ca^{2+} ion and may be

explained by the low Ca uptake ($0.36 \text{ Ca}^{2+}/\text{formula unit}$) or the limitation of redox to a surface only process.

It is important to mention here that the intercalation mechanism for multivalent ions into V_2O_5 is not well understood at this time and can be considered controversial. Verrelli et al. recently compiled the current experimental evidence of Ca and Mg intercalation in V_2O_5 and found the discharged electrodes tended to contain protonated Haggite phase V_2O_5 from wet or dry electrolytes. This research also found removal of multivalent ions from prepared CaV_2O_5 to be unfeasible. Most importantly a call for stricter protocols in characterization was made to guide future researchers to gain a better working knowledge with V_2O_5 and multivalent ion intercalation.

A highly prescient example of high-quality intercalation chemistry research was provided by Tchitchekova et al when they studied TiS_2 as a host for Mg^{2+} , and Ca^{2+} .⁵³ Diligent attention on their part led to the derivation of three intercalation phases for Ca^{2+} intercalation into TiS_2 . All three phases were identified by Rietveld refinement. Satisfyingly, Ca^{2+} intercalation into TiS_2 was proven unambiguously for the first time by X-ray tomography. Lee et al responded in kind by first ever reversible intercalation of Ca^{2+} into TiS_2 by use of $\text{Ca}(\text{TFSI})_2$ in PC and improved the energy storage abilities by adding excess DMC.⁵⁴ The role of DMC was to mitigate co-intercalation of PC into TiS_2 which may be deleterious. Even with their best conditions, charge storage specific capacities were only c.a. 20% of their theoretical values at RT and only one phase was observed. Tchitchekova et al followed up their research confirming TiS_2 could indeed intercalate Ca^{2+} ions at room temperature when $\text{Ca}(\text{TFSI})_2$ was used.⁵⁵ Unfortunately, $\text{Ca}(\text{TFSI})_2$ salts disallow Ca deposition onto a substrate forcing the use of activated

carbon as counter electrode. It is worth mentioning here that Lee et al reported using Li metal as their counter electrode for TiS_2 studies. This leaves us without any room temperature operational $\text{Ca}|\text{TiS}_2$ batteries to reference.

A novel move away from popular Prussian materials and V_2O_5 is the polyanion compound $\text{Na}_2\text{FePO}_4\text{F}$.⁴⁸ Although the voltage (2.6 vs Ca) is slightly lower than Prussian blue, the investigation done by Lipson et al was very thorough. Redox states and crystal structure variation for reversible intercalation was monitored carefully at multiple charge steps to provide a very strong argument that this type of material can truly intercalate Ca ions reversibly. With further optimization of the electrolyte, particle size, and cell components many advances can be made from this study. In particular, the charge discharge curves were sloping rather than plateau like exhibiting what may be pseudocapacitive rather than intercalation or insertion type behaviors with a limited capacity utilization of less than 80 mAh/g much work needs to be done to understand the redox mechanism of multivalent ions with polyanionic compounds.

Due to the difficulties associated with the direct use of Ca metal and underdeveloped electrolyte systems, Ca ion electrode materials have typically been tested in three electrode set-ups with $\text{Ag}^{+/0}$ reference electrodes or internal standards such as ferrocene for calibration.⁵⁶ Typically activated carbon materials are used as negative electrode to balance the charge of the cell by anion uptake. For full cell tests with calcium batteries an anode architecture amenable to Li-ion commercial cells or direct use of Ca metal is preferable. It is advantageous to gain the full advantage of high energy dense Ca metal and enable long term energy storage. Lipson et al. bypassed some of these challenges by exploiting the ability of Ca to form alloys with Sn as anode. For the first

time a Ca ion full cell was reported in 2015 with a calciated Sn anode, $\text{Ca}(\text{PF}_6)_2$ electrolyte in PC:EC and Prussian blue type cathode formulated as $\text{Na}_2\text{MnFe}(\text{CN})_6$.³⁹ This cell had a median operating voltage of approximately 1.0 V and could deliver 85 mAh/g during discharge with 35 cycles shown. The use of Sn/Ca alloy anode allowed for a demonstrable Ca ion battery at the cost of voltage considering the operational voltage of this Prussian blue materials $\text{Na}_2\text{MnFe}(\text{CN})_6$ was greater than 3.0 V vs the standard reduction potential of $\text{Ca}^{2+/0}$. Furthermore, XAS studies showed only Mn oxidation changed during different charge state highlighting the possibility to greatly enhance the capacity by utilization of all metal centers in Prussian blue analogues.

With high cell voltages and highly accessible diffusion pathways, hexacyanoferrate based Prussian analogues have been more extensively studied for Ca ion battery applications. The simplest, traditional Prussian blue material $\text{KFe}^{3+}(\text{Fe}^{2+}(\text{CN})_6)$ was show by Kuperman et al to reversibly intercalate Ca ions at a high voltage (c.a. >3.2 V vs Ca^{2+}/Ca) and high gravimetric capacities exceeding the typical one electron processes typically observed for hexacyanoferrate type materials.⁵⁷ Greater than 120 mAh/g of charge was reversibly stored by this material with 80 stable cycles shown making Prussian blue the highest capacity Ca-ion intercalation material reported. Surprisingly the electrochemistry for Ca intercalation matched well to monovalent potassium ion uptake also conducted in their study. Only three electrode half-cell type cycling data was reported possibly due to the lack of suitable anode materials available for Ca batteries at the time. If a suitable low voltage, comparable high energy density anode was successfully paired with this cathode material, energy densities approaching that of commercial LiFePO_4 are imagined to be obtainable through optimization. Careful

tracking of structural changes during cycling by XRD and careful control over interstitial water content may prove very useful in realizing optimization of Prussian blue for next generation batteries.³⁸ A more in depth review of Prussian blue materials for Ca ion batteries was recently conducted by Xu et al.⁵⁸

The development of next generation batteries comprising Ca metal, Ca electrolytes, and high energy cathode is still a work in progress. Major progress has been made by the recent discovery of electrolytes that plate/strip Ca at elevated temperatures or with borohydride anion in THF solvent. Still, elevated temperature operation is impractical for most commercial applications and the voltage window of borohydrides limits their use to low voltage batteries. Most promising is the highly stable borate-based electrolytes that can function at room temperature reported recently by Li et al and Shyamsunder et al. Positive electrodes have been studied with emphasis on current Li-ion technologies including metal oxides and polyanionic compounds that require more investigation. Substituting the currently untested calcium metal for alloying or intercalation type anodes has also allowed the assembly and testing of Ca ion full cells. Direct use of Ca is a technological necessity towards advancements for applications if Ca ion batteries are ever to find their way in mobile devices and electric vehicles. Ca is an actual contender for supplying energy to popular appliances and reducing the strain on Li reserves. At this time some high voltage Ca intercalation cathodes based on Prussian analogues and anion intercalating graphite have been reported. Bringing all the knowledge and experimentation together to discover a system with high voltage and specific capacity for Ca ion chemistry will be a great challenge requiring many incremental advancements to be made. Before full Ca metal batteries are realized,

suitable electrolyte chemistry must be developed in conjunction with all other components within the battery device.

1-2. Important parameters for rechargeable batteries and electrolytes.

Important parameters for cathode active materials

The cathode active material in a rechargeable static battery serves as a high voltage oxidant where the anode is a low voltage reductant. Both anode and cathode active materials need to have reversible redox reactions for the entire battery to be rechargeable. A key parameter for any cathode active material is where the reversible redox reaction occurs versus a standard electrode (typically vs Li metal). This is called electrode potential when a reference electrode is used, and it is called cell voltage in a battery. The Voltage (denoted V) of any battery can be calculated by subtracting the standard reduction potential (denoted P) of the anode from the cathode as shown in equation 1-1. Higher cell voltage is advantageous as the energy storage capability of any battery is dependent on the Cell voltage (V) and the number of electrons (n) transferred through an external circuit at that voltage as shown in equation 1-2. Theoretical capacity is another important metric for electrode materials. It is a ratio between maximum number of electrons that could be reversibly stored in a material and the mass (M_w) of repeating units in the material. It is calculated as shown in equation 1-3. The actual number of electrons a specific material can store is called the reversible capacity and must be measured using a potentiostat or battery testing device. Typically studies on cathode active materials will use excess anode material. This will make the maximum energy storage capability of the cell dependent on the cathode only thus making direct comparisons to other materials possible. Another important parameter for batteries, rate capability, is typically measured in C rates. Batteries that charge/discharge at high C rates with good reversible capacity are advantageous to those that don't. C rates are calculated

as charging/discharging the battery galvanostatically at a current that theoretically charge/discharge the battery in one hour divided the coefficient of C. For example, charging the battery at 2C rate would theoretically take 30 minutes (1/2 hour) to accomplish. The final important parameter for testing cathode active materials in batteries is capacity retention. This is a measure of how much reversible capacity is remaining after a certain number of cycles when compared to the first cycle. For new electrode materials to meet current industry standards, 80% retention after 500 cycles is typically the requirement.

$$V_{\text{cell}} = P_{\text{Cathode}} - P_{\text{anode}} \quad (1)$$

$$\text{Equation 1-2. } E = V * C_{\text{th}} \quad (2)$$

$$\text{Equation 1-3 } C_{\text{th}} = nF/M_w \quad (3)$$

Important parameters for electrolytes

Coulombic efficiency is the number one most important parameter when testing electrolytes. It is a ratio of charge passed to electroplate ions onto a surface and the amount of charge passed to strip the ions back out into solution. If electrolyte coulombic efficiencies are lower than 100%, then parasitic side reactions are responsible for some of the charge passed in plating. Stripping and plating overpotentials are also important when considering battery electrolytes. Overpotentials are observed on plating/stripping when additional energy is required to achieve an electrochemical reaction beyond what would be calculated using the standard reduction potential for that process. Overpotential is strictly speaking the difference between the onset potential and thermodynamic potential for an electrochemical reaction occurring at the surface of an electrode. Coulombic

efficiencies and overpotentials can both be measured by cyclic voltammetry studies that pass through the standard reduction potential of the metallic ions in solution. The total sum of charge passed for the process would ideally be zero considering a reversal in polarization for the deposition/stripping of ions onto an electrode.

1-3. Dissertation scope

In chapter I, a general introduction and motivation for MOFs capability to replace Li-ion battery electrodes, and the current state of Ca electrolytes was presented.

In chapter II, I devised a new synthetic strategy for preparing highly electronically conductive MOFs that were hitherto inaccessible for broad applications.

In chapter III, A full chemical and electrochemical investigation of redox active MOFs LiNiDBQ_{1.5} was performed. Battery tests found this MOF material to be incredibly durable for long lasting battery applications.

In chapter IV, A full chemical and electrochemical investigation of a MOF electrode material LiFeDBQ_{1.5} was performed with advantageous metal and organic redox confirmed electrochemically and spectroscopically.

In chapter V, A thorough investigation of current collectors, electrodes, and solvent effect was conducted for the only high voltage stability Ca electrolyte known to date.

In chapter VI, A novel Ca electrolyte with weakly coordinating anion was tested spectroscopically and electrochemically. It was found to possess superior qualities to the current electrolyte systems.

In chapter VII, A brief discussion on the significance and future directions of this research was provided.

1-4. References

1. Muench, S.; Wild, A.; Friebe, C.; Haupler, B.; Janoschka, T.; Schubert, U. S., Polymer-Based Organic Batteries. *Chem. Rev.* **2016**, *116*, 9438-9484.
2. Canepa, P.; Sai Gautam, G.; Hannah, D. C.; Malik, R.; Liu, M.; Gallagher, K. G.; Persson, K. A.; Ceder, G., Odyssey of Multivalent Cathode Materials: Open Questions and Future Challenges. *Chem. Rev.* **2017**, *117*, 4287-4341.
3. Chen, H.; Armand, M.; Courty, M.; Jiang, M.; Grey, C. P.; Dolhem, F.; Tarascon, J.-M.; Poizot, P., Lithium Salt of Tetrahydroxybenzoquinone: Toward the Development of a Sustainable Li-Ion Battery. *J. Am. Chem. Soc.* **2009**, *131*, 8984-8988.
4. Mann, M. E.; Bradley, R. S.; Hughes, M. K., Global-scale temperature patterns and climate forcing over the past six centuries. *Nature* **1998**, *392*, 779-787.
5. Mann, M. E.; Zhang, Z.; Hughes, M. K.; Bradley, R. S.; Miller, S. K.; Rutherford, S.; Ni, F., Proxy-based reconstructions of hemispheric and global surface temperature variations over the past two millennia. *Proceedings of the National Academy of Sciences* **2008**, *105*, 13252.
6. Poizot, P.; Dolhem, F., Clean energy new deal for a sustainable world: from non-CO₂ generating energy sources to greener electrochemical storage devices. *Energy Environ. Sci.* **2011**, *4*, 2003-2019.
7. Byrne, R. H.; Nguyen, T. A.; Copp, D. A.; Chalamala, B. R.; Gyuk, I., Energy Management and Optimization Methods for Grid Energy Storage Systems. *IEEE Access* **2018**, *6*, 13231-13260.
8. Zablocki, A., Fact Sheet: Energy Storage (2019). *Environmental and Energy Study Institute* **2019**.

9. Goodenough, J. B.; Park, K.-S., The Li-Ion Rechargeable Battery: A Perspective. *J. Am. Chem. Soc.* **2013**, *135*, 1167-1176.
10. Whittingham, M. S., Lithium Batteries and Cathode Materials. *Chem. Rev.* **2004**, *104*, 4271-4302.
11. Banza Lubaba Nkulu, C.; Casas, L.; Haufroid, V.; De Putter, T.; Saenen, N. D.; Kayembe-Kitenge, T.; Musa Obadia, P.; Kyanika Wa Mukoma, D.; Lunda Ilunga, J.-M.; Nawrot, T. S.; Luboya Numbi, O.; Smolders, E.; Nemery, B., Sustainability of artisanal mining of cobalt in DR Congo. *Nat. Sustain* **2018**, *1*, 495-504.
12. Campbell, G. A., The cobalt market revisited. *Mineral Economics* **2020**, *33*, 21-28.
13. Hanyu, Y.; Ganbe, Y.; Honma, I., Application of quinonic cathode compounds for quasi-solid lithium batteries. *J. Power Sources* **2013**, *221*, 186-190.
14. Liang, Y.; Tao, Z.; Chen, J., Organic Electrode Materials for Rechargeable Lithium Batteries. *Adv. Energy Mater.* **2012**, *2*, 742-769.
15. Renault, S.; Gottis, S.; Barrès, A.-L.; Courty, M.; Chauvet, O.; Dolhem, F.; Poizot, P., A green Li-organic battery working as a fuel cell in case of emergency. *Energy Environ. Sci.* **2013**, *6*, 2124-2133.
16. Song, Z.; Qian, Y.; Gordin, M. L.; Tang, D.; Xu, T.; Otani, M.; Zhan, H.; Zhou, H.; Wang, D., Polyanthraquinone as a Reliable Organic Electrode for Stable and Fast Lithium Storage. *Angew. Chem. Int. Ed.* **2015**, *54*, 13947-13951.
17. Gou, L.; Hao, L.-M.; Shi, Y. X.; Ma, S.-L.; Fan, X.-Y.; Xu, L.; Li, D.-L.; Wang, K., One-pot synthesis of a metal-organic framework as an anode for Li-ion batteries with improved capacity and cycling stability. *J. Solid State Chem.* **2014**, *210*, 121-124.

18. Li, X.; Cheng, F.; Zhang, S.; Chen, J., Shape-controlled synthesis and lithium-storage study of metal-organic frameworks $Zn_4O(1,3,5\text{-benzenetribenzoate})_2$. *J. Power Sources* **2006**, *160*, 542-547.
19. Sheberla, D.; Bachman, J. C.; Elias, J. S.; Sun, C. J.; Shao-Horn, Y.; Dinca, M., Conductive MOF electrodes for stable supercapacitors with high areal capacitance. *Nat. Mater.* **2017**, *16*, 220.
20. Sun, L.; Campbell, M. G.; Dincă, M., Electrically Conductive Porous Metal–Organic Frameworks. *Angew. Chem., Int. Ed.* **2016**, *55*, 3566.
21. Zhou, H. C.; Long, J. R.; Yaghi, O. M., Introduction to Metal–Organic Frameworks. *Chem. Rev.* **2012**, *112*, 673.
22. Wang, L.; Han, Y.; Feng, X.; Zhou, J.; Qi, P.; Wang, B., Metal-Organic Frameworks for Energy Storage: Batteries and Supercapacitors. *Coord. Chem. Rev.* **2015**, *307*.
23. Gong, T.; Lou, X. B.; Fang, J. J.; Gao, E. Q.; Hu, B. W., A novel coordination polymer based on Co(II) hexanuclear clusters with azide and carboxylate bridges: structure, magnetism and its application as a Li-ion battery anode. *Dalton Trans.* **2016**, *45*, 19109-19116.
24. Huang, X.; Sheng, P.; Tu, Z. Y.; Zhang, F. J.; Wang, J. H.; Geng, H.; Zou, Y.; Di, C. A.; Yi, Y. P.; Sun, Y. M.; Xu, W.; Zhu, D. B., A two-dimensional pi-d conjugated coordination polymer with extremely high electrical conductivity and ambipolar transport behaviour. *Nat. Commun.* **2015**, *6*.
25. Fateeva, A.; Horcajada, P.; Devic, T.; Serre, C.; Marrot, J.; Grenèche, J.-M.; Morcrette, M.; Tarascon, J.-M.; Maurin, G.; Férey, G., Synthesis, Structure,

Characterization, and Redox Properties of the Porous MIL-68(Fe) Solid. *Eur. J. Inorg. Chem.* **2010**, 2010, 3789-3794.

26. Férey, G.; Millange, F.; Morcrette, M.; Serre, C.; Doublet, M.-L.; Grenèche, J.-M.; Tarascon, J.-M., Mixed-Valence Li/Fe-Based Metal–Organic Frameworks with Both Reversible Redox and Sorption Properties. *Angew. Chem. Int. Ed.* **2007**, 46, 3259-3263.

27. Zhang, H.; Nai, J.; Yu, L.; Lou, X., Metal-Organic-Framework-Based Materials as Platforms for Renewable Energy and Environmental Applications. *Joule* **2017**, 1, 77-107.

28. Zhang, Z.; Yoshikawa, H.; Awaga, K., Monitoring the Solid-State Electrochemistry of Cu(2,7-AQDC) (AQDC = Anthraquinone Dicarboxylate) in a Lithium Battery: Coexistence of Metal and Ligand Redox Activities in a Metal–Organic Framework. *J. Am. Chem. Soc.* **2014**, 136, 16112-16115.

29. Han, C.; Li, H.; Shi, R.; Zhang, T.; Tong, J.; Li, J.; Li, B., Organic quinones towards advanced electrochemical energy storage: recent advances and challenges. *J. Mater. Chem. A* **2019**, 7, 23378-23415.

30. Zhang, Z.; Yoshikawa, H.; Awaga, K., Discovery of a “Bipolar Charging” Mechanism in the Solid-State Electrochemical Process of a Flexible Metal–Organic Framework. *Chem. Mater.* **2016**, 28, 1298-1303.

31. Fang, C.; Huang, Y.; Yuan, L.; Liu, Y.; Chen, W.; Huang, Y.; Chen, K.; Han, J.; Liu, Q.; Huang, Y., A Metal–Organic Compound as Cathode Material with Superhigh Capacity Achieved by Reversible Cationic and Anionic Redox Chemistry for High-Energy Sodium-Ion Batteries. *Angew. Chem. Int. Ed.* **2017**, 56, 6793-6797.

32. Shin, J.; Kim, M.; Cirera, J.; Chen, S.; Halder, G. J.; Yersak, T. A.; Paesani, F.; Cohen, S. M.; Meng, Y. S., MIL-101(Fe) as a lithium-ion battery electrode material: a

- relaxation and intercalation mechanism during lithium insertion. *J. Mater. Chem. A* **2015**, *3*, 4738-4744.
33. Elia, G. A.; Marquardt, K.; Hoepfner, K.; Fantini, S.; Lin, R.; Knipping, E.; Peters, W.; Drillet, J.-F.; Passerini, S.; Hahn, R., An Overview and Future Perspectives of Aluminum Batteries. *Adv. Mater.* **2016**, *28*, 7564-7579.
34. Ponrouch, A.; Bitenc, J.; Dominko, R.; Lindahl, N.; Johansson, P.; Palacin, M. R., Multivalent rechargeable batteries. *Energy Storage Mater.* **2019**, *20*, 253-262.
35. Ponrouch, A.; Frontera, C.; Bardé, F.; Palacín, M. R., Towards a calcium-based rechargeable battery. *Nat. Mater* **2015**, *15*, 169.
36. Wang, H.; Yu, D.; Kuang, C.; Cheng, L.; Li, W.; Feng, X.; Zhang, Z.; Zhang, X.; Zhang, Y., Alkali Metal Anodes for Rechargeable Batteries. *Chem* **2019**, *5*, 313-338.
37. Arroyo-de Dompablo, M. E.; Krich, C.; Nava-Avendaño, J.; Palacín, M. R.; Bardé, F., In quest of cathode materials for Ca ion batteries: the CaMO₃ perovskites (M = Mo, Cr, Mn, Fe, Co, and Ni). *PCCP* **2016**, *18*, 19966-19972.
38. Arroyo-de Dompablo, M. E.; Ponrouch, A.; Johansson, P.; Palacín, M. R., Achievements, Challenges, and Prospects of Calcium Batteries. *Chem. Rev.* **2019**.
39. Lipson, A. L.; Pan, B.; Lapidus, S. H.; Liao, C.; Vaughey, J. T.; Ingram, B. J., Rechargeable Ca-Ion Batteries: A New Energy Storage System. *Chem. Mater.* **2015**, *27*, 8442-8447.
40. Nielson, K. V.; Liu, T. L., Dawn of Calcium Batteries. *Angew. Chem. Int. Ed.* **2020**, *59*, 3368-3370.
41. Aurbach, D.; Skaletsky, R.; Gofer, Y., The Electrochemical Behavior of Calcium Electrodes in a Few Organic Electrolytes. *J. Electrochem. Soc.* **1991**, *138*, 3536-3545.

42. Wang, D.; Gao, X.; Chen, Y.; Jin, L.; Kuss, C.; Bruce, P. G., Plating and stripping calcium in an organic electrolyte. *Nat. Mater* **2017**, *17*, 16.
43. Ta, K.; Zhang, R.; Shin, M.; Rooney, R. T.; Neumann, E. K.; Gewirth, A. A., Understanding Ca Electrodeposition and Speciation Processes in Nonaqueous Electrolytes for Next-Generation Ca-Ion Batteries. *ACS Appl. Mater. Interfaces* **2019**, *11*, 21536-21542.
44. Li, Z.; Fuhr, O.; Fichtner, M.; Zhao-Karger, Z., Towards stable and efficient electrolytes for room-temperature rechargeable calcium batteries. *Energy Environ. Sci.* **2019**, *12*, 3496-3501.
45. Shyamsunder, A.; Blanc, L. E.; Assoud, A.; Nazar, L. F., Reversible Calcium Plating and Stripping at Room Temperature Using a Borate Salt. *ACS Energy Lett.* **2019**, *4*, 2271-2276.
46. Zhao-Karger, Z.; Gil Bardaji, M. E.; Fuhr, O.; Fichtner, M., A new class of non-corrosive, highly efficient electrolytes for rechargeable magnesium batteries. *J. Mater. Chem. A* **2017**, *5*, 10815-10820.
47. Shiga, T.; Kondo, H.; Kato, Y.; Inoue, M., Insertion of Calcium Ion into Prussian Blue Analogue in Nonaqueous Solutions and Its Application to a Rechargeable Battery with Dual Carriers. *The Journal of Physical Chemistry C* **2015**, *119*, 27946-27953.
48. Lipson, A. L.; Kim, S.; Pan, B.; Liao, C.; Fister, T. T.; Ingram, B. J., Calcium intercalation into layered fluorinated sodium iron phosphate. *J. Power Sources* **2017**, *369*, 133-137.
49. Luo, J.; Bi, Y.; Zhang, L.; Zhang, X.; Liu, T. L., A Stable, Non-Corrosive Perfluorinated Pinacolatoborate Mg Electrolyte for Rechargeable Mg Batteries. *Angew. Chem. Int. Ed.* **2019**, *58*, 6967-6971.

50. Hayashi, M.; Arai, H.; Ohtsuka, H.; Sakurai, Y., Electrochemical Insertion/Extraction of Calcium Ions Using Crystalline Vanadium Oxide. *Electrochem. Solid-State Lett.* **2004**, *7*, A119-A121.
51. Vo, T. N.; Kim, H.; Hur, J.; Choi, W.; Kim, I. T., Surfactant-assisted ammonium vanadium oxide as a superior cathode for calcium-ion batteries. *J. Mater. Chem. A* **2018**, *6*, 22645-22654.
52. Xu, X.; Duan, M.; Yue, Y.; Li, Q.; Zhang, X.; Wu, L.; Wu, P.; Song, B.; Mai, L., Bilayered Mg_{0.25}V₂O₅·H₂O as a Stable Cathode for Rechargeable Ca-Ion Batteries. *ACS Energy Lett.* **2019**, *4*, 1328-1335.
53. Tchitchekova, D. S.; Ponrouch, A.; Verrelli, R.; Broux, T.; Frontera, C.; Sorrentino, A.; Bardé, F.; Biskup, N.; Arroyo-de Dompablo, M. E.; Palacín, M. R., Electrochemical Intercalation of Calcium and Magnesium in TiS₂: Fundamental Studies Related to Multivalent Battery Applications. *Chem. Mater.* **2018**, *30*, 847-856.
54. Lee, C.; Jeong, Y.-T.; Nogales, P. M.; Song, H.-Y.; Kim, Y.; Yin, R.-Z.; Jeong, S.-K., Electrochemical intercalation of Ca²⁺ ions into TiS₂ in organic electrolytes at room temperature. *Electrochemistry Communications* **2019**, *98*, 115-118.
55. Verrelli, R.; Black, A.; Dugas, R.; Tchitchekova, D.; Ponrouch, A.; Palacin, M. R., Steps Towards the Use of TiS₂ Electrodes in Ca Batteries. *J. Electrochem. Soc.* **2020**, *167*, 070532.
56. Liu, X.; Elia, G. A.; Passerini, S., Evaluation of counter and reference electrodes for the investigation of Ca battery materials. *J. Power Sources Advances* **2020**, *2*, 100008.

57. Kuperman, N.; Padigi, P.; Goncher, G.; Evans, D.; Thiebes, J.; Solanki, R., High performance Prussian Blue cathode for nonaqueous Ca-ion intercalation battery. *J. Power Sources* **2017**, *342*, 414-418.
58. Xu, Y.; Zheng, S.; Tang, H.; Guo, X.; Xue, H.; Pang, H., Prussian blue and its derivatives as electrode materials for electrochemical energy storage. *Energy Storage Mater.* **2017**, *9*, 11-30.

CHAPTER II

A STRATEGIC HIGH YIELD SYNTHESIS OF 2,5-DIHYDROXY-1,4-BENZOQUINONE BASED MOFS

2-1. Abstract

Metal Organic Frameworks (MOFs) of the type $\text{NBu}_4\text{M}(\text{DHBQ})_{1.5}$ ($\text{M} = \text{Ni}^{2+}$, Fe^{2+} , and Co^{2+} , and $\text{DHBQ} = 2,5\text{-dihydroxy-1,4-benzoquinone}$) were prepared with improved yield up to 100% via a simple benchtop aqueous addition reaction. For the first time, the crystalline phase of this formula polymer was synthesized without in-situ generation of the DHBQ ligand from 2,5-diamino-1,4-benzoquinone (DABQ). Powder X-ray diffraction and elemental analysis confirm the crystalline phase and composition of products. Infra-red and electron dispersive spectroscopy further confirm the materials are homologous to the reported single crystalline polymers. The present MOF synthesis can be extended to halide substituted ligands, 3,6-dichloro-2,5-dihydroxy-1,4-benzoquinone (chloranilic acid, CAN) and 3,6-difluoro-2,5-dihydroxy-1,4-benzoquinone (fluoranilic acid, FAN).

2-2. Introduction

Electrically conductive metal organic frameworks (MOFs)¹⁻⁴ represents an important extension of the applications of MOFs materials beyond their current applications in gas sorption/separation, sensors, and catalysis.⁵ Indeed, over the past ten years, conductive MOFs have found use in a variety of applications including but not limited to electrocatalysis, thermoelectric, field effect transistors, and supercapacitors.^{4, 6-8} In 2011

Adapted with permission from Nielson, K. V.; Zhang, L.; Zhang, Q.; Liu, T. L., A Strategic High Yield Synthesis of 2,5-Dihydroxy-1,4-benzoquinone Based MOFs. *Inorganic Chemistry* **2019**, *58*, 10756-10760.

Abrahams *et al* reported on the synthesis of single crystals for a family of coordination polymers with formula $\text{NBu}_4\text{M}(\text{DHBQ})_{1.5}$ ($\text{M} = \text{Mn, Fe, Co, Ni, Zn, and Cd}$).⁹ This pioneering research inspired others including Long's research group to more closely examine this family of MOFs polymers.¹⁰⁻¹² Long's group analyzed $\text{NBu}_4\text{Fe}_2\text{DBQ}_3$ by studying its electrical and magnetic properties. Their results concluded this material had very high electrical conductivity ($10^{-2} \text{ S}\cdot\text{cm}^{-1}$) and high ferromagnetic ordering temperature (130 K) making this a desirable material for applications requiring high charge mobility. Recently, our group has also become interested in this class of MOFs materials specifically to exploit their non-innocent DHBQ ligand based redox properties for energy storage/conversion applications.

However, the synthesis of these materials is not straightforward. Both research groups employed an indirect synthetic method whereby the DHBQ ligand was not used in the synthesis in favor of 2,5-diamino-1,4-benzoquinone (DABQ) which undergoes in-situ hydrolysis to become the DHBQ ligand (see Figure 2-1A).⁹ The reported reactions were typically done on a milligram scale in sealed glass vial reactors above the boiling point of the solvent. These conditions led to low yields (< 43%), requiring up to 48 hours of reaction time. To further study these polymers or produce them on a large enough scale for materials utilization, a straightforward, high yield synthesis needs to be demonstrated. In addition, it is important to mention that for a scaled-up synthesis of $\text{NBu}_4\text{M}(\text{DHBQ})_{1.5}$ crystalline polymers, the direct use of the DHBQ ligand is intuitively desired rather than DABQ. This is due in part to the much lower cost of DHBQ compared to DABQ. However, no study has been reported on the direct use of this ligand in making $\text{NBu}_4\text{M}(\text{DHBQ})_{1.5}$ MOFs materials. Herein, we report highly efficient, selective

synthesis of **NBu₄M(DHBQ)_{1.5}** MOFs (M = Ni and Fe) using the DHBQ ligand under strategically controlled reaction conditions.

2-3. Experimental Section

Chemicals and instruments. All chemicals were purchased from TCI, stored in an Ar glovebox, and used directly. Elemental analysis was done by Atlantic Microlabs. SEM was done on a FEI Quanta FEG 650. PXRD was obtained from a Rigaku MiniFlex II tabletop X-ray diffractometer with silicon wafer sample holder. FT-IR was done on a Perkin Elmer Spectrum 100 FT-IR spectrometer with universal ATR sampling accessory. NMR was done on a Jeol 300 MHz Spectrometer. All reagents and prepared samples were dried at 100 °C in a vacuum oven before masses were taken.

SEM sample preparation. 1.0 mg of sample powder was dispersed in 1.0 ml of new degassed absolute ethanol. The sample was sonicated for 30 minutes. Under Ar atmosphere glovebox conditions (<1.0 ppm O₂, <0.1 ppm H₂O), several drops of suspension were layered onto an Al SEM sample stub and left to dry. The samples were then sealed in air-free SEM sample holders for transportation. The sample stubs were loaded into the FEI Quanta FEG 650 under a cool stream of nitrogen then tested under reduced pressures (<5.0*10⁻⁵ mm Hg).

Literature synthesis of NBu₄Ni(DHBQ)_{1.5}. The exact conditions reported by Abrahams et al.¹³ were utilized to prepare this sample. In brief: 2,5-diamino-1,4-hydroquinone dihydrochloride (38.14 mg, 0.1803 mmol) was dissolved in 30ml D.I. H₂O and bubble with oxygen to generate 2,5-diamino-1,4-benzoquinone. The solution was then cleared of oxygen by freeze pump thaw. Tetra butyl ammonium bromide (excess, 300 mg) was dissolved followed by Ni(OAc)₂•4H₂O (44.86 mg, 0.1803 mmol). This

suspension was loaded into a thick-walled glass vial and flame sealed. The vial was placed in a preheated 120 °C oven for 48 hours and then removed all at once. A black precipitate lined the walls of the vial and some small crystals were observed above the solvent line. The solid components were extracted by vacuum filtration with rinsing by degassed water. The solids were dried by vacuum oven at 100 °C for 1 hour. Yield: <20 mg, 47%. Anal. Calcd. for C₂₅H₃₉NiNO₆: C, 59.07; H, 7.73; N, 2.75. Found: C, 55.01; H, 6.36; N, 5.54. ¹H NMR (300 MHz, 4 drops conc. HCl in 1ml DMSO-d₆, TMS): δ = 7.27 (acid), δ = 5.63 (3H; ring CH), δ = 2.88 (6.92 H; NBu₄ CH₂), δ = 1.27 (6.91 H; NBu₄ CH₂), δ = 1.00 (6.90 H; NBu₄ CH₂), δ = 0.61 (10.44 H; NBu₄ CH₃). (PXRD Figure 2-5.)

Literature synthesis of NBu₄Fe(DHBQ)_{1.5}. The exact conditions reported by Long et al.¹⁰ were utilized to prepare this sample. The conditions were the same as the above synthesis for NBu₄Ni(DHBQ)_{1.5} excepting Fe(SO₄)₂ • 7H₂O (150.4 mg, .5409 mmol) was used in place of Ni(OAc)₂ • 4H₂O. Yield: <15mg, 63%. Anal. Calcd for C₂₅H₃₉FeNO₆: C, 59.41; H, 7.78; N, 2.77. Found: C, 55.14; H, 6.50; N, 5.58.

Ni(DHBQ)(H₂O)₂. The conditions reported by Abrahams and Long for the Ni and Fe polymers respectively were followed excepting the direct use of 2,5-dihydroxy-1-4-benzoquinone. Gray (Ni) or Black (Fe) powders were collected by filtration. It was found that low crystallinity one dimensional polymers formulated as M(DHBQ)(H₂O) were generated at room temperature with or with or without the presence of NBu₄⁺ salts. Highly crystalline NiDHBQ(H₂O)₂ could be prepared by combining aqueous metal solution to ligand solution at 100 °C, cooling to room temperature and rinsing with water and ethanol on the filter.

New synthesis of NBu₄Ni(DHBQ)_{1.5}. DHBQ (1.50 mmol, 210 mg) and NBu₄Br (excess, 2.00 g) were dissolved in 50 ml degassed H₂O under N₂ reflux. Ni(OAc)₂•4H₂O (249 mg, 1.00 mmol) was dissolved separately in 10 ml degassed H₂O, added dropwise over 15 minutes, then left to reflux for an additional 30 minutes. A carrot orange precipitate was extracted by vacuum filtration and rinsing with water. Yield: 510.0 mg, 100%. Anal. Calcd for C₂₅H₃₉NiNO₆: C, 59.07; H, 7.73; N, 2.75. Found: C, 58.92; H, 7.67; N, 2.73. ¹H NMR (300 MHz, 4 drops HCl in 1 ml DMSO-d₆, TMS): δ = 6.93 (acid), δ = 5.54 (3H; ring CH), δ = 2.73 (7.97 H; NBu₄ CH₂), δ = 1.13 (7.99 H; NBu₄ CH₂), δ = 0.86 (7.98 H; NBu₄ CH₂), δ = 0.47 (12.0 H; NBu₄ CH₃). (PXRD Figure 2-2B)

New synthesis of NBu₄Fe(DHBQ)_{1.5}. The conditions were the same as the previous synthesis with minor modifications. FeSO₄•7H₂O (278 mg, 1.0 mmol) was used as the metal source and a greater excess of NBu₄Br (3.0-4.0g) was found to improve yield. Also, air sensitivity was observed for this material by loss of crystallinity after air exposure. As such, air free filtration under N₂ was utilized to extract a black purple microcrystalline precipitate that was then stored in inert atmosphere. Yield: 434.6 mg, 86%. Anal. Calcd for C₂₅H₃₉FeNO₆: C, 59.41; H, 7.78; N, 2.77. Found: C, 59.95; H, 7.86; N, 2.76. (PXRD Figure 2-2C).

Synthesis of NBu₄Ni(CAN)_{1.5}. 3,6-dichloro-2,5-dihydroxy-1,4-benzoquinone (chloranilic acid, CAN) (0.3 mmol, 60.0 mg) and NBu₄Br (1.00 mmol, 322 mg) were dissolved in 100 ml degassed H₂O under N₂ reflux. Ni(NO₃)₂•6H₂O (58.0 mg, 0.2 mmol) was dissolved separately in 10 ml degassed H₂O, added dropwise over 15 minutes, then left to reflux for an additional 30 minutes. A brown precipitate was extracted by vacuum filtration and rinsing with water. Yield 175.0 mg, 99% by mass, 96.4% by chlorine

composition. Anal. Calcd for $C_{25}H_{36}FNiNO_6C_{13}$: C, 49.0; H, 5.88; N, 2.29; Cl, 17.39.

Found: C, 49.95; H, 6.71; N, 2.40; Cl, 16.76. (PXRD Figure 2-7).

Synthesis of $NBu_4Ni(FAN)_{1.5}$. 3,6-difluoro-2,5-dihydroxy-1,4-benzoquinone (fluoranilic acid, FAN) (0.3 mmol, 53.4 mg) and NBu_4Br (1.0 mmol, 322 mg) were dissolved in 100 ml degassed H_2O under N_2 reflux. $Ni(NO_3)_2 \cdot 6H_2O$ (58.0 mg, 0.2 mmol) was dissolved separately in 10 ml degassed H_2O , added dropwise over 15 minutes, then left to reflux for an additional 30 minutes. A brown precipitate was extracted by vacuum filtration and rinsing with water. Yield 120.0 mg, 92.0% by mass, 96.2% by fluorine composition. Anal. Calcd for $C_{25}H_{36}FNiNO_6F_3$: C, 53.40; H, 6.45; N, 2.49; F, 10.13. Found: C, 53.66; H, 6.76; N, 2.50; F, 9.75. (PXRD Figure 2-8).

2-4. Results and Discussion

To prepare the as mentioned MOFs, first, the exact synthetic procedures were followed from Abrahams *et al* for the $NBu_4Ni(DHBQ)_{1.5}$ MOFs using $Ni(OAc)_2 \cdot 4H_2O$ and DABQ in the presence of excess NBu_4Br . The X-ray diffraction pattern obtained was in close agreement to the simulated pattern obtained from the reported $NBu_4Ni(DHBQ)_{1.5}$ MOFs crystal structure where the NBu_4^+ cation was squeezed because of disorder.⁹ The location of all peaks was a good match confirming the presence of the reported crystalline phase for $NBu_4Ni(DHBQ)_{1.5}$ (Figure 2-2). The relative intensities of some peaks are not in close agreement, which is explained as there is no NBu_4^+ cation in the simulated PXRD

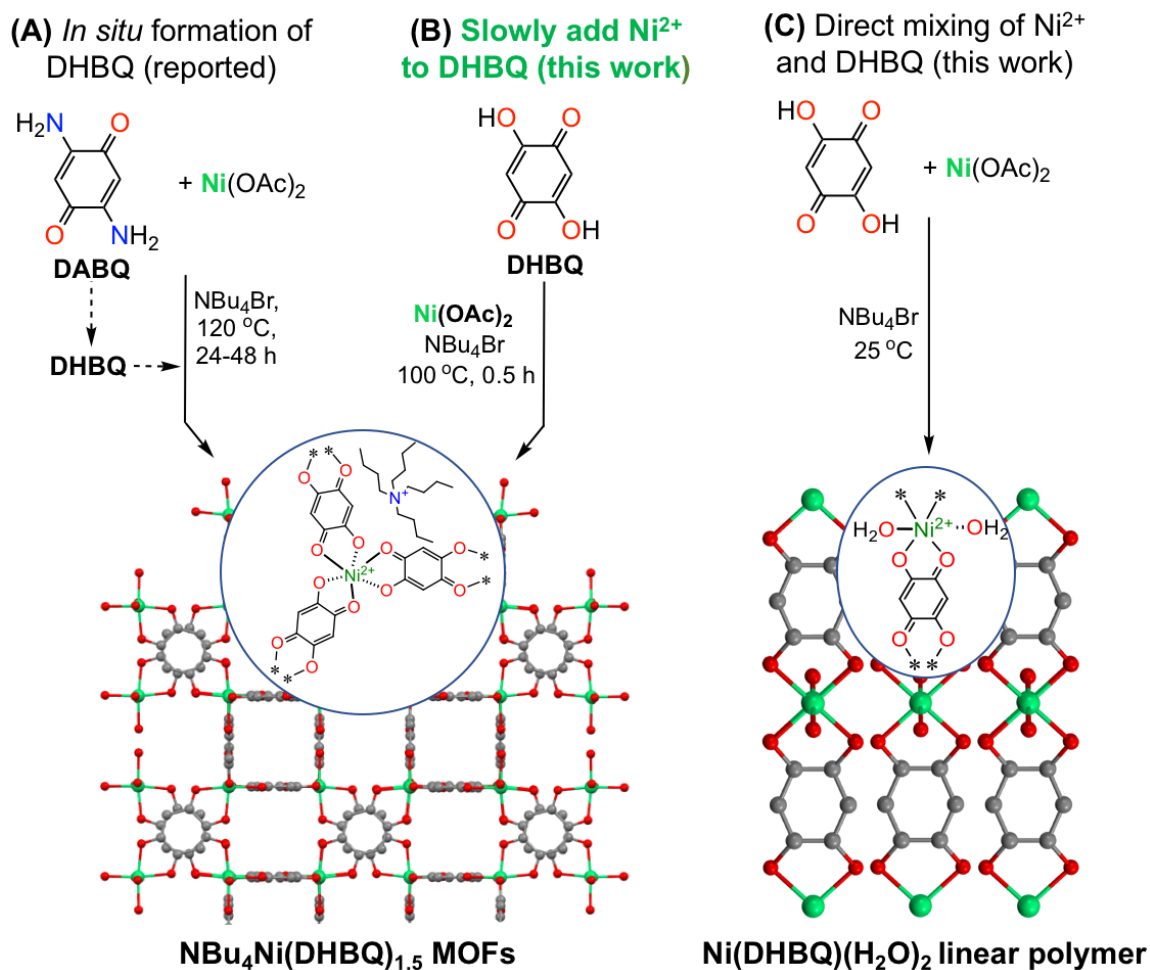


Figure 2-1. (A) Literature reported $\text{NBu}_4\text{Ni}(\text{DHBQ})_{1.5}$ by in-situ hydrolysis of DABQ to DHBQ. (B) Synthesis of $\text{NBu}_4\text{Ni}(\text{DHBQ})_{1.5}$ reported here by direct use of the DHBQ ligand. (C) Generation of $\text{Ni}(\text{DHBQ})(\text{H}_2\text{O})_2$ one-dimensional polymer by direct mixing Ni^{2+} and DHBQ at room temperature.

pattern. In the ^1H NMR spectrum of HCl digested MOFs samples. The proton resonances for the in situ formed DHBQ from the hydrolysis of DABQ and the $^n\text{Bu}_4\text{N}^+$ cation was confirmed (Figure 2-9). The elemental analysis performed on these samples indicated a 2-fold excess of nitrogen for both samples suggesting incomplete hydrolysis of the amine or incorporation of NH_4^+ cations into the product. The presence of NH_4^+ in the product can be explained by the in-situ hydrolysis of DABQ to produce NH_3 and subsequent solvation to NH_4OH . It is reasonable to believe NH_4^+ can be incorporated as counter cations into the Ni-MOF. NH_4^+ in the product is also corroborated by low C and H

percentages from elemental analysis. In the ^1H NMR studies of the acid digested MOFs, the observed ratio (3:7) of the ring protons in DHBQ versus the protons of one methylene group in the $^n\text{Bu}_4\text{N}^+$ cation was larger than the formula ratio (3:8), further suggesting the presence of the NH_4^+ cation.

Initial attempts to synthesize $\text{NBu}_4\text{Ni}(\text{DHBQ})_{1.5}$ followed the synthetic method reported by Abrahams exactly excepting the direct use of DHBQ over DABQ. However, it was observed every time the metal and ligand were combined at room temperature, with or without the NBu_4Br salt, that precipitates immediately began to fall out of solution. There was no indication of the correct phase of material by PXRD (Figure 2-2A). According to literature,¹³⁻¹⁴ the obtained PXRD pattern indicates only the formation of the one-dimensional polymer, $\text{Ni}(\text{DHBQ})(\text{H}_2\text{O})_2$. Even after heating at $120\text{ }^\circ\text{C}$ for two days, the linear polymer diffraction pattern was still observed without the formation of $\text{NBu}_4\text{Ni}(\text{DHBQ})_{1.5}$. In the case of Fe, only amorphous or unknown phases could be observed by PXRD under the same conditions.

The precipitation of the linear polymer $\text{NiDHBQ}(\text{H}_2\text{O})_2$ dominated the reaction chemistry when $\text{Ni}(\text{OAc})_2\cdot 4\text{H}_2\text{O}$, tetrabutylammonium salts and DHBQ were directly mixed at room temperature. This phenomenon was attributed to the low solubility ($< 3\text{ mM}$) of DHBQ in water at ambient temperatures and high solubility of the metal salt. We envisioned that slow addition of the Ni salt into a refluxing aqueous solution of DHBQ (20 mM) would instead maintain a high ligand to metal ratio and favor the desired three-ligand coordinated $\text{NBu}_4\text{Ni}(\text{DHBQ})_{1.5}$ over the two-ligand coordinated linear polymer.

We believe $\text{NBu}_4\text{Ni}(\text{DBHQ})_{1.5}$ is a thermodynamic product formed at the reflux temperature while the formation of the $\text{Ni}(\text{DBHQ})(\text{H}_2\text{O})_2$ is kinetically driven by

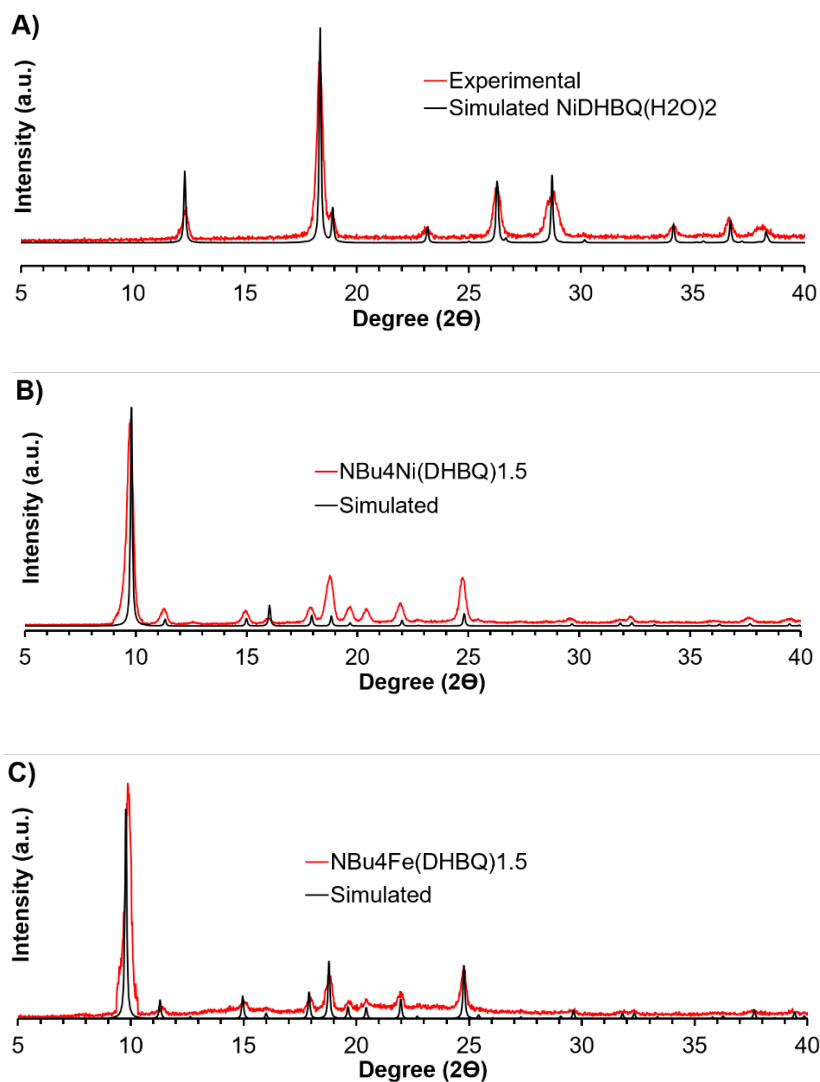


Figure 2-2. X-ray diffraction data obtained from samples prepared by facile synthesis compared to simulated patterns for (A) $\text{Ni}(\text{DHBQ})(\text{H}_2\text{O})_2$ prepared by room temperature reagent combination. And hot addition reactions presented here for (B) $\text{NBu}_4\text{Ni}(\text{DHBQ})_{1.5}$ and (C) $\text{NBu}_4\text{Fe}(\text{DHBQ})_{1.5}$.

precipitation at a lower temperature. By refluxing 50 ml degassed water with oil bath temperature set to 120 °C, DHBQ and excess NBu_4Br were dissolved. $\text{Ni}(\text{OAc})_2 \cdot 4\text{H}_2\text{O}$ dissolved in H_2O was added dropwise with vigorous stirring over 20-30 minutes making sure the water was boiling before subsequent drops were added. After the metal solution was added, the reaction was kept under reflux for an additional 30 minutes. The vial was

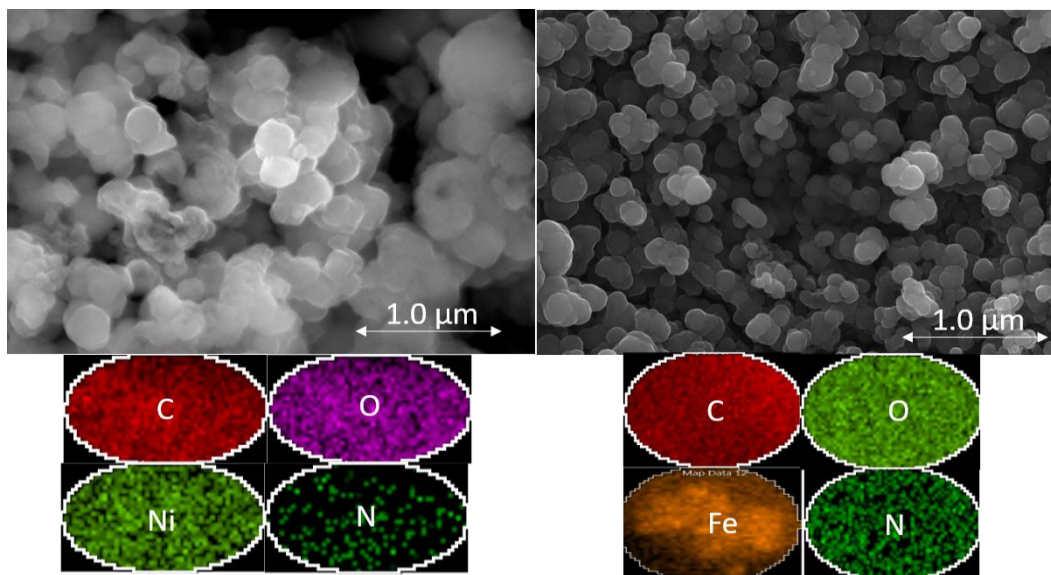


Figure 2-3. SEM and EDS analysis of $\text{NBu}_4\text{Ni}(\text{DHBQ})_{1.5}$ (left) and $\text{NBu}_4\text{Fe}(\text{DHBQ})_{1.5}$ (right).

removed from the oil bath and left until boiling dissipated. The contents of the flask were then filtered hot using an air free filtration device under Ar. The carrot orange powder was then rinsed with degassed H_2O and dried on the filter. The PXRD pattern of the synthesized $\text{NBu}_4\text{Ni}(\text{DBQ})_{1.5}$ MOFs matched the reported phase (Figure 2-2B). The Ni sample remained stable after several days exposed to ambient atmospheric conditions and showed no loss of crystallinity by PXRD. To further confirm the generality of the synthesis route using the DHBQ ligand, $\text{NBu}_4\text{Fe}(\text{DBQ})_{1.5}$ was also prepared as purple (Fe) powders using $\text{Fe}(\text{SO}_4)_2 \cdot 7\text{H}_2\text{O}$, which was confirmed by the match of the experimental and simulated PXRD (Figure 2-2C). The Fe sample on the other hand was highly sensitive to atmosphere and lost its crystallinity within three hours of ambience. Thus, it is very important to utilize air free conditions when handling the Fe MOFs.

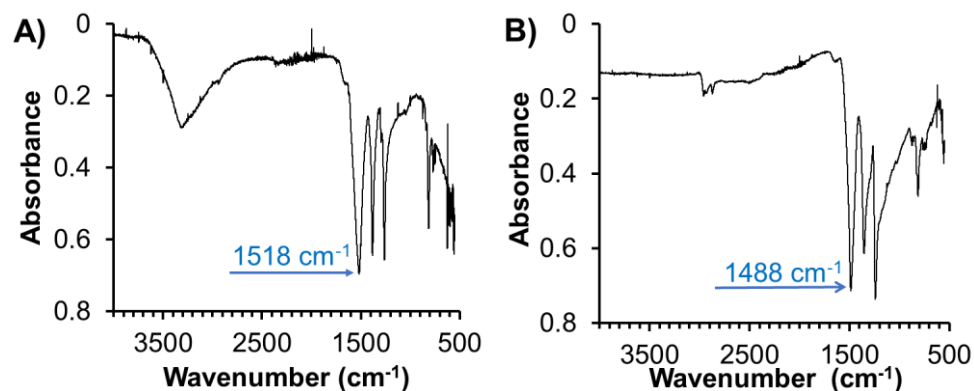


Figure 2-4. FT-IR absorbance spectra of A) $\text{NBu}_4\text{Ni}(\text{DHBQ})_{1.5}$ and B) $\text{NBu}_4\text{Fe}(\text{DHBQ})_{1.5}$

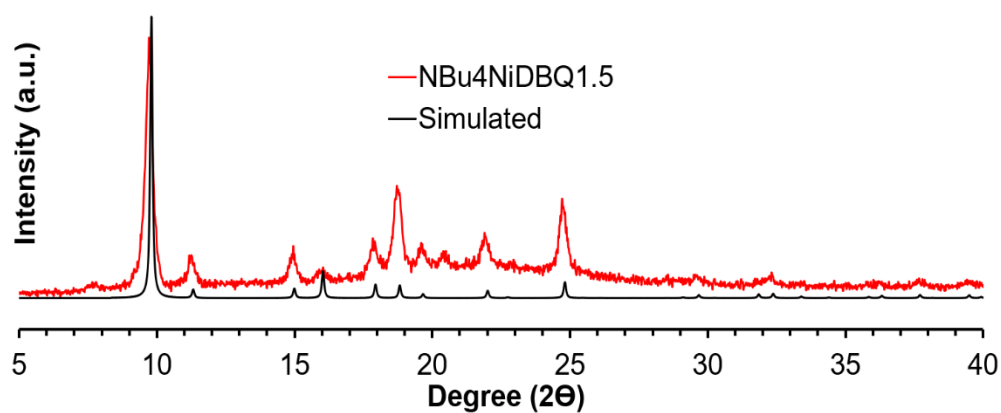


Figure 2-5. PXRD of $\text{NBu}_4\text{NiDHBQ}_{1.5}$ prepared with DABQ ligand in a sealed glass vial reactor compared to the simulated pattern.

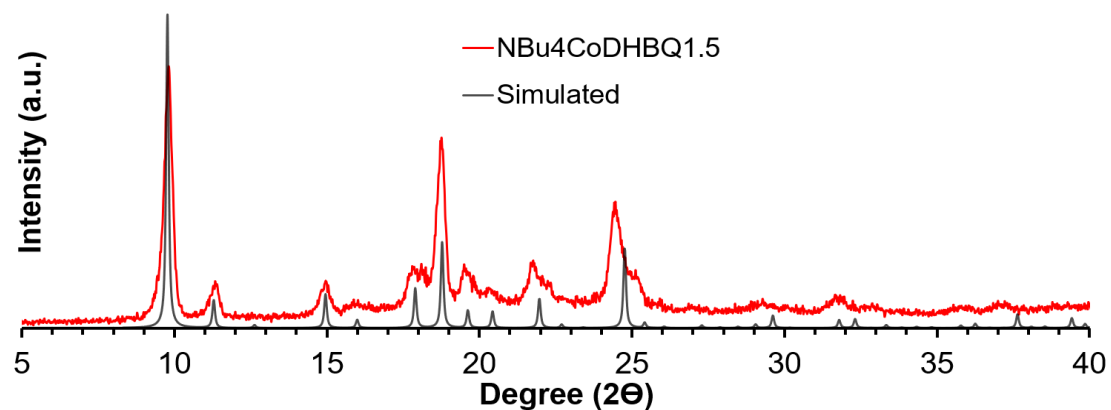


Figure 2-6. $\text{NBu}_4\text{CoDHBQ}_{1.5}$ and simulation prepared by the high temperature addition reaction presented in this work.

The elemental analysis for the Ni and Fe MOFs samples agreed quite well with their chemical formula. Indeed, by direct use of DHBQ, the possibility of incomplete hydrolysis of DABQ or NH_4^+ incorporation is eliminated. The ^1H NMR studies of acid digested Ni-MOF samples consistently determine the organic composition (Figure 2-10). Qualitatively, only DHBQ molecules and NBu_4^+ cations were observed for all samples digested by concentrated HCl. The integration ratio (ca. 3:7.98) of peaks from the ring protons in the DHBQ versus the protons of one methylene group in the $^n\text{Bu}_4\text{N}^+$ cation proved the sample prepared by the slow addition method agreed better with the expected chemical formula of $\text{NBu}_4\text{NiDHBQ}_{1.5}$ (3:8) than did the integrations for the sample prepared by the hydrothermal method (Figure 2-9).

The IR spectra of the Ni and Fe MOFs agreed with the results reported in the literature.¹⁰⁻¹¹ Most notably from the IR spectra, it was observed the C=O stretching frequency for the Fe polymer was located 30 cm^{-1} lower than the Ni polymer (Figure 2-4). This result is consistent with the conclusion made by Long and coworkers concerning the increased C=O bond length in the DHBQ (3-) radical ligands.¹⁰⁻¹¹ SEM indicated uniform morphology for both samples (Figure 2-3). The Ni MOFs appeared to lack noticeable micron size morphology instead it appears to be polycrystalline nanoparticles. This observation is consistent with the broader Bragg diffraction peaks (full width half max at $18.84\text{ deg } 2\Theta$: c.a. $0.42\text{ deg } 2\Theta$, c.a. 20.2 nm) when compared to the simulated spectra (Figure 2-2). The Fe polymer had a similar morphology of sub-micron nanoparticle aggregates (full width half max at $18.84\text{ deg } 2\Theta$: c.a. $0.40\text{ deg } 2\Theta$, c.a. 21.02 nm).

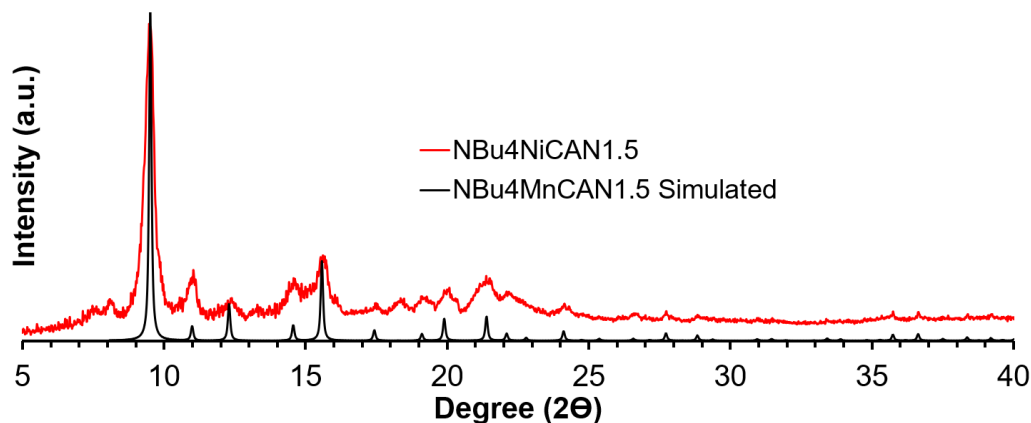


Figure 2-7. NBu₄NiCAN_{1.5} prepared by high temperature addition reaction and simulation.

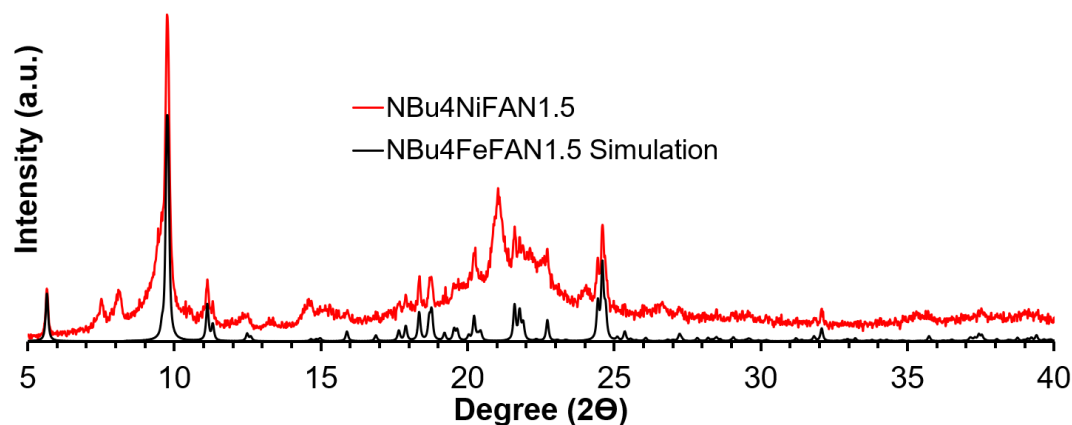


Figure 2-8. NBu₄NiFAN_{1.5} prepared by high temperature addition reaction and simulation.

We also conducted another reaction using Co(OAc)₂•4H₂O and observed the formation of the NBu₄Co(DHBQ)_{1.5} phase by PXRD. Moreover, the scope and modularity of this synthetic method was briefly extended further, beyond the DHBQ ligand, by substitution of 3,6-dichloro-2,5-dihydroxy-1,4-benzoquinone (chloranilic acid, CAN) and 3,6-difluoro-2,5-dihydroxy-1,4-benzoquinone (fluoranilic acid, FAN) as bridging ligands. Under more dilute conditions, NBu₄Ni(CAN)_{1.5} and NBu₄Ni(FAN)_{1.5} were prepared as brown powders with PXRD spectra matching their simulated PXRD patterns. Imperfections in the PXRD spectra of NBu₄Ni(CAN)_{1.5} were attributed to

impure reagent chloranilic acid (97%). Further efforts are under way to improve control over crystallinity and particle size via modulation of reaction conditions.

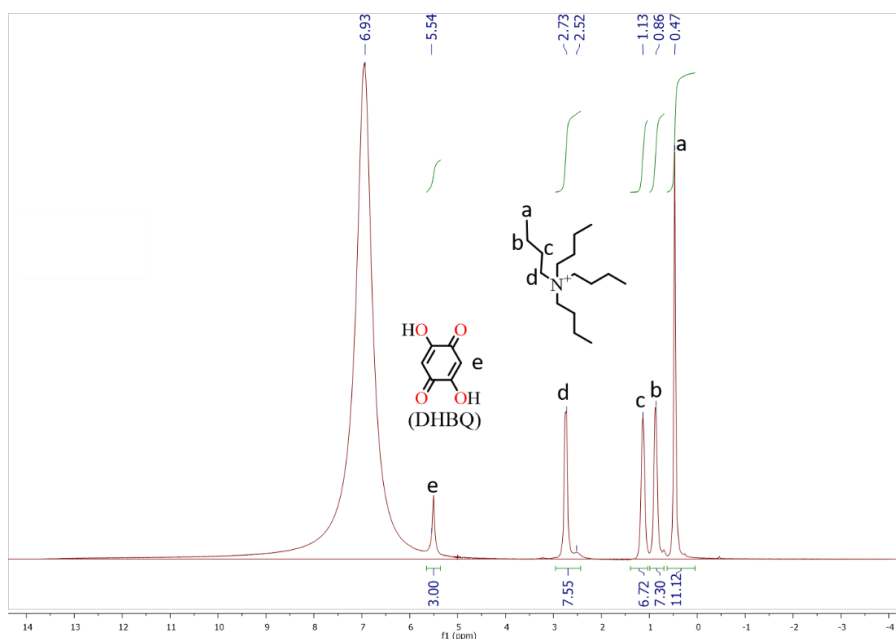


Figure 2-9. ^1H NMR of $\text{NBu}_4\text{NiDHBQ}_{1.5}$ in $\text{DMSO } D_6$ (1 ml) and four drops concentrated HCL to digest the sample. This sample was prepared with the DHBQ ligand by the methods described in this work.

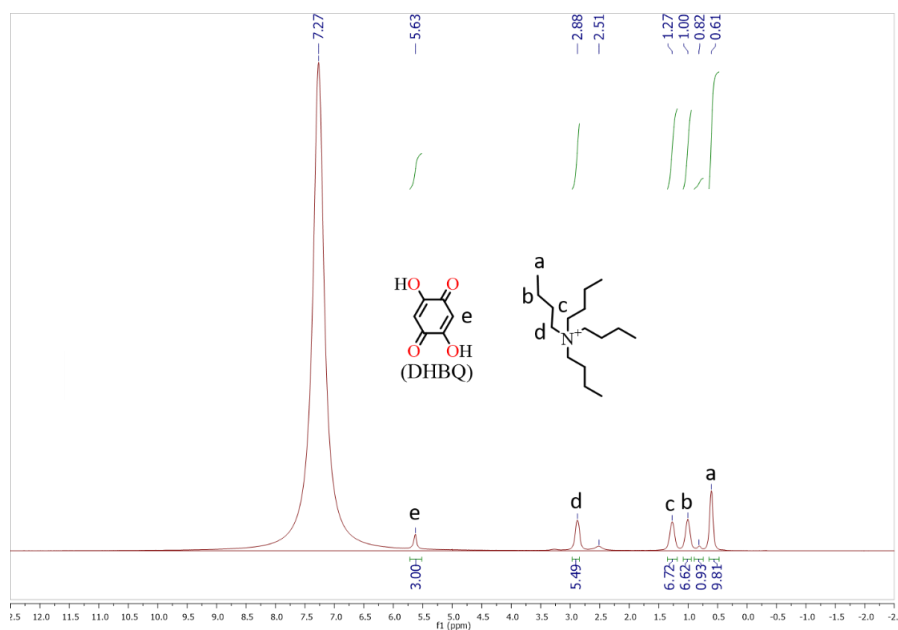


Figure 2-10 ^1H NMR of $\text{NBu}_4\text{NiDABQ}_{1.5}$ in $\text{DMSO } D_6$ (1 ml) and four drops concentrated HCL to digest the sample. This sample was prepared with the DABQ ligand by the hydrothermal method.

2-5. Conclusion

In summary, $\text{NBu}_4\text{MDHBQ}_{1.5}$ ($M = \text{Fe}, \text{Ni}, \text{Co}$) crystalline powders were prepared via a simple addition reaction of metal to ligand in boiling water. Via temperature regulation of addition, the products were uniform and pure according to XRD, FT-IR, SEM, EDS, ^1H NMR and EA. Most importantly, the straightforward synthesis utilizing the DHBQ ligand rather than in-situ generation of DHBQ was demonstrated with a greater than 10-fold scale up of product with improved yield up to 100% and with better elemental and PXRD agreement than that produced by the sealed glass vial reactor using DABQ. This synthesis was successfully demonstrated for Ni, Fe, Co and can reasonably be extended to other divalent metals. By substituting chloranilate or fluoranilate ligands for the DHBQ based Ni-MOFs, materials matching simulated PXRD were prepared. The present convenient of DHBQ ligand (and its derivatives) based MOFs will further promote their applications such as conductive MOFs and magnetic materials. Currently investigations into MOF syntheses extending to other metals, ligands, and ions are under way while exploiting the redox chemistry of $\text{NBu}_4\text{M}_2\text{DHBQ}_3$ ($M = \text{Fe}$ and Ni) for potential energy storage applications.

Table 2-1. Price comparison for DAHQ vs DHBQ ligand as of March 20, 2019.

Supplier	Chemical name	Purity	CAS #	Quantity	Price (USD)
Alfa Aesar	2,5-Diaminohydroquinone dihydrochloride	97%	24171-03-7	1 g	\$136.00/g
	2,5-dihydroxy-1,4-benzoquinone	98%	615-94-1	25 g	\$57.80 \$2.32/g
Sigma	2,5-Diaminohydroquinone dihydrochloride	>90%	24171-03-7	1 g	\$90.80/g
	2,5-dihydroxy-1,4-	98%	615-94-1	25 g	\$78.00

2-6. References

1. Sun, L.; Campbell, M. G.; Dincă, M., Electrically Conductive Porous Metal–Organic Frameworks. *Angew. Chem., Int. Ed.* **2016**, *55*, 3566.
2. Sheberla, D.; Sun, L.; Blood-Forsythe, M. A.; Er, S.; Wade, C. R.; Brozek, C. K.; Aspuru-Guzik, A.; Dinca, M., High electrical conductivity in Ni(3)(2,3,6,7,10,11-hexamino-triphenylene)(2), a semiconducting metal-organic graphene analogue. *J. Am. Chem. Soc.* **2014**, *136*, 8859.
3. Lahiri, N.; Lotfizadeh, N.; Tsuchikawa, R.; Deshpande, V. V.; Louie, J., Hexaaminobenzene as a Building Block for a Family of 2D Coordination Polymers *J. Am. Chem. Soc.* **2017**, *139*, 2119.
4. Feng, D.; Lei, T.; Lukatskaya, M. R.; Park, J.; Huang, Z.; Lee, M.; Shaw, L.; Chen, S.; Yakovenko, A. A.; Kulkarni, A.; Xiao, J.; Fredrickson, K.; Tok, J. B.; Zou, X.; Cui, Y.; Bao, Z., Robust and conductive two-dimensional metal–organic frameworks with exceptionally high volumetric and areal capacitance. *Nat. Energy* **2018**, *3*, 30.
5. Zhou, H. C.; Long, J. R.; Yaghi, O. M., Introduction to Metal–Organic Frameworks. *Chem. Rev.* **2012**, *112*, 673.
6. Sheberla, D.; Bachman, J. C.; Elias, J. S.; Sun, C. J.; Shao-Horn, Y.; Dinca, M., Conductive MOF electrodes for stable supercapacitors with high areal capacitance. *Nat. Mater.* **2017**, *16*, 220.
7. Tan, C.; Cao, X.; Wu, X. J.; He, Q.; Yang, J.; Zhang, X.; Chen, J.; Zhao, W.; Han, S.; Nam, G. H.; Sindoro, M.; Zhang, H., Recent Advances in Ultrathin Two-Dimensional Nanomaterials. *Chem. Rev.* **2017**, *117*, 6225.

8. Li, P.; Wang, B., Recent Development and Application of Conductive MOFs. *Isr. J. Chem.* **2018**, *58*, 1010.
9. Abrahams, B. F.; Hudson, T. A.; McCormick, L. J.; Robson, R., Coordination Polymers of 2,5-Dihydroxybenzoquinone and Chloranilic Acid with the (10,3)-a Topology. *Cryst. Growth Des.* **2011**, *11*, 2717.
10. Darago, L. E.; Aubrey, M. L.; Yu, C. J.; Gonzalez, M. I.; Long, J. R., Electronic Conductivity, Ferrimagnetic Ordering, and Reductive Insertion Mediated by Organic Mixed-Valence in a Ferric Semiquinoid Metal–Organic Framework. *J. Am. Chem. Soc.* **2015**, *137*, 15703.
11. Ziebel, M. E.; Darago, L. E.; Long, J. R., Control of Electronic Structure and Conductivity in Two-Dimensional Metal–Semiquinoid Frameworks of Titanium, Vanadium, and Chromium. *J. Am. Chem. Soc.* **2018**, *140*, 3040.
12. Murase, R.; Abrahams, B. F.; D'Alessandro, D. M.; Davies, C. G.; Hudson, T. A.; Jameson, G. N. L.; Moubaraki, B.; Murray, K. S.; Robson, R.; Sutton, A. L., Mixed Valency in a 3D Semiconducting Iron-Fluoranilate Coordination Polymer. *Inorg. Chem.* **2017**, *56*, 9025.
13. Abrahams, B. F.; Dharma, A. D.; Dyett, B.; Hudson, T. A.; Maynard-Casely, H.; Kingsbury, C. J.; McCormick, L. J.; Robson, R.; Sutton, A. L.; White, K. F., An indirect generation of 1D MII-2,5-dihydroxybenzoquinone coordination polymers, their structural rearrangements and generation of materials with a high affinity for H₂, CO₂ and CH₄. *Dalton Trans.* **2016**, *45*, 1339.

14. Morikawa, S.; Yamada, T.; Kitagawa, H., Crystal Structure and Proton Conductivity of a One-dimensional Coordination Polymer, $\{\text{Mn}(\text{DHBQ})(\text{H}_2\text{O})_2\}$. *Chem. Lett.* **2009**, 38, 654.

CHAPTER III

**REDOX ACTIVE NI-QUINONE MOFS AS A NOVEL LI ION INTERCALATION
CATHODE****3-1. Abstract**

The structure tunability and built-in porosity of metal organic frameworks (MOFs) materials makes them promising electrode materials to host metal ions. Herein, we present a redox active Ni-quinone MOFs (**LiNiDBQ_{1.5}**, DBQ = 2,5-dihydroxyl-1,4--benzoquinone) as a high-performance cathode material. The **LiNiDBQ_{1.5}** MOFs delivered outstanding battery performance in a Li metal battery, including a high charge capacity of 222 mAh/g at 0.1 C, high rate performance from 0.1 to 1.6 C, and stable cycling performance with 82% capacity retention after 1000 cycles, which represents one of the highest capacity and the most stable cycling MOFs cathode of those reported to date.

3-2. Introduction

Electrochemical energy storage devices play essential roles in storing and delivering efficient and reliable energy in portable devices, electric vehicles, and electricity grids that are pivotal to our daily life and the economic development of modern society.¹⁻² There have been continuous efforts in developing new electrode materials with improved performance and low cost to meet the increasing demand for energy storage.¹⁻² Recently, redox active organic electrode materials including conjugated carbonyls, conjugated sulfides, conjugated amine, conjugated thioethers, and nitrosyl radicals based oligomers and polymers have received increasing attention because of their structural tunability (achieving high capacities, optimal redox potential, and high stability), fast conversion charge/discharge mechanisms, resource abundance, and

potentially low costs.³⁻⁵ A number of ingeniously designed insoluble redox active organic salts/oligomer/polymer cathodes⁶⁻¹⁰ and anodes¹¹ have demonstrated outstanding cycling performance in both nonaqueous and aqueous rechargeable batteries.

Metal organic frameworks (MOFs) are a class of inorganic coordination polymeric materials consisting of bridging organic ligands and metal centers to form 2D and 3D topological frameworks, and have been applied in a broad array of applications including gas storage, sensors, and catalysis.¹² The structure tunability and built-in porosity of MOFs makes them promising electrode materials to host metal ions. However, the use of redox active MOFs as metal ion (such as Li^+ and Na^+) storage electrode materials still remains largely underdeveloped since the early report of the Zn based MOF-117 as an anode in 2006.¹³ Since then, a few MOFs anode materials,¹⁴⁻¹⁷ have demonstrated promising prospects including high charge capacities and relative stable cycling performance. Nevertheless, the development of MOFs cathode materials is still a forbidding challenge as reported MOFs cathode materials only demonstrated limited capacities ($< 150 \text{ mAh/g}$) and unsatisfactory cycling performance (< 100 cycles).¹⁸⁻²⁰ In addition, reported MOFs materials primarily employ metal based redox activity and do not fully take advantage of the structural features of MOFs materials such as structural tunability, intercalation properties, and ligand based multi-redox processes. There have been only a few examples of MOFs electrode materials using ligand based redox activity.^{15-16, 19-23} Among them, the $\text{Cu}(2,7\text{-AQDC})$ MOFs represents the state of art MOFs cathode utilizing the two electron redox process of its bridging dicarboxylate anthraquinone ligand.²⁰

The MOFs design consisting of redox active ligands (L_{redox}) as MOFs “strut” and earth abundant transition metals (TM, e.g. Ni, Fe, and Mn) as MOFs “node” could lead to high performance MOFs cathode materials for rechargeable batteries. Potential technological advantages of redox active TM- L_{redox} MOFs as cathode materials include (1) high stability and complete insolubility through strong metal-ligand dative coordination bonding, (2) high ion mobility through well-defined ion channels in MOFs structures,²⁰ (3) high charge capacity benefited from low weight and multi-redox changes of redox active ligands,²⁰ (4) high electrical conductivity through delocalized MOFs networks,²⁴⁻²⁶ and (5) tunability through Lewis acidity of transition metals and substituent effects of redox active ligands. Herein, we report a redox active Ni-quinone MOFs material (named **LiNiDBQ_{1.5}**) as a high-performance cathode material, which was conveniently prepared in a one-step solvothermal reaction and fully characterized by a suite of spectroscopies. The Ni-quinone MOFs cathode material demonstrated outstanding electrochemical performance in a Li metal battery, including a high charge capacity of 222 mAh/g at 0.1 C, high rate performance from 0.1 to 1.6 C, and stable cycling performance with 82% capacity retention after 1000 cycles at 0.4 C. The Ni-quinone MOFs represents the most stable cycling MOFs cathode material reported to date, highlighting the promising potential of redox active MOFs as cathode materials in rechargeable batteries.

3-3 Experimental

Chemicals and manipulations:

All chemicals were purchased from TCI, dried at 100 °C under reduced pressure , and used directly. All experimental operations were conducted under an Argon

atmosphere. Elemental analysis was done at Atlantic Microlab. ICP-MS was done on Thermo X Series 2 Quadrupole ICP-MS. SEM was done on a FEI Quanta FEG 650. XPS spectra was acquired on a Kratos Axis Ultra DLD equipped with a hemispherical analyzer.²⁷ Monochromatic aluminum K α was used as the X-ray source and an area of 300 nm x 700 nm was scanned. All acquisitions were collected at ultrahigh vacuum of 2×10^{-9} Torr or less. The spectra were analyzed using CasaXPS software and was standardized by calibrating the C(1s) peak to 284.8 eV. TEM images were acquired on a JEOL JEM-2800 instrument at an accelerating voltage of 80 keV and the images were analyzed using Gatan Micrograph software. The TEM samples were prepared by drop-casting an ethanol suspension of LiNiDBQ_{1.5} on 20 nm carbon film grids supported by an Au framework. Thermogravimetric analysis was performed on a TA Instruments TGA 2950 Thermogravimetric Analyzer at a heating rate of 10°C/min and a Nitrogen flow rate of 150 mL/min. FT-IR was measured on a Perkin Elmer Spectrum 100 FT-IR spectrometer with universal ATR sampling accessory. XRD was collected using a Panalytical X'Pert Pro X-ray Diffraction Spectrometer with monochromatic Cu K-alpha radiation using the High Score software program to index peaks and identify minerals. An autosorb iQ automated gas sorption analyzer (Quantachrome Instruments, USA) was used for BET measurements. XAS data were measured at the Stanford synchrotron radiation light source (SSRL) using beamline 9-3 with the storage ring operating at 3.0 GeV electron energy and 500 mA average current (further details are given in the supporting information). EIS was recorded using a Gamry potentiostat. XAS data were also measured at beamline 20-BM-B of Advanced Photon Source at Argonne National Laboratory.

Synthesis of LiNiDBQ_{1.5}. Dilithium 2,5-dihydroxy-1,4-benzoquinone (Li₂DBQ) (0.152 g, 1 mmol) was prepared according to literature.²⁷ At 80 °C, Li₂DBQ (0.152 g, 1.0 mmol) was dissolved in 10 mL absolute ethanol. Then NiCl₂ (0.085 g, 0.66 mmol) dissolved in 10 ml ethanol was added dropwise via cannula. The reaction mixture was stirred at reflux temperature for 4-5 hours then cooled to room temperature. The supernatant solvent was completely colorless indicating reaction completion. The desired product was separated from the solvent by vacuum filtration followed by rinsing with copious ethanol. A light red precipitate was collected. The product was dried at 80 °C in the vacuum oven then stored in an argon filled glove box. The yield was ca. 97.16% by mass. (0.200 g). Anal. Calcd. for LiNiDBQ_{1.5}·2H₂O: C 35.03, H 2.26, N 0.00; found C 35.27, H 2.33, N 0.00. FTIR (KBr pellets): 3450, 2924, 1520, 1346, 1383, 1262, 813, 769 cm⁻¹. ICP-MS calculated for LiNiDBQ_{1.5}: Li 2.25%, Ni 19.01%; found: Li 2.80%, Ni 20.6%. A N₂ adsorption study at 150 K yield a BET surface area of 324.32 m²/g for this material, indicating a pore volume = 1.58 cm³/g and a pore diameter D_v(d) = 3.14 nm.

Preparation of LiNiDBQ_{1.5} MOFs and Li₂DBQ cathode. Active material (60% by weight), Carbon black acetylene (30% by weight), and PTFE (10% by weight) were ground into a slurry with mortar and pestle by adding drops of ethanol. The slurry was cast onto aluminum foil by doctor blading and dried at 100 °C in the vacuum oven for 1 hour. 10 mm discs were punched out of the sheet and dried for an additional 1-2 hours in the 100 °C vacuum oven. The active material mass loading of the cathodes was 0.8 to 1.2 mg/cm².

Cyclic Voltammetry Studies of LiNiDBQ_{1.5}, Li₂DBQ, and H₂DBQ. A three-electrode solid CV technique was employed whereby Li foil was the counter and reference

electrodes and a prepared 10mm cathode disc was the working electrode. The electrodes were lowered into a 20 ml scintillation vial containing 5.0 ml 1.0 M LiTFSI electrolyte in 1:1 V:V DME:DOL solvent mixture. Voltammetry was started at the high voltage cutoff, scanned towards the negative region at a sweep rate of 0.1 mV/s to the low cutoff voltage then scanned back to the high voltage at the same rate to complete one cycle. All cyclic voltammetry experiments were conducted in an Ar filled glovebox due to the reactivity of Li metal and N₂. O₂ and H₂O levels were kept below 0.1 PPM.

EIS studies. Performed using a Gamry potentiostat by placing a coin cell containing the described active material inside a conductive clamp with cathode side attached to working electrode lead and with the anode side attached to counter/reference leads. Scanned from 10⁵ Hz to 10⁻¹ Hz with 10 points/decade. All EIS studies were performed on coin cells that had been cycled by charging and discharging for 5 cycles at 0.1 C charge rate.

Battery studies of LiNiDBQ_{1.5}, Li₂DBQ, and H₂DBQ. Battery testing was conducted using the Lanhe battery testing system with stainless steel cr2032 type coin cells containing Li metal anode, Celgard 2025 separator and 1.0 M LiTFSI in 1:1 V:V DME:DOL electrolyte. Open circuit Voltage was recorded as 2.94 V, so the batteries were first discharged to 1.40 V then charged to 3.40 V with ten minutes resting time between cycles. For long term cycling, the voltage window was restricted to 1.6 to 3.0 Volts to encourage cycling stability. The batteries were charged and discharged galvanostatically at different C rates calculated by multiplying the mass of active material in the electrode by the theoretical specific capacity of the cathode active material and

then multiplying this value by the desired C rate. A piece of Li metal disc was used as an anode in all coin cells to assure the cathode was the capacity limiting electrode.

X-ray Absorption Data collection and analysis

Beamline 9-3 at the Stanford synchrotron radiation light source (SSRL) was used to conduct X-ray absorption spectroscopy (XAS) measurements. A cryogenically cooled Si(220) double crystal was used as monochromator which was detuned to 50 % of flux maximum at the Ni K-edge to reduce the contribution from higher harmonics. A harmonic rejection mirror was employed to further eliminate the contamination of higher harmonics. N₂ filled ion chambers (I₀, in front of the sample and I₁/I₂ after the sample) for monitoring the intensity of the incident and transmitted x-rays. Samples were packed in 0.5 mm thick Aluminum sample holders with Kapton film window on either side. The reference compounds were diluted with boron nitride (~5% w/w) and finely ground before packing. The sample spectra were collected in transmission as well as fluorescence mode using a 30-element Ge detector (Canberra). Beamline energy was calibrated by measuring Ni foil spectrum and setting the first inflection point at 8333.0 eV. For internal calibration, XAS spectra of Ni foil (placed between I₁ and I₂ ion chambers) were recorded concomitantly with the sample measurements. XAS data of sample was closely monitored for any radiation damage.

The raw XAS data was reduced using the SamView program in SixPack software package (<http://www.sams-xrays.com/sixpack>). Data aligning/merging and background subtraction was done with Athena software (Demeter version 0.9.26) (Journal of synchrotron radiation, 2005, 12, 537-541.) and spectra were then normalized to edge-

jump. The background removal in k -space EXAFS data was achieved with a five-domain cubic spline. The resulting data, as $k^3\chi(k)$, was then Fourier transformed into r -space over a k range of 2.4 to 10.3 \AA^{-1} . Artemis (Demeter software version 0.9.26) was used for EXAFS fitting where theoretical EXAFS functions were calculated with FEFF6. FEFF input file was generated starting with the crystal structure corresponding to $(\text{NBu}_4)_2[\text{Ni}_2(\text{DBQ})_3]$ as reported by Brendon *et. al.* (Crystal Growth & Design, 2011, 11, 2717-2720, CCDC 839252) and elongating the distance for two of the first shell oxygens considering the Li interaction. A three shell EXAFS fit was carried out in r -space over an R' (non-phase-shift corrected bond distance which is shorter than actual bond distance by approximately 0.5 \AA) range of 1.0-4.0 \AA . The parameters generated by the best fit are listed in Table 2-1. The value of N (the path degeneracy or number of atoms in the shell) was fixed while the variables include average bond distance (R) between Ni and the scattering atom and mean square displacement of the bond distance). The value of E_0 (the energy which corresponds to the zero value of the photoelectron wave vector k) was also varied but restricted to a common value for each path. The value for amplitude reduction factor, S_0^2 , was extracted from the fit to the data of Ni foil and was fixed (0.87) during the fits.

3-4. Results and Discussion

Synthesis, Spectroscopic, and Electrochemical Studies of $\text{LiNiDBQ}_{1.5}$ MOFs

In order to construct the proposed redox active MOFs, 2,5-dihydroxyl-*p*-quinone (DBQ) was selected as a bridging ligand because of its two electron redox properties (Scheme 1) and low molecular weight (i.e. high charge capacity),²⁷ and chelating oxygen ligands to form strong dative metal-O coordination bonds.²⁸ Coordination polymers and

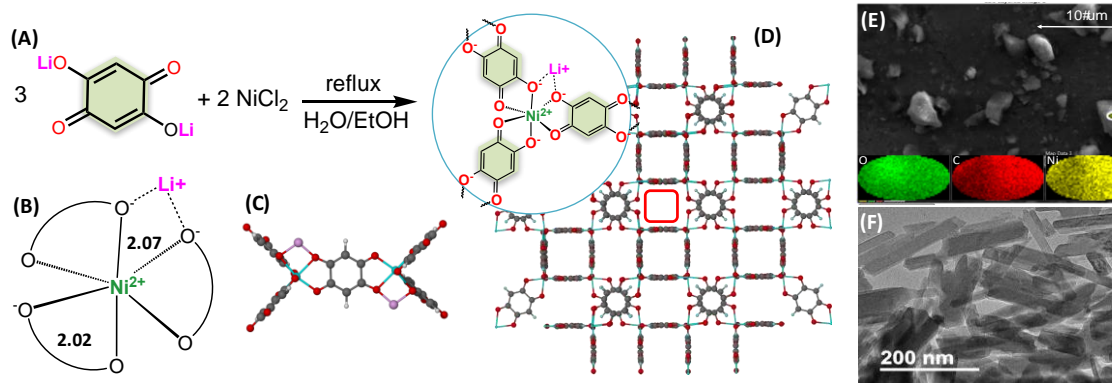


Figure 3-1. (A) Synthesis of **LiNiDBQ_{1.5}** MOFs; (B) Coordination sphere of the Ni center with labelled averaged Ni-O bond distances obtained from the EXAFS studies; (C) Coordination structural model showing one DBQ ligand bridging two Ni centers, Li (purple), Ni (green), C (black) and H (white); and (D) Proposed 3-dimensional structure model of the **LiNiDBQ_{1.5}** MOFs with Li⁺ ion omitted for clarity. (E) SEM and element mapping images of **LiNiDBQ_{1.5}** MOFs. (F) TEM image of **LiNiDBQ_{1.5}** MOFs.

MOFs based on transition metals and DBQ (or its derivatives) are well documented for their magnetic and conductive properties,^{26, 28-31} however, transition metal DBQ MOFs incorporated with alkali cations such as Li⁺ remain unknown for battery applications.

Based the consideration of hard/soft Lewis acid/base interactions to achieve robust metal ligand bonding strength, we chose to exploit Ni-DBQ MOFs²⁹ as a cathode material.

After deprotonation using LiOH, the resulting dilithium 2,5-dihydroxide-*p*-quinone (Li₂DBQ) can act as a bridging bidentate ligand using *ortho* C-O⁻ and C=O oxygen donors (Figure 3-1A) while introducing Li ions into the expected MOFs product. To form a stable octahedral Ni geometry while achieving a high loading of the redox active BDQ ligand, 1.5 :1 ratio of Li₂DBQ (1.5 equivalent) and NiCl₂ readily produce **LiNiDBQ_{1.5}** MOFs as a light red precipitate (Figure 3-1A). SEM studies (Figure 3-1E) revealed the morphology of **LiNiDBQ_{1.5}** MOFs as micro-particles. Further TEM studies revealed that individual micro-particles are aggregates composed by nano-plates with a size within 200 nm × 50 nm × 20 nm (Figure 3-1F). The formula of **LiNiDBQ_{1.5}** was determined using

elemental analysis and ICP-MS, confirming the ratio of Li, Ni, and DBQ ligand is 1:1:1.5. The **LiNiDBQ_{1.5}** MOFs has a BET surface area of 324.32 m²/g, indicating a Pore volume = 1.58 cm³/g and a pore diameter of 3.14 nm.

The X-ray absorption near-edge structure (XANES) studies for the Ni element confirmed that **LiNiDBQ_{1.5}** MOFs has Ni²⁺ metal centers with rising edge energy (at half-edge height) at 8343.4 eV (Figure 3A), which is comparable with the reference compounds, Ni(OH)₂. The edge energy of **LiNiDBQ_{1.5}** MOF is in between those of Ni foil (Ni⁰) and g-NiO(OH) (Ni^{3.6+}), further confirming the Ni²⁺ oxidation state in **LiNiDBQ_{1.5}** MOFs. The weak absorption pre-edge at 8333 eV in the Ni XANES spectra is associated with dipole-forbidden 1s-3d electron transition, consistent with an octahedral symmetry surrounding the Ni metal of **LiNiDBQ_{1.5}**. The strong peak at 8349 eV originated from dipole-allowed transition of 1s to unoccupied 4p. The local atomic structure information was extracted by fitting the extended X-ray absorption fine structure spectrum (EXAFS, Figure 3-2B). Figure 3-2B represents non-phase-shift corrected *r*-space EXAFS data (in which the radial distance is shorter than the actual bond distance by ~0.5 Å) along with the best fit. The details of the fitting procedure are described in the experimental along with the best fit parameters listed in Table 3-1. The first peak at apparent distance of 2.04 Å corresponds to the first shell O neighbors. Two Ni-O paths were used for the first shell corresponding to six O neighbors at 2.01±0.01 Å (Table 3-1). The second peak at 2.27 Å contains scattering contributions from the second shell carbons whereas most the amplitude in third peak is contributed by multi-leg scattering paths Ni-C-C (see Table 2-1

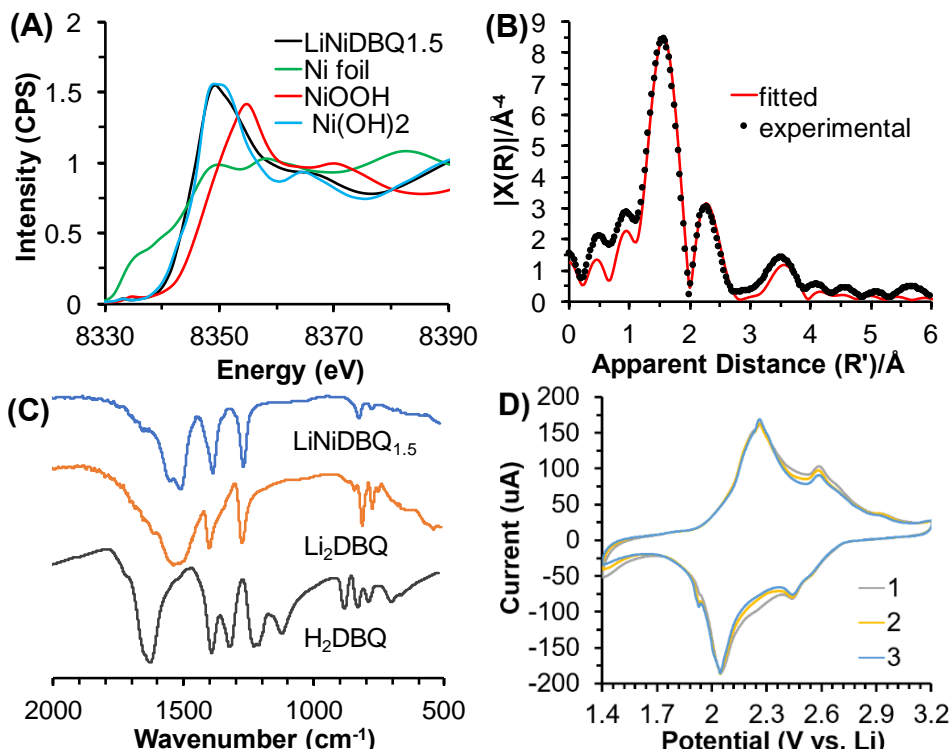


Figure 3-2. (A) Ni K-edge XANES spectra of the **LiNiDBQ_{1.5}** MOFs and Ni foil, Ni(OH)₂, and γ -NiO(OH); (B) Ni K-edge EXFAS spectra of the **LiNiDBQ_{1.5}** MOFs: experimental spectrum (black dotted curve) and fitted spectrum (red curve); (C) IR spectra of **LiNiDBQ_{1.5}** MOFs, Li₂DBQ, and H₂DBQ; and (D) CV of **LiNiDBQ_{1.5}**.

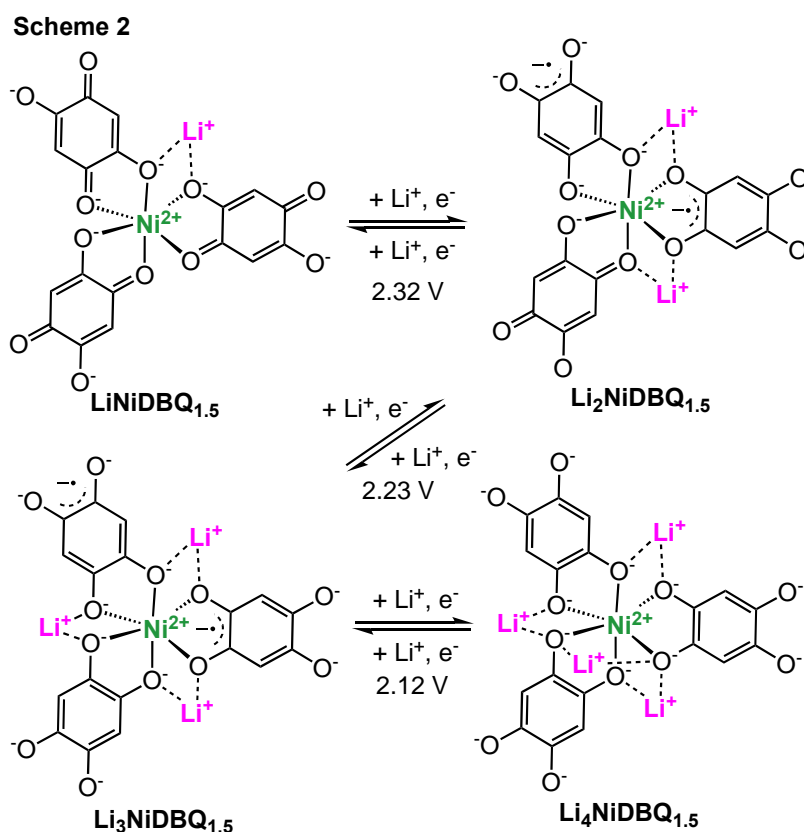
for details). The Ni-O bond distances determined by the EXAFS studies are comparable to those (2.04 Å) observed in the reported (NBu₄)NiDBQ_{1.5}MOF.²⁹ All Ni atoms are bridged by the DBQ ligand with a distance of 7.81 Å (Figure 3-1C) to form a three dimensional topology, which is believed to be identical as (NBu₄)NiDBQ_{1.5} MOF (Figure 3-1D).²⁹ The square open channels along the b axis are clearly visualized in the proposed three dimensional topology of **LiNiDBQ_{1.5}** (Figure 3-1D) and is believed to enable facile Li⁺ ion transportation.

The structure and bonding features of **LiNiDBQ_{1.5}** MOFs were further characterized using Fourier-transform infrared spectroscopy (FTIR) (Figure 3-2C, black curve). **LiNiDBQ_{1.5}** MOFs displays two carbonyl stretching frequency at 1542 and 1506

cm^{-1} . The relative less intensive absorption at the higher wavenumber (1542 cm^{-1}) is assigned as one C=O group in the DBQ ligand which is only ligated with Ni while the relative more intensive absorption at the lower wavenumber (1506 cm^{-1}) is assigned to two C=O groups in the two DBQ ligands which not only bond with Ni but also interact with Li ion (Figures 3-1A and 3-1B). These C=O stretching absorptions are comparable to those of Li_2DQB (a broad absorption at 1536 cm^{-1} ; Figure 3-2C, blue trace) but weaker than those observed in H_2DBQ (1631 cm^{-1} ; Figure 3-3C, red trace). Similarly, **$\text{LiNiDBQ}_{1.5}$** MOFs exhibits a lower C-O stretching frequency at 1390 cm^{-1} than 1402 cm^{-1} for Li_2DQB and 1392 cm^{-1} for H_2DQB . These results indicate the stronger metal (Lewis acid) and ligand (Lewis base) bonding interactions in **$\text{LiNiDBQ}_{1.5}$** MOFs than the Li_2DQB ligand and the H_2DBQ precursor, which is attributed to the greater Lewis acidity of Ni^{2+} than Li^+ and H^+ .

In the cyclic voltammogram, **$\text{LiNiDBQ}_{1.5}$** MOFs displays two-electron and one-electron redox couples at 2.16, and 2.52 V respectively (all redox potentials reported are versus to Li in this study, Figure3-2D) at a scan rate of 0.1 mV/s. It is proposed that **$\text{LiNiDBQ}_{1.5}$** MOFs can sequentially undergo DBQ ligand-based reductions as shown in Scheme 2, accompanying with Li^+ ion transfers. It is believed that the Li ions are positioned around the Ni metal with weak bonding interactions with the DBQ ligands.²⁷ Due to the stronger Lewis acid and Lewis base interactions, **$\text{LiNiDBQ}_{1.5}$** MOFs has a more positive average potential at 2.30 V than that of the Li_2DBQ ligand precursor (2.05 V) by 180 mV. **$\text{LiNiDBQ}_{1.5}$** was scanned from 3.2 V to 1.4 V then back to 3.2 V for three cycles. Reversible processes were clearly defined with reversible a single electron mechanism at 2.45V/2.60V, and a reversible two electron mechanism at 2.05 V/2.27 V.

On the other hand, Li_2DBQ was scanned from 3.5 V to 1.5 V then back to 3.5 V for three cycles. A quasi-reversible two-electron reduction/oxidation occurred at 2.1/2.0 Volt. a nonreversible oxidation occurred at 3.27 V that became more pronounced with each cycle. The redox active ligand in $\text{LiNiDBQ}_{1.5}$ MOFs, H_2DBQ , was scanned from 3.5 V to 1.5 V then back to 3.5 V for one cycle. Further cycles were not possible due to solvation of the active material into the electrolyte. An asymmetric reduction/oxidation occurs with a two-electron reduction at 2.04 V. Two single electron oxidations at 2.30 V and 2.54 V. Another two one-electron oxidations were observed at 3.21 V and 3.50 V. A very weak reduction at 3.05 V was also observed. The more positive redox potential of $\text{LiNiDBQ}_{1.5}$ MOFs is advantageous to have a higher cell voltage than Li_2DQB . In addition, $\text{LiNiDBQ}_{1.5}$ MOFs exhibits more stable CV scans than Li_2DQB and H_2DBQ because of



its superior insolubility and structural stability (Figure 3-2D). The CV of the H₂DBQ precursor could only be run for one cycle due to dissolution.

Battery Studies of LiNiDBQ_{1.5} MOFs

The battery performance of LiNiDBQ_{1.5} MOFs as cathode material was studied in coin cells using a Li disc as anode and 1.0 M LiTFSI in 1:1 V:V DME:DOL as supporting electrolyte. According to the CV study (Figure 3-2D and Scheme 2), the LiNiDBQ_{1.5}/Li battery has a cell voltage of 2.23 V) and allow for reversible intercalation of three Li ions for each Ni coordination unit. The battery was cycled between 3.5 and 1.4 V cutoff voltages. A single discharge with a capacity of 274 mAh/g was observed. In the second cycle a discharge capacity of 244 mAh/g was observed at a rate of 0.1 C, corresponding to 82% utilization of the 294.78 mAh/g theoretical capacity. At 1.6 C, the capacity was below 122 mAh/g (50% of 0.1C capacity). The nonreversible capacity observed in the first cycle is attributed to volumetric changes on the electrode and complete lithiation of the active material. Long term cycling was performed at 0.4 C for 1000 cycles. Li₂DBQ: The performance of this coordination polymer as a cathode active material is reported elsewhere.³² In our trial, 90.7 mAh/g at 25 mA/g was attained during the first cycle. 69.2 mAh/g was attained during the second cycle and continuous capacity decay was observed thereafter. The theoretical capacity for this active material (348.33 mAh/g) was not nearly achieved. The redox active ligand H₂DBQ was also tested. The performance of this organic molecule as a cathode active material is reported elsewhere.³³ The capacity decay was immediate and the capacity utilization was very low due to poor cyclability caused by high charge transfer resistance and solubility of H₂DBQ in the electrolyte. The

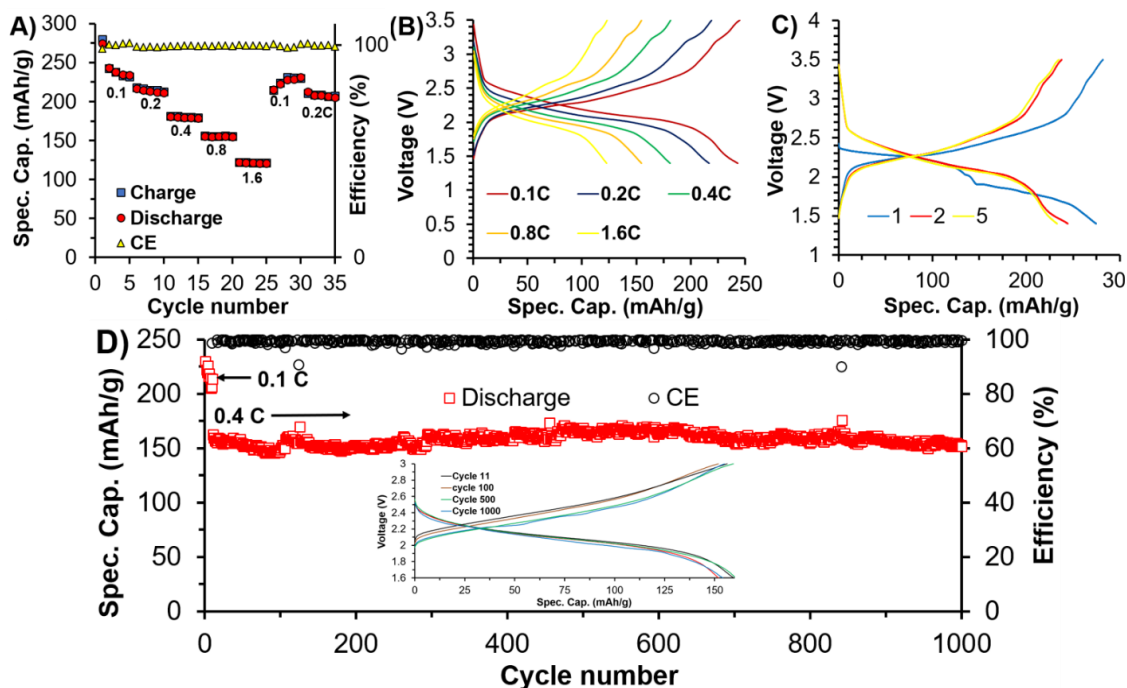


Figure 3-3. (A) Rate performance from 0.1 to 1.6 C; (B) Representative charge/discharge curves at various C rates; (C) Initial and reversible discharging/charging profiles.; (D) Discharge capacity and coulombic efficiency over cycling number at 0.4 C, inset showing charge discharge curves at specified cycle numbers.

LiNiDBQ_{1.5} battery exhibited good rate performance from 0.1 to 1.6 C with coulombic efficiencies of near 100% for all current densities (Figure 3-3A). The battery delivered a reversible capacity of 222 mAh/g discharge capacity at 0.1 C out of a theoretical capacity of 294.78 mAh/g and still achieved 110 mAh/g at 1.6 C. Representative charge/discharge curves are shown in Figure 3-3B. In stark contrast, the Li₂DBQ ligand with a theoretical capacity of 446.8 mAh/g could be only utilized at a discharge capacity of ca. 67.4 mAh/g at 25 mA/g. H₂DBQ could not be cycled under similar conditions due to its high solubility in electrolytes and large charge transfer resistance. In addition, rate performance of the **LiNiDBQ_{1.5}/Li** battery is also much better than the Li₂DBQ/Li battery. EIS studies (Figure 3-4A-C) revealed that the charge transfer resistances of both charged (125 Ω•cm²) and discharged (90 Ω•cm²) states of **LiNiDBQ_{1.5}** are at least 6

times smaller than those of Li_2DBQ (1330 and $782 \Omega \cdot \text{cm}^2$ for discharged and charged states, respectively), and further at least two orders of magnitude smaller than those of H_2DBQ (1.2×10^4 and $15 \times 10^4 \Omega \cdot \text{cm}^2$ for discharged and charged states, respectively). It is believed that the outstanding electrical conductivity of $\text{LiNiDBQ}_{1.5}$ is attributed to the π -d conjugation within its three-dimensional MOFs structure.^{24-26, 34}

The long-term performance of the $\text{LiNiDBQ}_{1.5}/\text{Li}$ battery was tested at 0.4 C. The battery demonstrated outstanding cycling performance, achieving 96% capacity retention of the initial 159 mAh/g after 1000 cycles (Figure 3-3D). For comparison, a $\text{Li}_2\text{DBQ}/\text{Li}$ battery was studied under similar conditions. The $\text{Li}_2\text{DBQ}/\text{Li}$ battery has a lower cell voltage, 2.05 V. In contrast, under similar test conditions, the capacity of the $\text{Li}_2\text{DBQ}/\text{Li}$ battery faded by 17.6% in only ten cycles at 25mA/g which is consistent with the

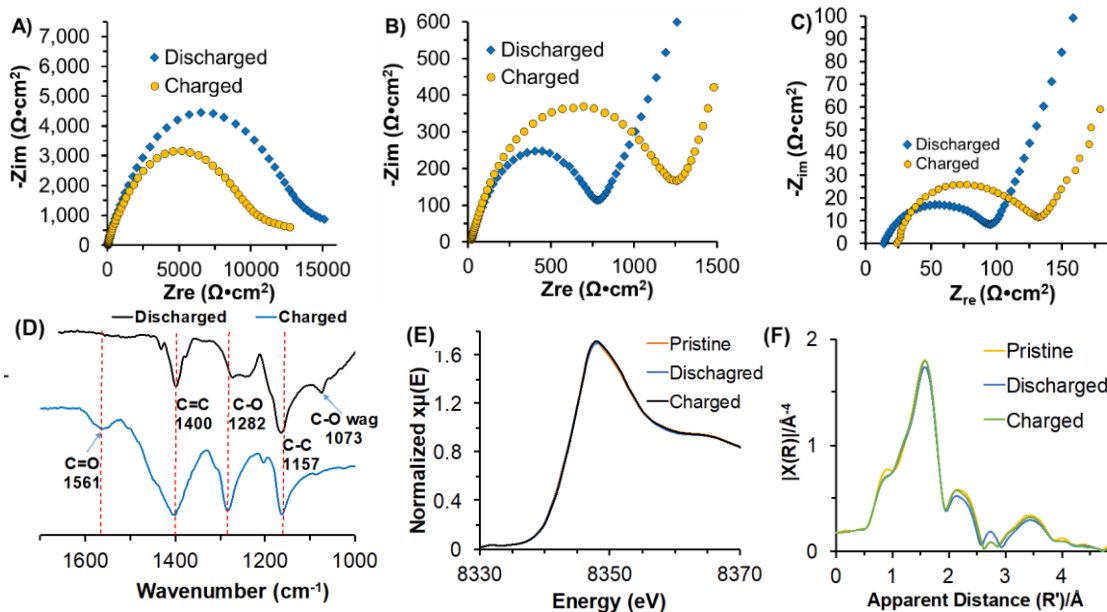


Figure 3-4. Nyquist plots for coin cells containing (A) H_2DBQ , (B) Li_2DBQ , and (C) $\text{LiNiDBQ}_{1.5}$. FTIR (D), and XANES (E) and EXFAS (F) studies of the charged and discharged states of the $\text{LiNiDBQ}_{1.5}$ MOFs cathode.

previous report.²⁷ The superior cycling stability of **LiNiDBQ_{1.5}** over Li₂DBQ and H₂DBQ is definitely attributed to its insolubility and structural stability as a result of the coordinating interactions of the Ni²⁺ Lewis acid and the DBQ Lewis base. As displayed in Figure 3-6, both charged and discharged states of **LiNiDBQ_{1.5}** are insoluble in the LiTFSI supporting electrolyte, which is in stark contrast to those of Li₂DBQ and H₂DBQ.

To further understand the charge/discharge mechanism of the **LiNiDBQ_{1.5}** MOFs cathode, the charged and discharged states were studied by FTIR, X-ray diffraction (XRD), XANES, and EXAFS (Figure 3-4D-G). In FTIR studies (Figure 3-4D), compared to the charged state, the C=O stretches (1561 cm⁻¹) completely disappeared in the charged state of the **LiNiDBQ_{1.5}** MOFs cathode, accompanied with additional spectroscopic changes observed for other vibrational modes of C=C and C-O bonds. It should be noted that the charged state of the **LiNiDBQ_{1.5}** MOFs cathode exhibited different spectroscopic features than pristine **LiNiDBQ_{1.5}** MOFs, which is attributed to the binder and electrolyte residues in the **LiNiDBQ_{1.5}** MOFs cathode. The FTIR results confirmed the complete formation of quinolate groups in the DBQ ligand in the discharged state (**Li₄NiDBQ_{1.5}** in Scheme 2). The spectroscopic observations confirmed that crystalline morphology of the cathode maintained intact during cycling, which is attributed to the porous nature of the cathode materials (Figure 3-1D), resembling traditional Li ion intercalation cathode materials. In the XANES studies (Figure 3-4F), charged and discharged states of the cathode displayed nearly identical Ni K edge spectroscopic features as the pristine material, and thus maintained the Ni²⁺ oxidation state, which is consistent with the DBQ ligand based redox chemistry. In addition, there was no apparent change observed in the Ni K-edge EXFAS spectra of the pristine **LiNiDBQ_{1.5}**, the charged and discharged states

of the **LiNiDBQ_{1.5}** cathode (Figures 3-4G), which confirms the retained local coordination sphere of the Ni metal during the charge/discharge processes and also corroborates the intercalation nature of the **LiNiDBQ_{1.5}** cathode.

3-5. Conclusions

In summary, redox active **LiNiDBQ_{1.5}** MOFs was fully characterized and applied as a Li⁺ ion storage cathode material. The high rate performance and outstanding long cycling stability of **LiNiDBQ_{1.5}** MOFs are benefited from facile reversible redox changes of the DBQ quinone ligand, and strong dative chemical interactions between the Ni metal and the ligand and the resulting insolubility. Because of rich structural tunability including using different metals and redox active ligands, the demonstrated redox active MOFs material will open a new regime in designing high performance ion storage cathode and anode materials for rechargeable batteries. Particularly, it is highly promising to develop redox active MOF cathode materials for reversible integration of multivalent ions such as Mg²⁺, Ca²⁺ and Al³⁺, which represents an ongoing challenge in the field of rechargeable batteries.

3-6 Acknowledgements

Sheraz Gul and Junko Yano, Molecular Biophysics and Integrated Bioimaging Division, Lawrence Berkeley National Laboratory, California, 94720, United States for XANES and XAFS data collection.

Nabajit Lahiri and Professor Janis Louie, Department of Chemistry, University of Utah, Salt Lake City, Utah, 84122, United States for XPS data collection.

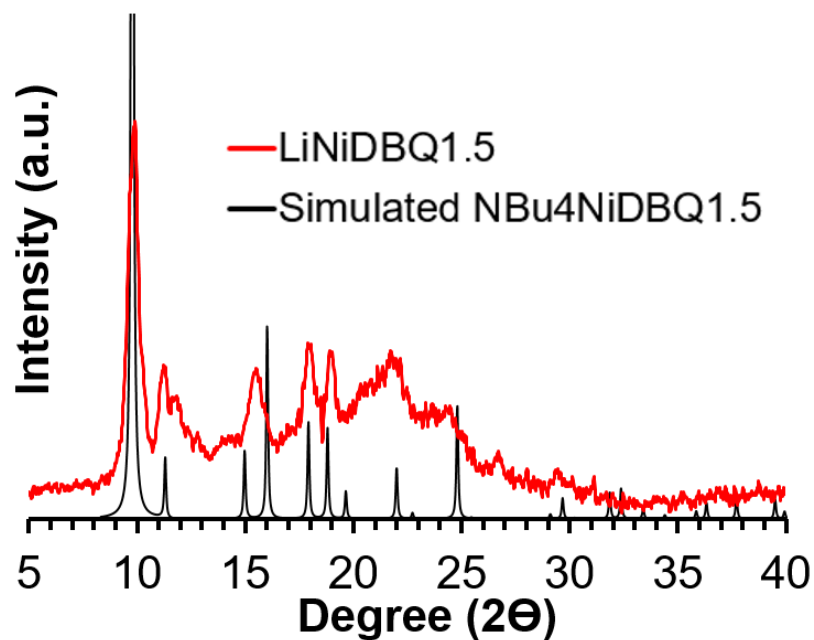


Figure 3-5: PXR D Spectrum comparison of $\text{LiNiDBQ}_{1.5}$ compared to the reference compound $\text{NBu}_4\text{NiDBQ}_{1.5}$.



Figure 3-6. Photography of charged and discharged electrodes in 1.0 M LiTFSI in 1:1 V:V DME:DOL of H_2DBQ , Li_2DBQ , and $\text{Li}_2\text{Ni}_2\text{DBQ}_3$ (from left to right).

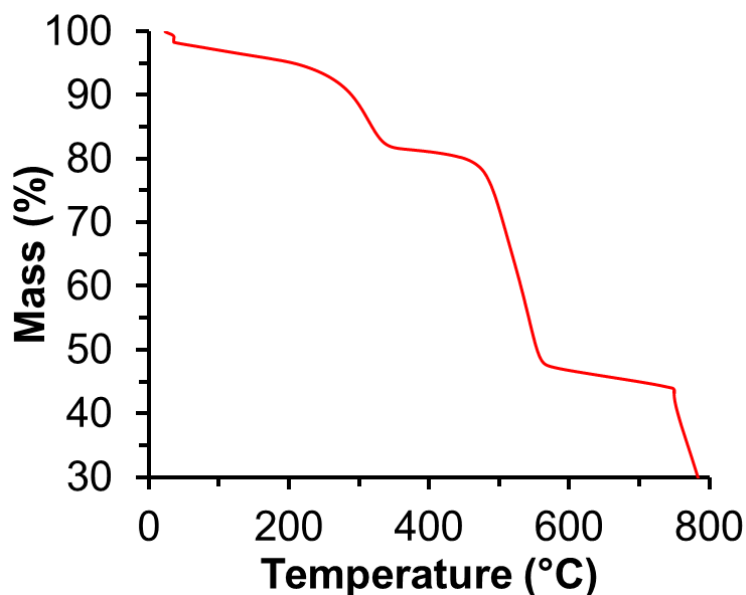


Figure 3-7: Thermogravimetric analysis of **LiNiDBQ_{1.5}** under N₂ with 10 °C per minute ramp rate. The initial weight loss is due to the crystalline water.

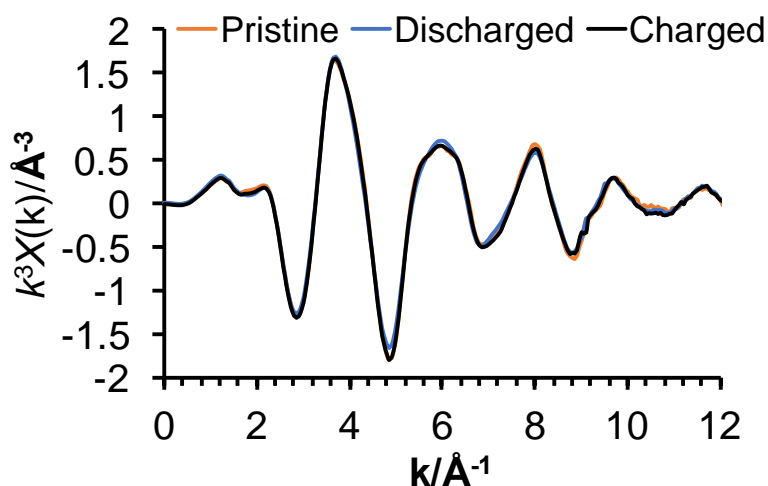


Figure 3-8. Fourier-transformed Ni K-edge K-space EXFAS spectra of the **LiNiDBQ_{1.5}** MOFs.

Table 3-1. Fitting parameters for the Ni K-edge EXFAS spectra of the LiNiDBQ_{1.5} MOFs

Sample	Path	R (Å)	N	σ^2 (10^{-3} Å ²)	R-factor (%)	ΔE_0 (eV)
LiNiDBQ _{1.5}	Ni-O	2.04±0.01	6	4.76±0.74	2.10	-0.56±1.67
	Ni-C	2.77±0.01	6	7.18±3.17		
	Ni-C	4.17±0.01	6	7.18±0.25		

3-6. References

1. Armand, M.; Tarascon, J. M., Building better batteries. *Nature* **2008**, *451*, 652-657.
2. Dunn, B.; Kamath, H.; Tarascon, J.-M., Electrical Energy Storage for the Grid: A Battery of Choices. *Science* **2011**, *334*, 928.
3. Poizot, P.; Dolhem, F., Clean energy new deal for a sustainable world: from non-CO₂ generating energy sources to greener electrochemical storage devices. *Energy Environ. Sci.* **2011**, *4*, 2003-2019.
4. Liang, Y.; Tao, Z.; Chen, J., Organic Electrode Materials for Rechargeable Lithium Batteries. *Adv. Energy Mater.* **2012**, *2*, 742-769.
5. Muench, S.; Wild, A.; Friebe, C.; Häupler, B.; Janoschka, T.; Schubert, U. S., Polymer-Based Organic Batteries. *Chem. Rev.* **2016**, *116*, 9438-9484.
6. Song, Z.; Qian, Y.; Gordin, M. L.; Tang, D.; Xu, T.; Otani, M.; Zhan, H.; Zhou, H.; Wang, D., Polyanthraquinone as a Reliable Organic Electrode for Stable and Fast Lithium Storage. *Angew. Chem. Int. Ed.* **2015**, *54*, 13947-13951.
7. Renault, S.; Gottis, S.; Barrès, A.-L.; Courty, M.; Chauvet, O.; Dolhem, F.; Poizot, P., A green Li-organic battery working as a fuel cell in case of emergency. *Energy Environ. Sci.* **2013**, *6*, 2124-2133.
8. Wang, S.; Wang, L.; Zhu, Z.; Hu, Z.; Zhao, Q.; Chen, J., All Organic Sodium-Ion Batteries with Na₄C₈H₂O₆. *Angew. Chem. Int. Ed.* **2014**, *53*, 5892-5896.
9. Fan, X.; Wang, F.; Ji, X.; Wang, R.; Gao, T.; Hou, S.; Chen, J.; Deng, T.; Li, X.; Chen, L.; Luo, C.; Wang, L.; Wang, C., A Universal Organic Cathode for Ultrafast Lithium and Multivalent Metal Batteries. *Angew. Chem. Int. Ed.* **2018**, *57*, 7146-7150.

10. Otteny, F.; Kolek, M.; Becking, J.; Winter, M.; Bieker, P.; Esser, B., Unlocking Full Discharge Capacities of Poly(vinylphenothiazine) as Battery Cathode Material by Decreasing Polymer Mobility Through Cross-Linking. *Adv. Energy Mater.* **2018**, *8*, 1802151.
11. Liang, Y.; Jing, Y.; Gheyhani, S.; Lee, K.-Y.; Liu, P.; Facchetti, A.; Yao, Y., Universal quinone electrodes for long cycle life aqueous rechargeable batteries. *Nature Materials* **2017**, *16*, 841.
12. Zhou, H.-C.; Long, J. R.; Yaghi, O. M., Introduction to Metal–Organic Frameworks. *Chem. Rev.* **2012**, *112*, 673-674.
13. Li, X.; Cheng, F.; Zhang, S.; Chen, J., Shape-controlled synthesis and lithium-storage study of metal-organic frameworks $Zn_4O(1,3,5\text{-benzenetribenzoate})_2$. *J. Power Sources* **2006**, *160*, 542-547.
14. Gou, L.; Hao, L.-M.; Shi, Y. X.; Ma, S.-L.; Fan, X.-Y.; Xu, L.; Li, D.-L.; Wang, K., One-pot synthesis of a metal–organic framework as an anode for Li-ion batteries with improved capacity and cycling stability. *J. Solid State Chem.* **2014**, *210*, 121-124.
15. Ogihara, N.; Yasuda, T.; Kishida, Y.; Ohsuna, T.; Miyamoto, K.; Ohba, N., Organic Dicarboxylate Negative Electrode Materials with Remarkably Small Strain for High-Voltage Bipolar Batteries. *Angew. Chem. Int. Ed.* **2014**, *53*, 11467-11472.
16. Park, J.; Lee, M.; Feng, D.; Huang, Z.; Hinckley, A. C.; Yakovenko, A.; Zou, X.; Cui, Y.; Bao, Z., Stabilization of Hexaaminobenzene in a 2D Conductive Metal–Organic Framework for High Power Sodium Storage. *J. Am. Chem. Soc.* **2018**.
17. Li, C.; Hu, X.; Tong, W.; Yan, W.; Lou, X.; Shen, M.; Hu, B., Ultrathin Manganese-Based Metal–Organic Framework Nanosheets: Low-Cost and Energy-Dense

Lithium Storage Anodes with the Coexistence of Metal and Ligand Redox Activities. *ACS Appl. Mater. Interfaces* **2017**, *9*, 29829-29838.

18. Combarieu, G. d.; Hamelet, S.; Millange, F.; Morcrette, M.; Tarascon, J.-M.; Férey, G.; Walton, R. I., In situ Fe XAFS of reversible lithium insertion in a flexible metal organic framework material. *Electrochem. Commun.* **2009**, *11*, 1881-1884.

19. Nagarathinam, M.; Saravanan, K.; Phua, E. J. H.; Reddy, M. V.; Chowdari, B. V. R.; Vittal, J. J., Redox-Active Metal-Centered Oxalato Phosphate Open Framework Cathode Materials for Lithium Ion Batteries. *Angew. Chem. Int. Ed.* **2012**, *51*, 5866-5870.

20. Zhang, Z.; Yoshikawa, H.; Awaga, K., Monitoring the Solid-State Electrochemistry of Cu(2,7-AQDC) (AQDC = Anthraquinone Dicarboxylate) in a Lithium Battery: Coexistence of Metal and Ligand Redox Activities in a Metal–Organic Framework. *J. Am. Chem. Soc.* **2014**, *136*, 16112-16115.

21. Zhang, Z.; Yoshikawa, H.; Awaga, K., Discovery of a “Bipolar Charging” Mechanism in the Solid-State Electrochemical Process of a Flexible Metal–Organic Framework. *Chem. Mater.* **2016**, *28*, 1298-1303.

22. Shimizu, T.; Wang, H.; Tanifuji, N.; Matsumura, D.; Yoshimura, M.; Nakanishi, K.; Ohta, T.; Yoshikawa, H., Rechargeable Batteries Based on Stable Redox Reactions of Disulfide Included in a Metal–Organic Framework as Ligands. *Chem. Lett.* **2018**, *47*, 678-681.

23. Park, J.; Lee, M.; Feng, D.; Huang, Z.; Hinckley, A. C.; Yakovenko, A.; Zou, X.; Cui, Y.; Bao, Z., Stabilization of Hexaaminobenzene in a 2D Conductive Metal–Organic Framework for High Power Sodium Storage. *J. Am. Chem. Soc.* **2018**, *140*, 10315-10323.

24. Sheberla, D.; Sun, L.; Blood-Forsythe, M. A.; Er, S.; Wade, C. R.; Brozek, C. K.; Aspuru-Guzik, A.; Dinca, M., High electrical conductivity in Ni(3)(2,3,6,7,10,11-hexamino-triphenylene)(2), a semiconducting metal-organic graphene analogue. *J Am Chem Soc* **2014**, *136*, 8859-62.
25. Lahiri, N.; Lotfizadeh, N.; Tsuchikawa, R.; Deshpande, V. V.; Louie, J., Hexaaminobenzene as a building block for a Family of 2D Coordination Polymers. *J. Am. Chem. Soc.* **2017**, *139*, 19-22.
26. Darago, L. E.; Aubrey, M. L.; Yu, C. J.; Gonzalez, M. I.; Long, J. R., Electronic Conductivity, Ferrimagnetic Ordering, and Reductive Insertion Mediated by Organic Mixed-Valence in a Ferric Semiquinoid Metal–Organic Framework. *J. Am. Chem. Soc.* **2015**, *137*, 15703-15711.
27. Xiang, J.; Chang, C.; Li, M.; Wu, S.; Yuan, L.; Sun, J., A Novel Coordination Polymer as Positive Electrode Material for Lithium Ion Battery. *Crystal Growth & Design* **2008**, *8*, 280-282.
28. Wroblewski, J. T.; Brown, D. B., Synthesis, Magnetic-Susceptibility, and Mossbauer-Spectra of Iron(III) Dimers and Iron(II) Polymers Containing 2,5-Dihydroxy-1,4-Benzoquinones. *Inorg. Chem.* **1979**, *18*, 498-504.
29. Abrahams, B. F.; Hudson, T. A.; McCormick, L. J.; Robson, R., Coordination Polymers of 2,5-Dihydroxybenzoquinone and Chloranilic Acid with the (10,3)-a Topology. *Crystal Growth & Design* **2011**, *11*, 2717-2720.
30. DeGayner, J. A.; Wang, K.; Harris, T. D., A Ferric Semiquinoid Single-Chain Magnet via Thermally-Switchable Metal–Ligand Electron Transfer. *J. Am. Chem. Soc.* **2018**, *140*, 6550-6553.

31. Min, K. S.; Rhinegold, A. L.; Miller, J. S., Tris(chloranilato)ferrate(III) Anionic Building Block Containing the (Dihydroxo)oxodiiron(III) Dimer Cation: Synthesis and Characterization of
[(TPA)(OH)FeIII(FeIII(OH)(TPA))][Fe(CA)₃]_{0.5}(BF₄)_{0.5}·1.5MeOH·H₂O [TPA = tris(2-pyridylmethyl)amine; CA = chloranilate]. *J. Am. Chem. Soc.* **2006**, *128*, 40-41.
32. Xiang, J. F.; Chang, C. X.; Li, M.; Wu, S. M.; Yuan, L. J.; Sun, J. T., A novel coordination polymer as positive electrode material for lithium ion battery. *Crystal Growth & Design* **2008**, *8*, 280-282.
33. Hanyu, Y.; Ganbe, Y.; Honma, I., Application of quinonic cathode compounds for quasi-solid lithium batteries. *J. Power Sources* **2013**, *221*, 186-190.
34. Kambe, T.; Sakamoto, R.; Hoshiko, K.; Takada, K.; Miyachi, M.; Ryu, J. H.; Sasaki, S.; Kim, J.; Nakazato, K.; Takata, M.; Nishihara, H., pi-Conjugated nickel bis(dithiolene) complex nanosheet. *J Am Chem Soc* **2013**, *135*, 2462-5.

CHAPTER IV
A HIGH CAPACITY IRON QUINONE METAL ORGANIC FRAMEWORK
FEATURING METAL AND LIGAND REDOX PROCESSES
FOR LI METAL ORGANIC BATTERIES

4-1. Abstract

Herein, rational synthesis of Metal Organic Frameworks (MOFs) was used to construct LiFeDBQ_{1.5} MOFs material. The title compound was completely chemically and electrochemically characterized. Ultra-high capacities of 275 mAh/g were achieved due to a three-electron organic quinone/enolate and metallic Fe²⁺/Fe³⁺ reversible redox reactions. The involvement of Fe²⁺/Fe³⁺ was proven unambiguously via XPS and Mossbauer characterization. The added metal redox raised the overall voltage of LiFeDBQ_{1.5} above 2.5 V vs Li and allowed fantastic rate capabilities in tested coin cell devices.

4-2. Introduction

In order to construct the proposed redox active MOFs, 2,5-dihydroxy-1,4-benzoquinone (H₂DBQ) was selected as a bridging ligand due to its facile two electron quinone/enolate redox mechanism,¹⁻⁴ low molecular weight, and ability to bridge metal centers in continuous frameworks via symmetric bis ortho C-O and C=O chelates.⁵ The electrochemical reversibility and plausibility of using this ligand in static batteries has been demonstrated in Li and Na-ion batteries by utilizing the Li or Na Salts of H₂DBQ as electrode active material.⁶⁻⁸ On the other hand, Coordination polymer materials utilizing the H₂DBQR₂ (R=H, Cl, Br, NO₂, F) ligand have not been thoroughly investigated for energy storage applications despite extensive documentation on their magnetic and

conductive properties.⁹⁻²⁰ Electronic conductivity is fundamentally important to battery electrodes.²¹⁻²³ Out of all reported materials based on the H₂DBQR₂ ligand, only those prepared with Fe²⁺ precursors led to robin-day class II mixed valent M²⁺/M³⁺ or L²⁻L³⁻ due to spontaneous charge transfer from metal to ligand.^{20, 24} Endowing materials with mixed valency has been a useful strategy for improving charge delocalization and electronic conductivity for semiconductors.²⁵ As such, the highest conductivity materials of this class are mixed valence (H₃O)H₂O(PHZ)₃Fe²⁺Fe³⁺DBQCl₂²⁻DBQCl₂³⁻ • xH₂O (PHZ = phenazine) with a reported conductivity of 4*10⁻⁵ S/cm,¹⁰ NBu₄Fe(DBQF₂)_{1.5} (0.1*10⁻³ S/cm),²⁶ and (NBu₄)₂Fe₂DBQ⁽³⁻⁾DBQ₂⁽²⁻⁾ with the highest reported conductivity of 0.16 S/cm.²⁷ Direct use of (H₃O)H₂O(PHZ)₃Fe²⁺Fe³⁺L²⁻L³⁻ • xH₂O as an electrode active was deemed unsuitable however due to this material's high instability, decomposition in all organic solvents tested (THF, DME, CH₃CN, PC) excepting acetone. Instead, a new material was prepared by substituting Li⁺ ions for the high molecular weight (H₃O)(PHZ)₃ paddle wheel cation. Synthesis of (NBu₄)₂Fe₂DBQ⁽³⁻⁾DBQ₂⁽²⁻⁾ is not straightforward and requires a complex synthesis wherein 2,5-diamino-1,4-benzoquinone undergoes in-situ hydrolysis to become the H₂DBQ ligand.²⁸ In addition, from the structural studies of these materials, the NBu₄⁺ ions completely block the pore volume making ion intercalation less feasible.

4-3. Results and discussion

The material presented for the first time in this paper, formulated as Li₂Fe²⁺_{1.2}Fe³⁺_{0.8}DBQ²⁻_{0.9}DBQ³⁻_{0.6} • 1.0H₂O or LiFeDBQ_{1.5} • 1.0H₂O if valence state is not considered, was prepared using a simple aqueous one-pot reaction by dissolving stoichiometric molar quantities of H₂DBQ, LiOH, and FeCl₂ in an ethanol, water mixture

at 60 °C to produce LiFeDBQ_{1.5} as a red microcrystalline precipitate with cubic microparticle morphology revealed by SEM (Figure 4-1a) that is insoluble in common electrolyte solvents used in battery application (PC, CH₃CN, THF, DME, DOL). Higher temperature reactions resulted in magnetic impurities in the Mossbauer spectrum. The crystallinity of this material was confirmed by PXRD. The empirical formula was confirmed by ICP-MS (Fe, Li), elemental analysis (C,H), EDX (O) and further corroborated by XPS and XAS analysis (Figures 4-1C and 4-1D). TGA analysis revealed that LiFeDBQ_{1.5} is thermally stable up to 260 °C (Figure 4-5). Mixed valence state of the Fe atoms was confirmed by integration of XPS spectra and further confirmed by Mossbauer spectroscopy to be c.a. Fe²⁺/Fe³⁺ 0.6/0.4. The charge transfer to the ligand was confirmed by EPR analysis of the formed radical (Figure 4-2C).

Structural characterization:

Powder X-ray diffraction (PXRD) was conducted to elucidate the three-dimensional structural information of LiFeDBQ_{1.5} (Figure 4-2D). The spectrum contained all diffractions corresponding to anilato coordination polymers of the type (NBu₄)₂[M(C₆O₄)₃]²⁸⁻²⁹ that crystalizes in the cubic space group I $\bar{4}3d$ as two interpenetrated (10,3)-a nets of opposing chirality. This structure contains a continuous network of octahedrally coordinated NBu₄[Fe((C₆O₄)_{1.5})] units. LiFeDBQ_{1.5} contains the same structural feature having trivalent FeO₆ octahedral centers with the same chirality in a continuous three-dimensional framework and small charge balancing Li⁺ ions replacing bulky [NBu₄]⁺. In contrast to the reference material that contained only Fe³⁺ centers, LiFeDBQ_{1.5} comprises mixed valence alternating Fe²⁺/Fe³⁺ centers (Figure 4-1D) and DBQ²⁻/DBQ³⁻ (Figure 4-2C). X-ray absorption spectroscopy (XAS) was conducted to

further elucidate the structure of LiFeDBQ_{1.5}. The X-ray absorption near-edge structure (XANES) studies for the Fe element (Figure 4-1C) revealed that LiFeDBQ_{1.5} had both Fe²⁺ and Fe³⁺ with rising edge energy (at half-edge height) at 7121.8 eV intermediate between reference compounds FeO (7119.19 eV) and Fe₂O₃ (7124.8 eV). The ratio of Fe²⁺/Fe³⁺ was quantified absolutely using Mossbauer spectroscopy (Figure 4-1E) to be 62.4% Fe²⁺. The local atomic structure information was extracted by fitting the extended X-ray absorption fine structure (EXAFS, Figure 4-1C) to represent non-phase shift corrected r-space EXAFS data in which the radial distance shorter than the bonding distance by ~0.5 Å along with the simulated best fit. The details of fitting procedure are described with the best fit parameters listed in Table 4-1. The first peak at apparent distance of 1.50 Å corresponds to the first shell O neighbors. Two Fe-O paths were used for the first shell corresponding to four O neighbors at 2.09 ± 0.01 Å and two O neighbors at 1.96 ± 0.01 Å (Table 4-1). The second peak at 2.17 Å contains scattering contributions from the second shell carbons whereas most the amplitude in third peak is contributed by multi-leg scattering paths Fe-O-C. The Fe-O bond distances determined by the EXAFS studies are comparable to those (2.04 Å) observed in the reported (NBu₄)FeDBQ_{1.5} MOFs.²⁹ The shorter Fe-O bond distances are assigned to the averaged bond

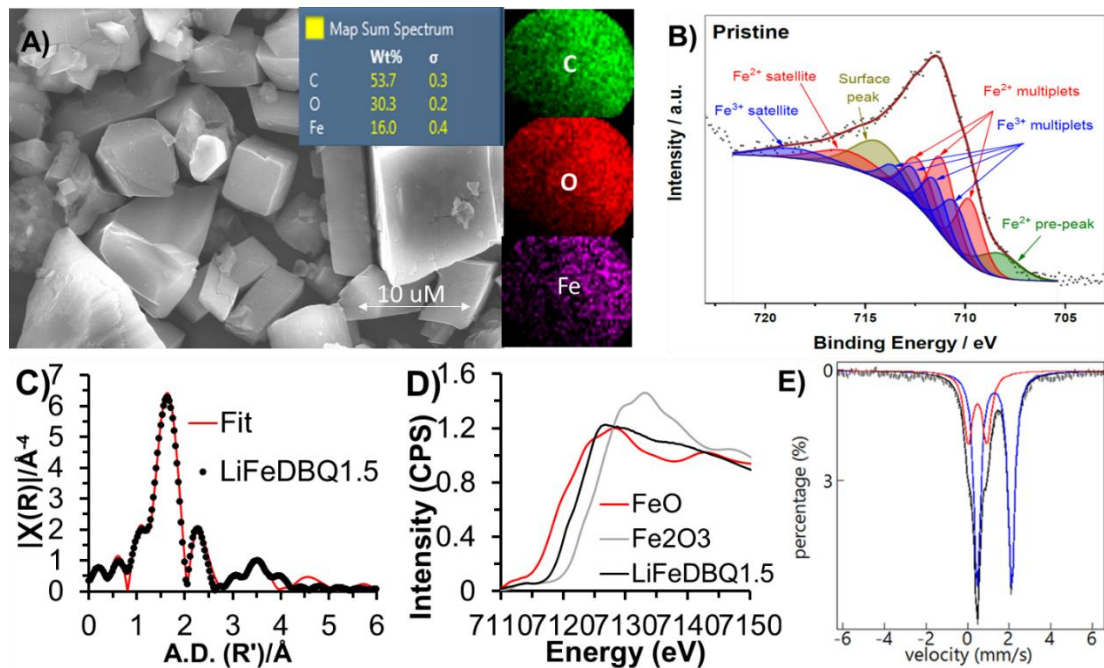


Figure 4-1. (A) High resolution SEM imaging of LiFeDBQ_{1.5} particle with 10 μM scale with inset showing EDX quantification of carbon, oxygen, and iron and EDX imaging shown to the right. (B) XPS integration of Fe. (C) X-ray absorption fine structure of LiFeDBQ_{1.5} and simulated best fit. (D) X-ray absorption near edge k-space spectra comparing rising energy of LiFeDBQ_{1.5} to reference materials FeO and Fe₂O₃. And (E) Mossbauer spectrum of pristine LiFeDBQ_{1.5} containing Fe²⁺ in blue and Fe³⁺ in red and sum spectra in black.

distances of (C-O)-Fe and (C=O)-Fe bonds without interaction with Li⁺. The longer bond distance was assigned to the averaged bond distances of two (C-O)-Fe bonds with interactions with Li⁺, which are expected to be more polarized owing to dual interactions of these O ligands with both Fe²⁺ and Li⁺ metal ions. All Fe atoms are bridged by the deprotonated H₂DBQ ligand (DBQ) with 7.81 Å (Figure 4-2A) to form a three-dimensional topology, which is like (NBu₄)FeDBQ_{1.5} MOF (Figure 4-1C). The square open channels along the b axis are unobstructed by bulky cations and are clearly visualized in the proposed three-dimensional topologies of LiFeDBQ_{1.5} (Figure 4-2A) and is believed to enable facile Li⁺ ion transportation during electrochemical charge/discharge processes.

The structure and bonding features of LiFeDBQ_{1.5} MOFs were further characterized using Fourier-transform infrared spectroscopy (FTIR) (Figure 4-2B). LiFeDBQ_{1.5} MOFs displayed two carbonyl stretching frequency at 1544 and 1498 cm⁻¹. The relative less intensive absorption at the higher wavenumber (1544 cm⁻¹) is assigned as one C=O group in the DBQ ligand which is only ligated with Fe while the relative more intensive absorption at the lower wavenumber (1506 cm⁻¹) is assigned to two C=O groups in the two DBQ ligands which not only bond with Fe but also interact with Li ion. H₂DBQ displays a carbonyl stretching frequency at approximately 1650 cm⁻¹. This absorption shifts to 1544 in the LiFeDBQ_{1.5} is consistent with strong coordination bonding from the carbonyls to the metal centers. A broadening of the carbonyl peak in the material is attributed to the presence of both bridging and terminal carbonyl moieties. A slight splitting of the carbonyl peak is attributed to the presence of both bridging transition metal and O-Li-O bonding interactions. H₂DBQ displays O-H torsion and O-H

bending frequencies at 688 cm^{-1} and 1229 cm^{-1} . Neither of these frequencies appear in any of the polymer spectra consistent with the formulation of coordination polymer materials.

These IR observations are consistent with the two different Fe-O bonds observed by EXAFS. These C=O stretching absorptions are weaker than those observed in H₂DBQ (1631 cm^{-1} ; Figure 4-2B). Similarly, LiFeDBQ_{1.5} MOFs exhibits a lower C-O stretching frequency at 1390 cm^{-1} than 1392 cm^{-1} for H₂DQB. These results indicate the strong metal (Lewis acid) and ligand (Lewis base) bonding interactions in LiFeDBQ_{1.5} MOFs when compared to the H₂DBQ precursor. In addition, H₂DBQ displays O-H torsion and O-H bending frequencies at 688 and 1229 cm^{-1} . Neither of these frequencies appears in

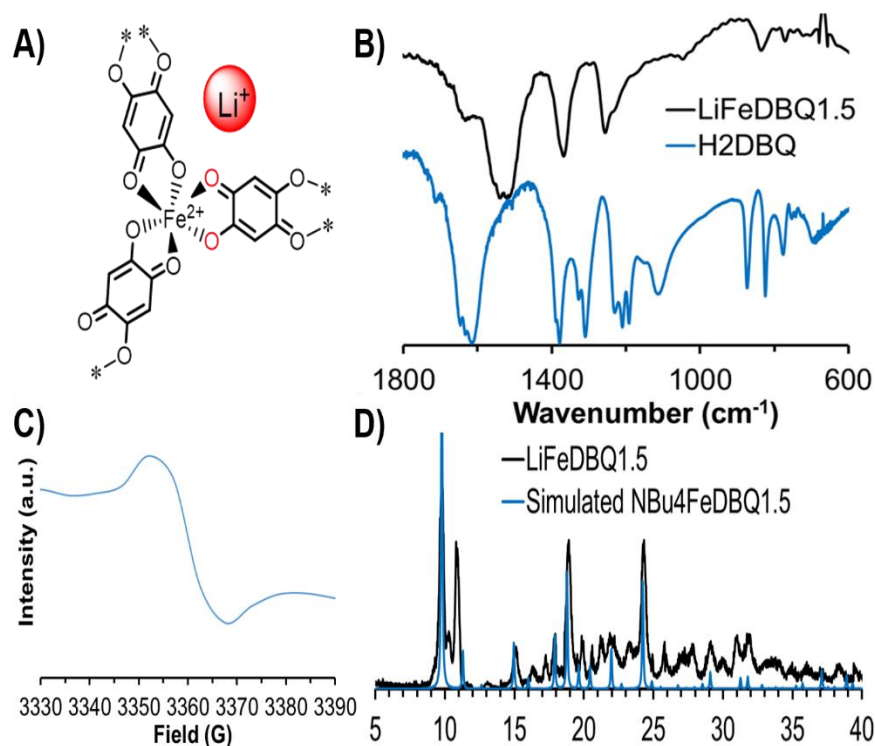


Figure 4-2. (A) Illustration of LiFeDBQ_{1.5} coordination sphere. (B) FTIR spectroscopy of LiFeDBQ_{1.5} and H₂DBQ. (C) Electron paramagnetic resonance spectra of LiFeDBQ_{1.5} in the appropriate range for the radical ligand. (D) PXRD matching of LiFeDBQ_{1.5} (Black) to the simulated Powder pattern of NBu₄FeDBQ_{1.5}.

the IR spectra of LiFeDBQ_{1.5} MOFs, indicating complete deprotonation of the hydroxyl moiety of the DBQ ligand.

Electrochemistry

In the cyclic voltammogram (Figure 4-3A), LiFeDBQ_{1.5} MOFs displayed reversible overlapped one-electron (3.12/2.86 V) and two-electron (2.32/2.28 V) redox couples corresponding to Fe³⁺/Fe²⁺ and DBQ²⁻/DBQ⁴⁻ respectively for an averaged potential of 2.45 V (all redox potentials reported are versus to Li in this study) at a scan rate of 0.1 mV/s. It is proposed that LiFeDBQ_{1.5} MOFs can undergo DBQ ligand-based reductions, with accompanying Li⁺ ion transfers. It is believed that Li ions are positioned around the Fe metal with weak bonding interactions with the DBQ ligands. Due to the stronger Lewis acid, Lewis base interactions and the noninnocent Fe²⁺/Fe³⁺ redox couple, LiFeDBQ_{1.5} MOFs has a more positive average potential at 2.46 V than that of the Li₂DBQ ligand precursor (2.05 V) by 400 mV. The more positive redox potential of LiFeDBQ_{1.5} MOFs is advantageous having a higher cell voltage than Li₂DBQ. In addition, LiFeDBQ_{1.5} MOFs exhibits more stable CV scans than Li₂DQB and H₂DBQ because of its superior insolubility. The CV of the H₂DBQ precursor could only be run for one cycle due to dissolution (Figure 4-6).

The battery performance of LiFeDBQ_{1.5} MOFs as cathode material was studied in coin cells using a Li metal disc as anode and 1.0 M LiTFSI in 1:1 V:V DME:DOL as supporting electrolyte. According to the CV study (Figure 4-3A), the LiFeDBQ_{1.5}/Li battery has a cell voltage of 2.46 V and allow for reversible intercalation of up to four Li ions for each Fe coordination unit. This corresponds to two electrons per DBQ⁽²⁻⁾/DBQ⁽⁴⁻⁾

and one electron for $\text{Fe}^{3+}/\text{Fe}^{2+}$ for a total possible theoretical specific capacity of 397.4 mAh/g for $\text{LiFeDBQ}_{1.5}$ (M.W. = 269.79 g/mol). However, in our Mossbauer spectroscopic studies, the Fe^{2+} percentage wavered between 12% and 82% in the reduced and oxidized states respectively indicating the ferric/ferrous redox couple is responsible for 0.6 electrons per formula unit and the charge storage mechanism is primarily ligand based ($C_{\text{th}} = 298.02$ mAh/g). As such and considering the realized capacity of this material (259 mAh/g at 30 mA/g current density), the C-rate was set as 1C equal to 300 mAh/g to making testing conditions more transferrable to comparative studies (i.e. 1c = 1h charging time).

The battery was cycled between 1.5 and 3.9 Volts. Benefitted from the high porosity and conductivity of $\text{LiFeDBQ}_{1.5}$ MOFs, the battery exhibited excellent rate performance from 0.1 to 10.0 C. The battery containing $\text{LiFeDBQ}_{1.5}$ cathode could achieve 259 mAh/g specific capacity at 0.1 C charge and discharge rate. This is equivalent to 606.2 Wh/kg for the M-DBQ/Li full cell battery which is more than (twice

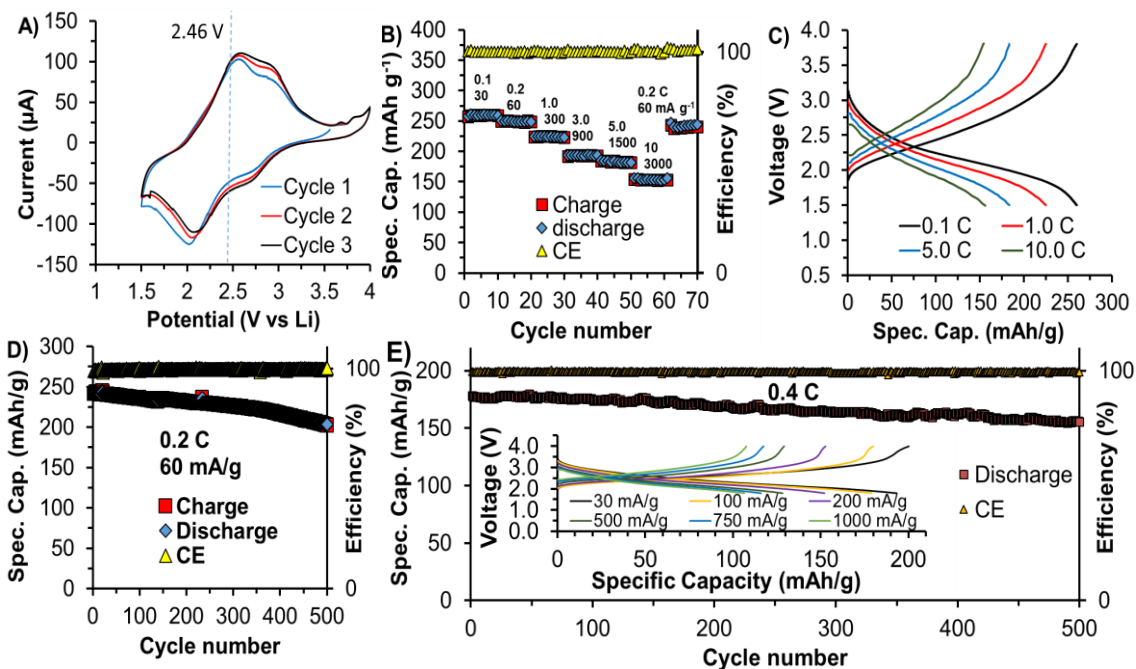


Figure 4-3. (A) CV of LiFeDBQ_{1.5}/Li from a three-electrode setup, (B) to (D) Battery data of the LiFeDBQ_{1.5}/Li battery. (B) Rate performance (C) Representative charge/discharge curves at various C rates. (D) Long term cycling for LiFeDBQ_{1.5} in the 1.5 to 3.9 V window. (E) Long term cycling for LiFeDBQ_{1.5} in the 1.8 to 4.0 V window with inset showing charge/discharge profile at different current densities.

the energy density of the state-of-the-art Li-ion battery (150-300 Wh/kg). Also, the charging/discharging rate capability of the LiFeDBQ_{1.5}/Li was much improved and is currently the fastest and highest energy material of all reported MOFs cathode materials. This cell demonstrated 259 mAh/g, 249 mAh/g, 225 mAh/g, 194 mAh/g, 185 mAh/g, and 153 mAh/g at 0.1 C (30 mA/g), 0.2 C (60 mA/g), 1.0 C (300 mA/g), 3.0 C (900 mA/g), 5.0 C (1500 mA/g), and 10.0 C (3,000 mA/g) current density respectively achieving 86.9.8%, 83.6%, 75.0%, 66.4%, 62.1%, and 51.3% of its theoretical capacity of 298.1 mAh/g (figure 4-2B). At the highest current density tested (10.0 C 3,000 mA/g) the cell could charge/discharge in approximately 3.24 minutes still achieving greater than 50% capacity utilization which is more than 10 times faster than the commercialized Li-ion battery. Representative charge discharge curves are shown (figure 4-3C). Also, the cell

could achieve 241.1 mAh/g at 0.2 C and still maintain greater than 84% capacity retention (203.6 mAh/g) of the first cycle after 500 cycles which also meets the industry standard of greater than 80% capacity retention after 500 cycles.³⁰ These studies indicate that batteries utilizing LiFeDBQ_{1.5} active material have relatively high cycling stability compared to other reported MOF electrode materials.³¹

Since the Fe/C ratio of the electrode was found to diminish with long term cycling (disassembled cell after 500 cycles (Figure 4-10), a battery was also cycled between 4.0 and 1.8 V cutoff voltages to discourage over reduction of the material that may result from exchange reactions of Li⁺ for Fe²⁺. Long term cycling was performed at 0.4C where 178.11 mAh/g was observed at the first cycle. After 500 cycles the capacity retention was 86.90% (154.78 mAh/g) of the first cycle with a capacity retention of 99.978% per cycle (Figure 4-3E). These studies indicate that the possible exchange reaction was partly responsible for capacity decay considering the capacity retention was improved by 2.9% over 500 cycles. In addition a solid electrolyte was utilized to prevent material crossover (figure 4-7). The active material mass loading of these discs was very high at c.a. 24mg/cm² and still demonstrated good performance. At 0.1C rate. The cell demonstrated a discharge capacity of 201.2 mAh g⁻¹ in the first cycle and a discharge capacity of 202.2 mAh g⁻¹ in cycle 50 showing no capacity decay. The coulombic efficiency did begin to destabilize near cycle 40 possibly due to excess oxidation of the solid electrolyte.

To further understand the charge/discharge mechanism of the LiFeDBQ_{1.5} MOFs cathode, the charged and discharged states were studied by FTIR, XPS, XANES, and

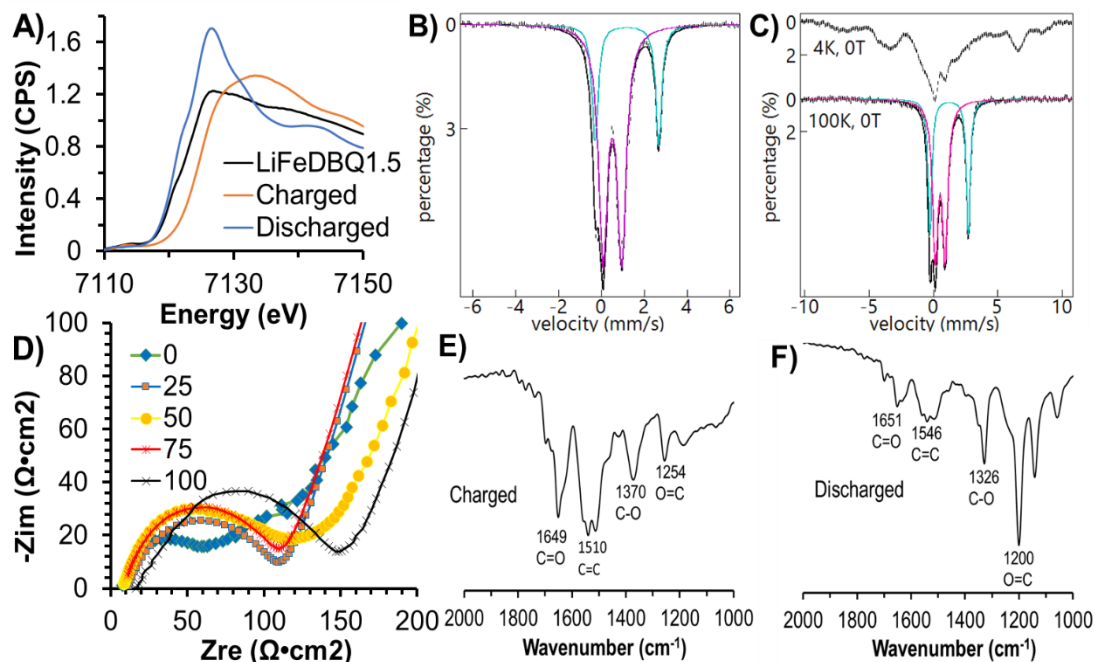


Figure 4-4. (A) XANES rising energy at pristine, charged, and discharged states. (B) Mossbauer of charged state sample and (C) discharged state sample. (D) EIS Nyquist plot at different states of charge. (E-F) FT-IR spectra of Charged and Discharged state samples.

Mossbauer spectroscopies (Figure 4-4). In FTIR studies (Figure 4-4E and 4-4F), compared to the charged state, the C=O stretches (1651 cm^{-1}) was greatly diminished in

the discharged state of the LiFeDBQ_{1.5} MOFs cathode, accompanied with radical spectroscopic changes observed for other vibrational modes of C=C and C-O bonds. It should be noted that the charged state of the LiFeDBQ_{1.5} MOFs cathode exhibited different spectroscopic features than pristine LiFeDBQ_{1.5} MOFs, which is attributed to the radical state of the ligands confirmed by EPR at (3359 G, Figure 4-2C) in the LiFeDBQ_{1.5} MOFs cathode. The FTIR results confirmed the complete formation of quinolate groups in the DBQ ligand in the discharged state. In the XRD studies, the XRD spectra collected after several cycles indicated a complete loss of crystallinity making further charge state dependent structural studies impossible. The XANES spectrum of

the pristine state described previously had half height energy intermediate to the reference compound, but in the charged (oxidized) and discharged (reduced) states the energies approached reference compounds Fe_2O_3 and FeO respectively due to varying the ratio of $\text{Fe}^{2+}/\text{Fe}^{3+}$ in the active material. Further analysis by XPS indicated the $\text{Fe}^{2+}/\text{Fe}^{3+}$ redox couple was partially reversible (Figure 4-9). The pristine material contained 60 percent Fe^{2+} which was validated by Mossbauer analysis (Figure 4-7). When oxidized electrochemically within a coin cell, Fe^{2+} dropped to 12.5 percent. When reduced electrochemically in a coin cell the Fe^{2+} ratio rose back to 64.5 percent which higher than the pristine state. Mossbauer spectroscopy confirmed these results by indication of $\text{Fe}^{2+}/\text{Fe}^{3+}$ ratios of (62.4/36.2), (27.7/77.2), and (63.0/44.1) in the pristine, charged, and discharged states respectively.

The redox reversibility seen from cyclic voltammetry (figure 4-3A supports these findings. $\text{LiFeDBQ}_{1.5}$ was scanned from 4.0 to 1.8V then back to 4.0V for three cycles. Two reversible single electron processes were observed with reversible events at 2.90V/3.00V and 2.30V/2.40V. using the Randles-Sevcik equation the Li-ion diffusion coefficient for the oxidation at 2.40V was calculated to be $1.64 \times 10^{-7} \text{ cm}^2 \text{ s}^{-1}$, the oxidation at 3.0V was $1.18 \times 10^{-7} \text{ cm}^2 \text{ s}^{-1}$. The reduction at 2.9V was calculated to be $1.60 \times 10^{-8} \text{ cm}^2 \text{ s}^{-1}$. The reduction at 2.30V was calculated to be $2.16 \times 10^{-7} \text{ cm}^2 \text{ s}^{-1}$. All Li ion diffusion coefficients show very high kinetics of Li ions in the electrode. In addition, the $\text{Fe}^{2+}/\text{Fe}^{3+}$ redox couple overlapping the quinone redox potential is beneficial to increasing the theoretical specific capacity and voltage of this material. Also, the spontaneous oxidation of Fe^{2+} to Fe^{3+} by ligand, can help to explain the capacity utilization and charging/discharging rate performance. We propose that during the reduction step, when

Fe^{3+} is promoted to Fe^{2+} , favorable metal to ligand charge transfer can occur assisting in near complete reduction of the ligand. During the oxidation step, the ligand is first oxidized encouraging spontaneous metal to ligand charge transfer again followed by overlapping oxidation peaks of the metal and ligand. From the CV, it can be seen in the first cycle redox is predominantly ligand based. But in the second and third cycles the peak intensity for the higher voltage process containing the $\text{Fe}^{2+}/\text{Fe}^{3+}$ couple becomes more pronounced after the ratio of Fe^{3+} is increased from 40 percent in the pristine material to 82.5% by electrochemical oxidation in the coin cell. These results help to demonstrate the importance of rationally designing MOFs containing synergistic metals and ligands for the desired application.

Electronic conductivity was measured by a two-point dc setup on 10mm by 2 mm pellets. The pellets were prepared by compressing 400mg $\text{LiFeDBQ}_{1.5}$ (vacuum dried 150 °C) at a pressure of 8 metric tons. Ag paste was applied at two points along the height of the pellet across the diameter to improve contact between the electrodes and surface. At room temperature a resistance of 94.0 +- 0.1 Ohms/cm was recorded. By taking the inverse of resistance, the conductivity was calculated as $1.1 * 10^{-2}$ S/cm. This conductivity value is intermediate to what Long and coworkers reported for the very similar $\text{NBu}_4\text{Fe}(\text{DBQ})_{1.5}$ (0.16 S/cm) and the fluoranilic acid derivative $\text{NBu}_4\text{Fe}(\text{fan})_{1.5}$ ($1.77 * 10^{-3}$ S/cm) and is three orders of magnitude more conductive than the phenazine templated $(\text{PHZ})\text{Fe}(\text{DBQCl}_2)_{1.5}$ ($4.0 * 10^{-5}$ s/cm) placing $\text{LiFeDBQ}_{1.5}$ among the highest observed values for conducting MOFs. The lower conductivity value of $\text{LiFeDBQ}_{1.5}$ to $\text{NBu}_4\text{FeDBQ}_{1.5}$ may be explained by a higher concentration of $\text{DBQ}^{(3-)}$ than $\text{DBQ}^{(2-)}$ which can hinder charge hopping between ligands. Our ICP-MS and elemental analysis

of this material indicated 21.4 percent excess Li^+ ions to the proposed structure which may exist as charge balancing ions to the $\text{DBQ}^{(3-)}$ radical. It is also possible the combination of mixed valence ligands and mixed valence metals has a deleterious effect to electrical conductivity by cancelling each other out to some degree in the bulk material possibly explaining why $(\text{PHZ})\text{Fe}(\text{DBQCl}_2)_{1.5}$ has lower conductivity. Further detailed investigation into this phenomenon is currently under way. The conductivity of $\text{LiFeDBQ}_{1.5}$ was also probed by electrochemical impedance spectroscopy (EIS) (Figure 4-4D). After several cycles for activation the battery cell was tested at differing states of charge. The charge transfer resistance in the fully charged (3.9 V) and fully discharged (1.5 V) states was c.a. $150 \Omega/\text{cm}^{-2}$ and c.a. $100 \Omega/\text{cm}^{-2}$ respectively. All other states of charge had resistance values intermediate to these two values, decreasing as full discharge was approached. The lower resistance in the reduced state can be explained by XPS analysis indicating mixed valence $\text{Fe}^{2+}/\text{Fe}^{3+}$ in a 64:36 molar ratio giving a higher electrical conductivity than the charged state that is predominantly (88%) Fe^{3+} disallowing charge hopping. At all states of charge the resistance was less than $150 \Omega/\text{cm}^{-2}$ which is competitive to organic and inorganic electrodes alike.

4-4. Conclusion

In summary, redox active $\text{LiFeDBQ}_{1.5}$ was fully characterized and applied as a Li^+ ion storage cathode material. The high rate performance and good cycling stability of $\text{LiFeDBQ}_{1.5}$ MOFs are benefited from its high conductivity due do mixed Iron valence, porous Li^+ ion transport channels, increased voltage due to reversible redox changes of the $\text{Fe}^{3+}/\text{Fe}^{2+}$ and non-innocent DBQ quinone ligand, and strong dative chemical interactions between the Fe metal and the ligand resulting in insolubility. The synthesis

for this material is straightforward requiring only common solvents and commercially available reagents. In addition, LiFeDBQ_{1.5} is stable in the voltage window 1.5-4.0 V making it suitable for a host of high energy applications. Having rich structural tunability allowing different metals and functionalized redox active ligands, the redox voltage and theoretical capacity can be modulated for this class for DBQ coordination polymers. Particularly, it is highly promising to develop redox active MOF electrode materials for reversible integration of multivalent ions such as Mg²⁺, Ca²⁺ and Al³⁺, which represents an ongoing challenge in the field of rechargeable batteries.

4-5. Experimental

Chemicals and manipulations. All chemicals were purchased from TCI or Sigma-Aldrich, stored in an Argon glovebox, and used directly. All experimental operations were conducted under a N₂ atmosphere. Elemental analysis was done at Atlantic Microlab. ICP-MS was done on Thermo X Series 2 Quadrupole ICP-MS. SEM was done on a FEI Quanta FEG 650. XPS spectra was acquired on a Kratos Axis Ultra DLD equipped with a hemispherical analyzer⁶ Monochromatic aluminum K α was used as the X-ray source and an area of 300 nm x 700 nm was scanned. All acquisitions were collected at ultrahigh vacuum of 2 x 10⁻⁹ Torr or less. The spectra were analyzed using CasaXPS software and was standardized by calibrating the C(1s) peak to 284.8 eV. Thermogravimetric analysis was performed on a TA Instruments TGA 2950 Thermogravimetric Analyzer at a heating rate of 10 °C/min and a Nitrogen flow rate of 150 mL/min. FT-IR was measured on a Perkin Elmer Spectrum 100 FT-IR spectrometer with universal ATR sampling accessory. XRD was collected using a Panalytical X'Pert Pro X-ray Diffraction Spectrometer with monochromatic Cu K-alpha radiation using the

High Score software program to index peaks and identify minerals. XAS data were measured at beamline 20-BM-B of Advanced Photon Source at Argonne National Laboratory. EIS was recorded using a Gamry potentiostat. Mössbauer spectra were recorded with two spectrometers using Janis Research (Wilmington, MA) SuperVaritemp dewars that allow studies in applied magnetic fields up to 7.5 T in the temperature range from 1.5 to 200 K. Mössbauer spectral simulations were performed using the WMOSS software package (SEE Co, Edina, MN). Perpendicular (9.63 GHz) mode X-band EPR spectra were recorded on a Bruker E500A spectrometer equipped with an Oxford ESR 910 liquid helium cryostat and an Oxford temperature controller.

Preparation of LiFeDBQ_{1.5} MOFs and Li₂DBQ cathode. Active material (60% by weight), Carbon Black(30% by weight), and PTFE (10% by weight) were ground into a slurry with mortar and pestle by adding drops of EtOH. The slurry was cast onto aluminum foil by pestle and doctor blading and dried at room temperature under reduced pressure. 12.25 mm discs were punched out of the sheet and dried for an additional 12 hours in the 100 °C vacuum oven. The mass loading of the cathodes was 2.0 to 2.2 mg/cm².

Cyclic Voltammetry Studies of LiFeDBQ_{1.5}, Li₂DBQ, and H₂DBQ. A three electrode solid CV technique was employed whereby Li foil was the counter and reference electrodes and a prepared 10mm cathode disc was the working electrode. The electrodes were lowered into a 20 ml scintillation vial containing 5.0 ml 1.0 M LiTFSI electrolyte in 1:1 V:V DME:DOL solvent mixture. Voltammetry was started at the high voltage cutoff, scanned towards the negative region at a sweep rate of 0.1 mV/s to the low cutoff voltage then scanned back to the high voltage at the same rate to complete one cycle. All cyclic

voltammetry experiments were conducted in an Ar filled glovebox due to the reactivity of Li metal and N_2 . O_2 and H_2O levels were kept below 0.1 PPM.

EIS studies. Performed using a Gamry potentiostat by placing a coin cell containing the described active material inside a conductive clamp with cathode side attached to working electrode lead and with the anode side attached to counter/reference leads. Scanned from 10^5 Hz to 10^{-1} Hz with 10 points/decade. All EIS studies were performed on coin cells that had been cycled by charging and discharging for 5 cycles at 0.1 C charge rate.

Battery studies of LiFeDBQ_{1.5}, Li₂DBQ, and H₂DBQ. Battery testing was conducted using the Lanhe battery testing system with stainless steel cr2032 type coin cells containing Li metal anode, Celgard 2025 separator and 1.0 M LiTFSI in 1:1 V:V DME:DOL electrolyte. Open circuit Voltage was recorded as 3.54 V so the batteries were first discharged to 1.50 V then charged to 3.90 V unless otherwise specified with ten minutes resting time between cycles. The batteries were charged and discharged galvanostatically at different C rates calculated by multiplying the mass of active material in the electrode by the theoretical specific capacity of the cathode active material and then multiplying this value by the desired C rate. A piece of Li metal disc was used as an anode in all coin cells to assure the cathode was the capacity limiting electrode.

Solid electrolyte cell. Electrodes containing LiFeDBQ_{1.5}:Carbon Black:Solid electrolyte in a ratio of 80:10:10 were added into a coin cell with 1.0 mm thick solid electrolyte disc. The solid electrolyte contained: Polyethylene glycol(mw: 4000): Polyethylene oxide (mw: 6,000): TiO_2 50 nm particles: LiTFSI in a mass ratio of 70:10:10:10 by weight. The

TiO₂ nanoparticles were suspended in a 1:1 mixture in excess CH₃CN:EtOH by repeated sonication and stirring. This suspension was added slowly to separate suspension containing the other components in excess CH₃CN:EtOH with stirring and sonication at least five times before all were combined to ensure uniform distribution. Additional sonication and stirring were performed at the end. 90 percent of the solvent was then removed by rotary evaporation at 40 °C with rapid rotation (200 rotations/minute). The Remaining suspension had a look and consistency of Elmers white glue. This mixture was pipetted into a petri dish and dried rapidly under vacuum at 60 °C. A white, flexible, 2mm film was obtained after cooling. 10 mm circles were cut from this film and pressed onto the cathode discs that were used for battery testing. The cathode discs were prepared by grinding a 80:10:10 by weight ratio of LiFeDBQ_{1.5}:Carbon Black:Solid electrolyte with mortar and pestle following by compressing into 30 mg pellets at 1000 N at room temperature.

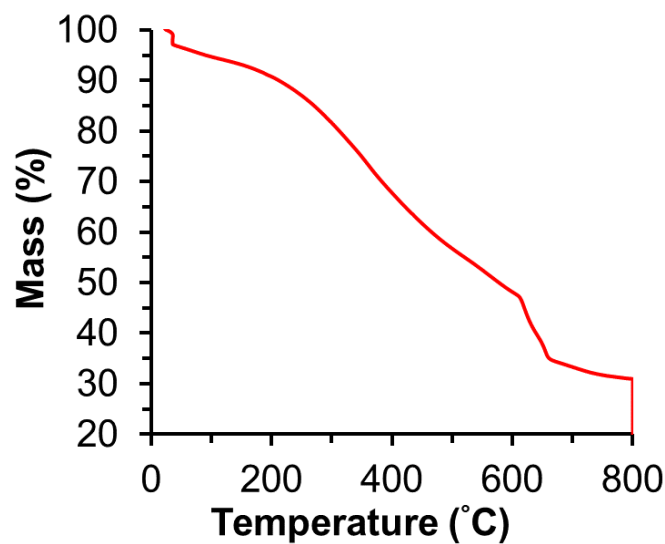
Synthesis of LiFeDBQ_{1.5}

A 100 mL Schlenk flask was degassed with N₂ and maintained under N₂. At 60 °C, LiOH (0.036 g, 1.5 mmol) and H₂DBQ (0.228 g, 1.5 mmol) were dissolved in 10 mL H₂O. FeCl₂ • 4H₂O (0.221 g, 1.0 mmol) dissolved in 25 ml EtOH was added slowly over two hours via addition funnel. The reaction mixture was stirred for an additional 1 hour and then stirring was turned off. The flask was left in the 60 °C bath until the solvent became completely transparent indicating reaction completion, then cooled to room temperature and filtered under air-free conditions. The precipitate was purified by rinsing

Table 4-1: EXAFS and XANES for LiFeDBQ_{1.5}

Sample	Path	R (Å)	N	σ^2 (10^{-3}Å^2)	R-factor (%)	ΔE_0 (eV)
Li ₂ Fe ₂ (DBQ) ₃	Fe-O	1.96±0.03	2	3.45±1.35	0.91	2.91±0.76
	Fe-O	2.09±0.01	4	9.48±0.74		
	Fe-C	2.87±0.01	6	15.0±4.01		
	Fe-C	4.24±0.01	6	15.0±4.01		

with a degassed 3:1 EtOH:H₂O mixture until solvent ran clear. A purple, hygroscopic, air-sensitive powder was collected and dried in a vacuum-oven at 120 °C overnight and then stored in an Argon filled glovebox with less than 0.1 ppm O₂ and H₂O atmosphere. The yield was ca. 86.6% by mass. (0.232 g). Anal. Calcd. for LiFeDBQ_{1.5}·1.0 H₂O: C 37.5, H 1.74, N 0.00; found C 37.8, H 1.74, N 0.00. FTIR (KBr pellets): $\nu = 3450, 3393, 3074, 1534, 1346, 1252, 831 \text{cm}^{-1}$. ICP-MS calculated for LiFeDBQ_{1.5}·H₂O: Li 2.41%, Fe 19.4%; found: Li 2.80%, Fe 18.8%.

**Figure 4-5.** Thermogravimetric analysis of LiFeDBQ_{1.5}

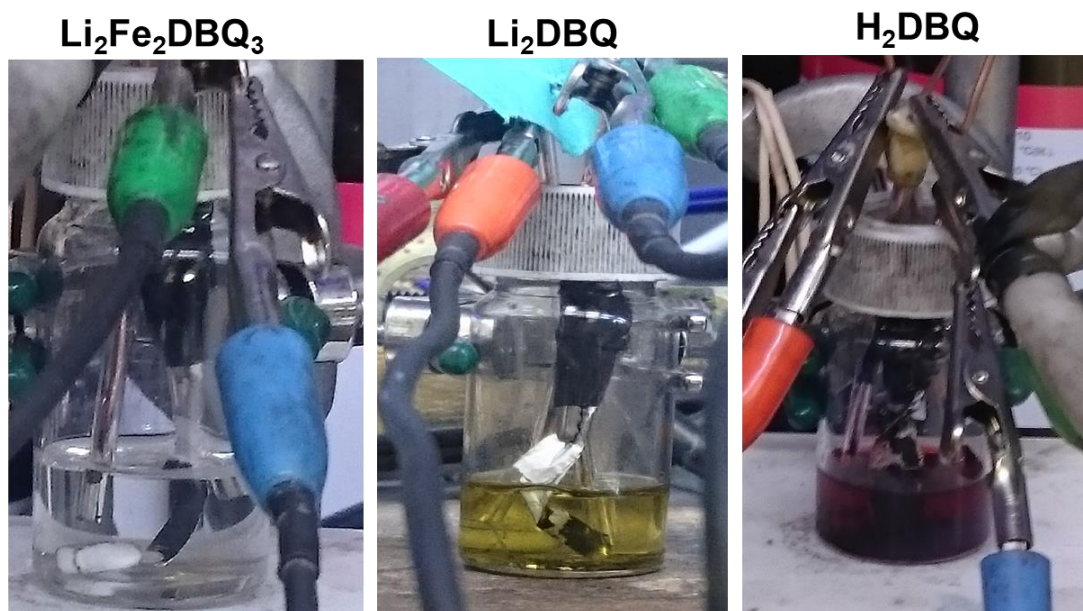
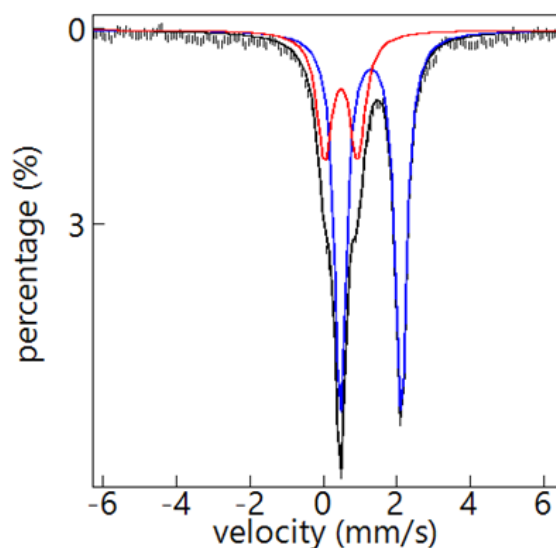
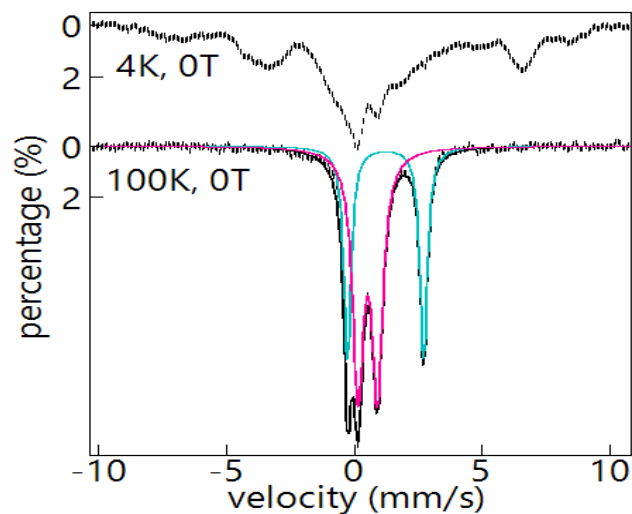


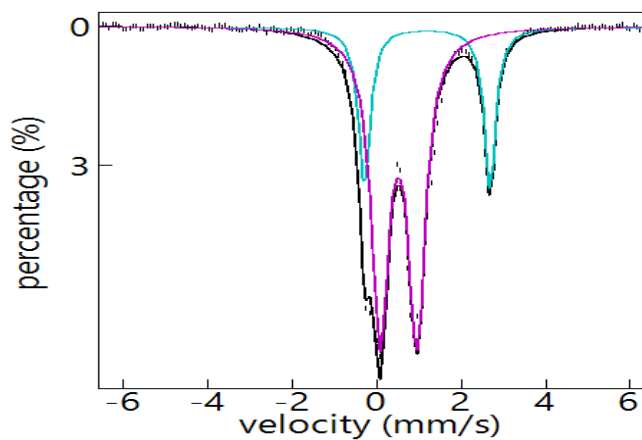
Figure 4-6. Solid cyclic voltammetry set-up after 3 complete cycles from 4.0 to 1.5V for $\text{LiFeDBQ}_{1.5}$ at 0.1mV/s rate showing no dissolution of the active material in pristine, charged, or discharged state. For Li_2DBQ the solvent became yellow during the charging process. For H_2DBQ the solvent immediately became red in the pristine state. The electrolyte was 1.0 M LiTFSI in 1:1 DME:DOL for each experiment.



		color	$\delta(\text{mm/s})$	$\Delta E_{\text{q}}(\text{mm/s})$	linewidth(mm/s)	percentage	Fe valence
site 1		blue	1.29	1.65	0.39	62.4%	II
site 2		red	0.48	0.893	0.50	37.2%	III



	color	δ (mm/s)	ΔE_q (mm/s)	linewidth(mm/s)	percentage	Fe Valence
site 1	cyan	1.22	2.99	0.388	63.0%	II
site 2	magenta	0.52	0.76	0.51	34.1%	III



	color	δ (mm/s)	ΔE_q (mm/s)	linewidth(mm/s)	percentage	Fe valence
site 1	cyan	1.19	2.97	0.33	27.7%	II
site 2	magenta	0.51	0.87	0.50	77.2%	III

Figure 4-7. Mössbauer spectroscopy of LiFeDBQ_{1.5} run at 10K. And tabulated result. Pristine, discharged and charged states respectively top to bottom.

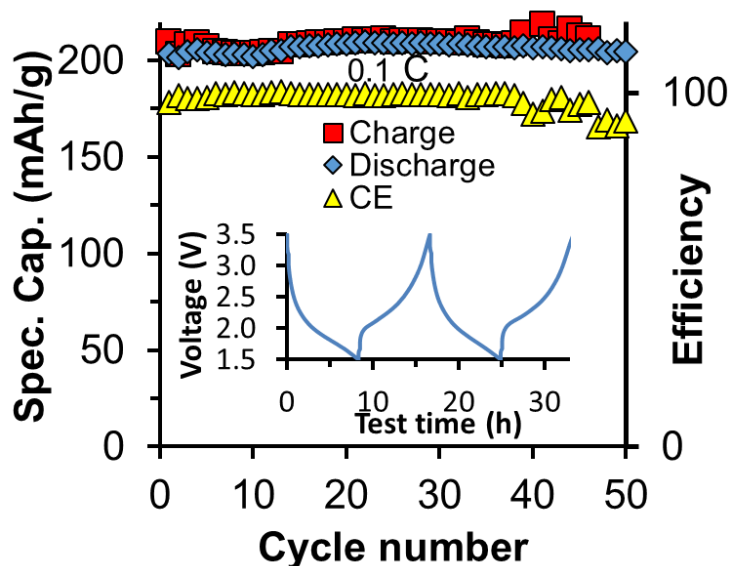


Figure 4-8. Solid electrolyte cell cycling performance and charging/discharging voltage versus time curve.

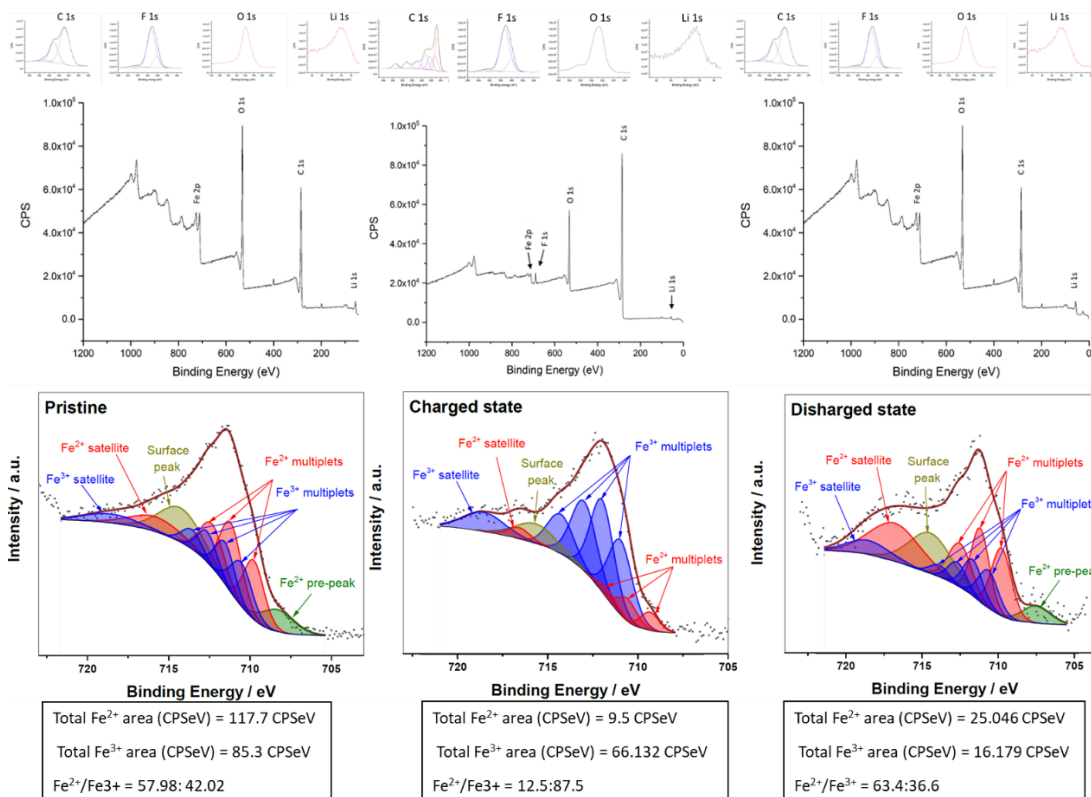


Figure 4-9. XPS integration of Fe²⁺/Fe³⁺ in different states of charge. Including XPS survey of different states of charge.

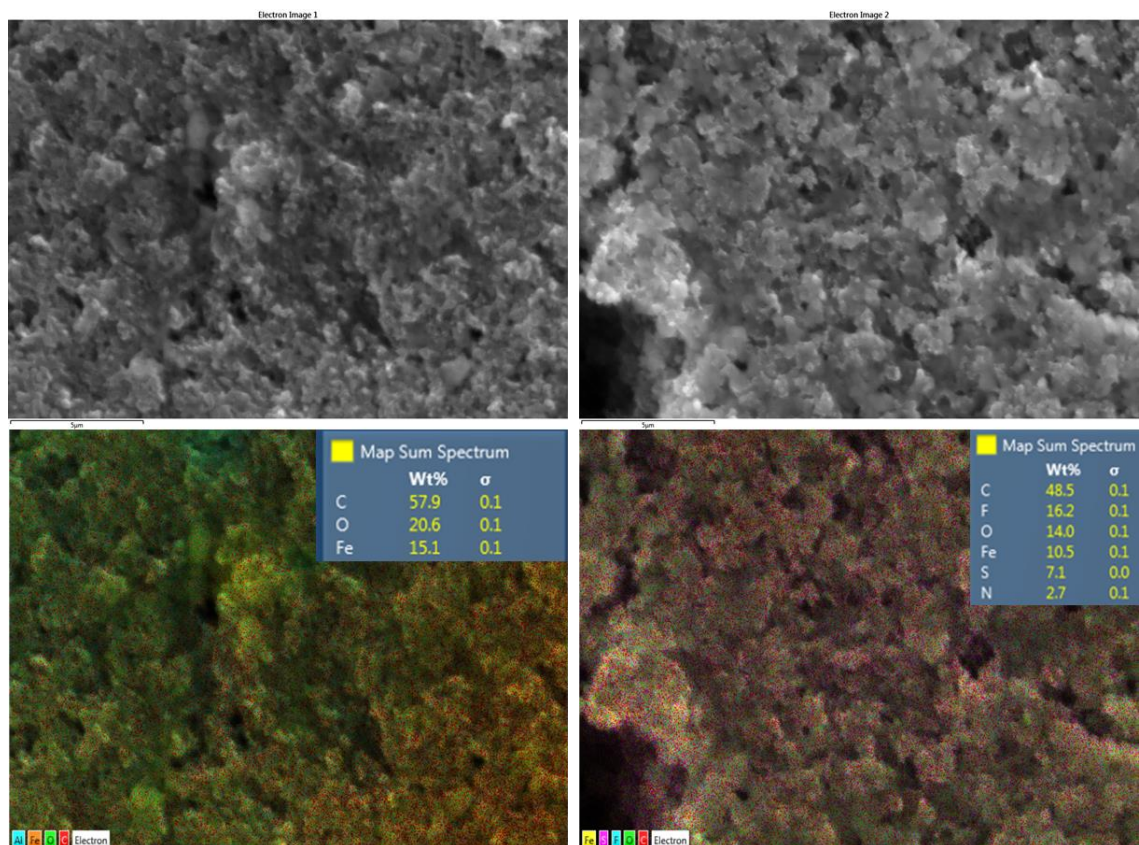


Figure 4-10. SEM-EDS analysis of freshly prepared electrode (left) and SEM-EDS analysis after 500 cycles indicating presence of SEI layer formation by decomposition of TFSI anion. Also, the Fe/C ratio was lowered by 5% after long term cycling.

4-6. References

1. Chen, H.; Armand, M.; Courty, M.; Jiang, M.; Grey, C. P.; Dolhem, F.; Tarascon, J.-M.; Poizot, P., Lithium Salt of Tetrahydroxybenzoquinone: Toward the Development of a Sustainable Li-Ion Battery. *J. Am. Chem. Soc.* **2009**, *131*, 8984-8988.
2. Han, C.; Li, H.; Shi, R.; Zhang, T.; Tong, J.; Li, J.; Li, B., Organic quinones towards advanced electrochemical energy storage: recent advances and challenges. *J. Mater. Chem. A* **2019**, *7*, 23378-23415.
3. Hanyu, Y.; Ganbe, Y.; Honma, I., Application of quinonic cathode compounds for quasi-solid lithium batteries. *J. Power Sources* **2013**, *221*, 186-190.
4. Song, Z.; Qian, Y.; Gordin, M. L.; Tang, D.; Xu, T.; Otani, M.; Zhan, H.; Zhou, H.; Wang, D., Polyanthraquinone as a Reliable Organic Electrode for Stable and Fast Lithium Storage. *Angew. Chem. Int. Ed.* **2015**, *54*, 13947-13951.
5. Wroblewski, J. T.; Brown, D. B., Synthesis, magnetic susceptibility, and Moessbauer spectra of iron(III) dimers and iron(II) polymers containing 2,5-dihydroxy-1,4-benzoquinones. *Inorg. Chem.* **1979**, *18*, 498-504.
6. Xiang, J.; Chang, C.; Li, M.; Wu, S.; Yuan, L.; Sun, J., A Novel Coordination Polymer as Positive Electrode Material for Lithium Ion Battery. *Crystal Growth & Design* **2008**, *8*, 280-282.
7. Wang, S.; Wang, L.; Zhu, Z.; Hu, Z.; Zhao, Q.; Chen, J., All Organic Sodium-Ion Batteries with Na₄C₈H₂O₆. *Angew. Chem. Int. Ed.* **2014**, *53*, 5892-5896.

8. Zhu, Z.; Li, H.; Liang, J.; Tao, Z.; Chen, J., The disodium salt of 2,5-dihydroxy-1,4-benzoquinone as anode material for rechargeable sodium ion batteries. *Chem. Commun.* **2015**, *51*, 1446-1448.
9. Mercuri, M., Laura; Congiu, F.; Concas, G.; Sahadevan, A., Recent Advances on Anilato-Based Molecular Materials with Magnetic and/or Conducting Properties. *Magnetochemistry* **2017**, *3*, 17.
10. Shilov, G. V.; Nikitina, Z. K.; Ovanesyan, N. S.; Aldoshin, S. M.; Makhaev, V. D., Phenazineoxonium chloranilatomanganate and chloranilatoferrate: synthesis, structure, magnetic properties, and Mossbauer spectra. *Russ. Chem. Bull.* **2011**, *60*, 1209-1219.
11. Ziebel, M. E.; Darago, L. E.; Long, J. R., Control of Electronic Structure and Conductivity in Two-Dimensional Metal–Semiquinoid Frameworks of Titanium, Vanadium, and Chromium. *J. Am. Chem. Soc.* **2018**, *140*, 3040-3051.
12. Ward, M. D.; McCleverty, J. A., Non-innocent behaviour in mononuclear and polynuclear complexes: consequences for redox and electronic spectroscopic properties. *J. Chem. Soc.-Dalton Trans.* **2002**, 275-288.
13. Shota, M.; Tepei, Y.; Hiroshi, K., Crystal Structure and Proton Conductivity of a One-dimensional Coordination Polymer, {Mn(DHBQ)(H₂O)₂}. *Chem. Lett.* **2009**, *38*, 654-655.
14. Shilov, G. V.; Nikitina, Z. K.; Ovanesyan, N. S.; Aldoshin, S. M.; Makhaev, V. D., Phenazineoxonium chloranilatomanganate and chloranilatoferrate: synthesis, structure, magnetic properties, and Mössbauer spectra. *Russ. Chem. Bull.* **2011**, *60*, 1209-1219.
15. Nikitina, Z. K.; Shilov, G. V.; Ovanesyan, N. S.; Makhaev, V. D., Synthesis and some properties of anionic chloranilate complexes of iron(III). Crystal and molecular

structure of rubidium and cesium chloranilateferrates. *Russ. Chem. Bull.* **2013**, *62*, 419-426.

16. Kingsbury, C. J.; Abrahams, B. F.; D'Alessandro, D. M.; Hudson, T. A.; Murase, R.; Robson, R.; White, K. F., Role of NEt_4^+ in Orienting and Locking Together $[\text{M}_2\text{lig}_3]^{2-}$ (6,3) Sheets (H_2lig = Chloranilic or Fluoranilic Acid) to Generate Spacious Channels Perpendicular to the Sheets. *Crystal Growth & Design* **2017**, *17*, 1465-1470.

17. Imaz, I.; Mouchaham, G.; Roques, N.; Brandès, S.; Sutter, J.-P., Tetradihydrobenzoquinonate and Tetrachloranilate Zr(IV) Complexes: Single-Crystal-to-Single-Crystal Phase Transition and Open-Framework Behavior for $\text{K}_4\text{Zr}(\text{DBQ})_4$. *Inorg. Chem.* **2013**, *52*, 11237-11243.

18. Benmansour, S.; Valles-Garcia, C.; Gomez-Claramunt, P.; Espallargas, G. M.; Gomez-Garcia, C. J., 2D and 3D Anilato-Based Heterometallic M(I)M(III) Lattices: The Missing Link. *Inorg. Chem.* **2015**, *54*, 5410-5418.

19. Benmansour, S.; Gomez-Claramunt, P.; Valles-Garcia, C.; Espallargas, G. M.; Garcia, C. J. G., Key Role of the Cation in the Crystallization of Chiral Tris(Anilato)Metalate Magnetic Anions. *Crystal Growth & Design* **2016**, *16*, 518-526.

20. Benmansour, S.; Abherve, A.; Gomez, P.; Valles-Garcia, C.; Gomez-Garcia, C. J., Nano-sheets of 2D magnetic and conducting Fe(II)/Fe(III) mixed-valence MOFs. *ACS Appl. Mater. Interfaces* **2006**, 1-10.

21. Feng, D.; Lei, T.; Lukatskaya, M. R.; Park, J.; Huang, Z.; Lee, M.; Shaw, L.; Chen, S.; Yakovenko, A. A.; Kulkarni, A.; Xiao, J.; Fredrickson, K.; Tok, J. B.; Zou, X.; Cui, Y.; Bao, Z., Robust and conductive two-dimensional metal-organic frameworks with exceptionally high volumetric and areal capacitance. *Nat. Energy* **2018**, *3*, 30.

22. Li, P.; Wang, B., Recent Development and Application of Conductive MOFs. *Isr. J. Chem.* **2018**, *58*, 1010.
23. Sun, L.; Campbell, M. G.; Dincă, M., Electrically Conductive Porous Metal–Organic Frameworks. *Angew. Chem., Int. Ed.* **2016**, *55*, 3566.
24. Wang, L.; Han, Y. Z.; Feng, X.; Zhou, J. W.; Qi, P. F.; Wang, B., Metal-organic frameworks for energy storage: Batteries and supercapacitors. *Coord. Chem. Rev.* **2016**, *307*, 361-381.
25. Murase, R.; Leong, C. F.; D'Alessandro, D. M., Mixed Valency as a Strategy for Achieving Charge Delocalization in Semiconducting and Conducting Framework Materials. *Inorg. Chem.* **2017**, *56*, 14373-14382.
26. Murase, R.; Abrahams, B. F.; D'Alessandro, D. M.; Davies, C. G.; Hudson, T. A.; Jameson, G. N. L.; Moubaraki, B.; Murray, K. S.; Robson, R.; Sutton, A. L., Mixed Valency in a 3D Semiconducting Iron-Fluoranyl Coordination Polymer. *Inorg. Chem.* **2017**.
27. Darago, L. E.; Aubrey, M. L.; Yu, C. J.; Gonzalez, M. I.; Long, J. R., Electronic Conductivity, Ferrimagnetic Ordering, and Reductive Insertion Mediated by Organic Mixed-Valence in a Ferric Semiquinoid Metal–Organic Framework. *J. Am. Chem. Soc.* **2015**, *137*, 15703-15711.
28. Abrahams, B. F.; Hudson, T. A.; McCormick, L. J.; Robson, R., Coordination Polymers of 2,5-Dihydroxybenzoquinone and Chloranilic Acid with the (10,3)-a Topology. *Cryst Growth Des* **2011**, *11*, 2717-2720.
29. Darago, L. E.; Aubrey, M. L.; Yu, C. J.; Gonzalez, M. I.; Long, J. R., Electronic Conductivity, Ferrimagnetic Ordering, and Reductive Insertion Mediated by Organic

Mixed-Valence in a Ferric Semiquinoid Metal–Organic Framework. *J. Am. Chem. Soc.* **2015**, *137*, 15703.

30. Goodenough, J. B.; Park, K.-S., The Li-Ion Rechargeable Battery: A Perspective. *J. Am. Chem. Soc.* **2013**, *135*, 1167-1176.

31. Zhang, H.; Nai, J.; Yu, L.; Lou, X., Metal–Organic–Framework–Based Materials as Platforms for Renewable Energy and Environmental Applications. *Joule* **2017**, *1*, 77-107.

CHAPTER V
OPTIMIZING CALCIUM ELECTROLYTES BY SOLVENT
MANIPULATION FOR CA BATTERIES

5-1. Abstract

Calcium is a highly attractive metal anode because of its high earth abundance and low reduction potential. However, the lack of calcium electrolytes for reversible calcium deposition significantly hampers the development of Ca rechargeable batteries. Herein, the calcium deposition/stripping behaviors of a calcium salt electrolyte, $\text{Ca}[\text{B}(\text{hfip})_4]_2$ ($[\text{B}(\text{hfip})_4]^-$ = tetrakis(hexafluoroisopropoxy)borate) were systematically studied using different working electrodes (GC, Pt, Cu, and Al) and different solvents including tetrahydrofuran (THF), dimethoxyethane (DME), and diglyme (DGM). It was found that the $\text{Ca}[\text{B}(\text{hfip})_4]_2/\text{DGM}$ electrolyte demonstrated the highest reversibility and stability in cyclic voltammetry and symmetric Ca/Ca half-cell studies. The $\text{Ca}[\text{B}(\text{hfip})_4]_2/\text{DGM}$ electrolyte was further employed to demonstrate a 3.4 V Ca battery using a FePO_4 cathode with a discharge capacity of 120 Ah/mg.

5-2. Introduction

Multivalent batteries have received increasing attention in order to developing post-Li ion battery technologies with high energy densities, low materials costs, and good cycling performance.¹⁻⁴ Particularly, significant advances have been made in developing

Adapted with permission from [Nielson, K. V.; Luo, J.; Liu, T. L., Optimizing Calcium Electrolytes by Solvent Manipulation for Calcium Batteries. *Batteries & Supercaps.*, **2020**, *3*, 766-772.]

electrolyte chemistry for Mg batteries.^{1, 3, 5-19} However, high Lewis acidity of Mg^{2+} ions makes them extremely challenging to adopt the interaction chemistry of Li ion batteries. Identifying suitable Mg^{2+} ion interaction cathode host with high kinetics and high redox potential presents a formidable task.^{2, 4} Compare to Mg^{2+} , Ca with lower Lewis acidity is believed to be promising for intercalation chemistries.²⁰ In addition, Ca metal has a low reduction potential close to Li (+0.17 V vs Li) and also has the distinct advantages of divalent redox couple $\text{Ca}^{2+/0}$ giving it high gravimetric (ca. 1337 mAh/g) and volumetric capacities (2099 mAh/cm³).²⁰ There are very limited efforts in developing Ca electrolytes for reversible Ca deposition, a prerequisite for developing Ca metal batteries.^{6, 20-24} $\text{Ca}(\text{BF}_4)_2$ in carbonate electrolytes was reported for Ca deposition and exhibited a degree of reversibility of less than 40% coulombic efficiency at 100 °C.^[21] $\text{Ca}(\text{BH}_4)_2$ in THF was reported as the first example enabling reversible Ca deposition at room temperature albeit a low anodic stability of 2.4 V vs Ca due to the highly reducing nature of the BH_4^- anion.^{22, 24} Recently Zhao-Karger and Nazar research groups simultaneously published their results describing a room temperature reversible Ca electrolyte $\text{Ca}[\text{B}(\text{hfip})_4]_2$ (hfip = tetrakis(hexafluoroisopropoxy)borate) in DME with an impressive anodic stability of above 4.0 V.^{6, 23} It is worth noting this unique $\text{Ca}[\text{B}(\text{hfip})_4]_2$ electrolyte was inspired by prior studies of corresponding $\text{Mg}[\text{Al}(\text{hfip})_4]_2$ ⁸ and $\text{Mg}[\text{B}(\text{hfip})_4]_2$ ¹⁰ electrolytes.²⁰ Both research groups used DME solvent and a noble metal working electrode to demonstrate their reversible cyclic voltammetry curves. The authors did not however inspect the electrochemical deposition behaviors of the $\text{Ca}[\text{B}(\text{hfip})_4]_2$ electrolyte using non-noble working electrode materials. In addition, the solvent effect of the $\text{Ca}[\text{B}(\text{hfip})_4]_2$ electrolyte remains unexplored. Herein, we present a systematic study of the calcium

deposition/stripping behaviors of the $\text{Ca}[\text{B}(\text{hfip})_4]_2$ calcium salt electrolyte using different working electrodes (GC, Pt, Cu, and Al) and different solvents, tetrahydrofuran (THF), dimethoxyethane (DME) and diglyme (DGM). We found that DGM, a tridentate ligand solvent molecule, enables $\text{Ca}[\text{B}(\text{hfip})_4]_2$ to manifest superior reversible and smooth Ca deposition even with a non-noble Cu working electrode.

5-3. Results and discussion

The development of the $\text{Ca}[\text{B}(\text{hfip})_4]_2$ electrolyte by Zhao-Karger and Nazar research groups were inspired by its Mg electrolyte congeners.^{8, 10} In fact, we also briefly studied this $\text{Ca}[\text{B}(\text{hfip})_4]_2$ electrolyte using a glassy carbon electrode (Figure 5-1A) when we investigated Cl-free, non-corrosive Mg electrolytes supported by weakly coordination anions.⁶ However, the poor coulombic efficiency (33%) and large overpotential were (500 mV) observed and discouraged further pursuit. The studies of the $\text{Ca}[\text{B}(\text{hfip})_4]_2$ electrolyte using Pt and Au electrodes by Zhao-Karger and Nazar research groups, respectively, yielded improved overpotential than our initial results with glassy carbon.^{6, 23} Thereby, we were promoted to study how working electrodes affect deposition electrochemistry of the $\text{Ca}[\text{B}(\text{hfip})_4]_2$ electrolyte. At first, we established a baseline result by testing the $\text{Ca}[\text{B}(\text{hfip})_4]_2$ electrolyte in DME using a Pt working electrode. A coulombic efficiency of 80% percent was calculated by summing up the total charge passed in the deposition and stripping processes (Figure 5-1A), and overpotential between the deposition and stripping was recorded as 0.33 V. These performance metrics are indeed better than the results collected by GC while Pt and GC displayed comparable anodic stability above 4.0 vs Ca. Since it is unreasonable that noble metals such as Pt or Au would be used in practical battery applications, we set out to test the reversibility of

this electrolyte upon the surface of more common materials found in batteries. Al foil, a common current collector in Li-ion batteries, was tested as working electrode in the electrolyte. A very high overpotential (>1.0 V) was observed and current observed on stripping decreased dramatically over three cycles (Figure 5-1B) with a coulombic efficiency less than 40%. However, anodic current with the Al electrode was not observed even above 4.5 V vs Ca. Then another common current collector, Cu foil, was tested in the same conditions. The reversibility of deposition/stripping (25%) on the Cu electrode was negligible and continuous oxidative decomposition was observed beyond 2.5 V vs Ca (Figure 5-1C). In addition, we hypothesized that electrolyte decomposition at reducing potential is responsible for the low coulombic efficiencies. To test this theory, cyclic voltammetry was performed at increasingly reductive potentials using the Pt electrode. Accordingly, the coulombic efficiencies dropped to lower values as the cyclic voltammetry swept to lower voltages (Figure 5-4C). This behavior may be deleterious to high voltage or fast charging battery applications where the battery anode can experience low reduction potential.

To further optimize the electrolyte stability, different ethereal solvents were tested to see if there was a solvent effect on electrolyte decomposition. A 0.25 M $\text{Ca}[\text{B}(\text{hfip})_4]_2$ in THF was tested under the same conditions as the electrolyte in DME. A lower reversibility was observed up to 60% coulombic efficiency on a Pt electrode (Figure 5-6A). However, when the CV scan was directed to more negative voltages (-1.0 V vs Ca), the reversibility completely disappeared (Figure 5-6B). This result suggested that $\text{Ca}[\text{B}(\text{hfip})_4]_2$ electrolyte had even worse reductive stability and reversibility in THF vs the DME electrolyte. It was proposed by Liao *et al.* that polydentate glyme can stabilize

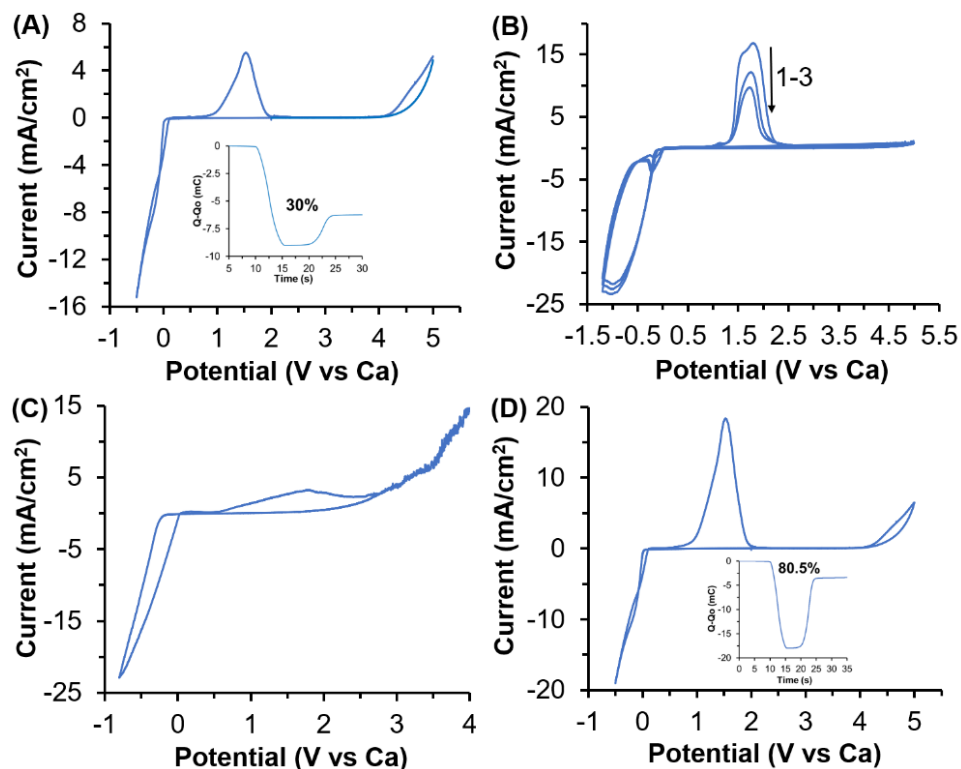


Figure 5-1. Cyclic voltammetry of a 0.25 M $\text{Ca}[\text{B}(\text{hfp})_4]_2/\text{DME}$ electrolyte solution with a glassy carbon rod counter electrode and a Ca reference electrode for A) Glassy carbon working electrode with Coulombic efficiency shown. B) Al working electrode with three cycles of decreasing current shown. C) Cu working electrode with limited reversibility and oxidation stability. D) Pt working electrode with inset showing accumulation of charge and Coulombic efficiency.

cations from interfering counter anions in Mg electrolytes.¹⁹ Since THF is a lower coordinating solvent than DME and the stability was decreased, we then chose diglyme (DGM, a tridentate ligand solvent) to test the electrolyte. DGM is also advantageous with its higher boiling point and lower vapor pressure than THF and DME solvents. A 0.25 M $\text{Ca}[\text{B}(\text{hfp})_4]_2$ in DGM was tested as the samples before.^{8, 10} To our delight, the electrolyte in DGM showed promising improvements over the tests in DME even on non-noble working electrode surfaces. A coulombic efficiency of 85.5% was calculated along with ca. 4.2 V anodic stability for the glassy carbon electrode (Figure 5-2A). On Cu foil, the Coulombic efficiency was 76% (Figure 5-1C) and on Al it was over 60% (Figure 5-

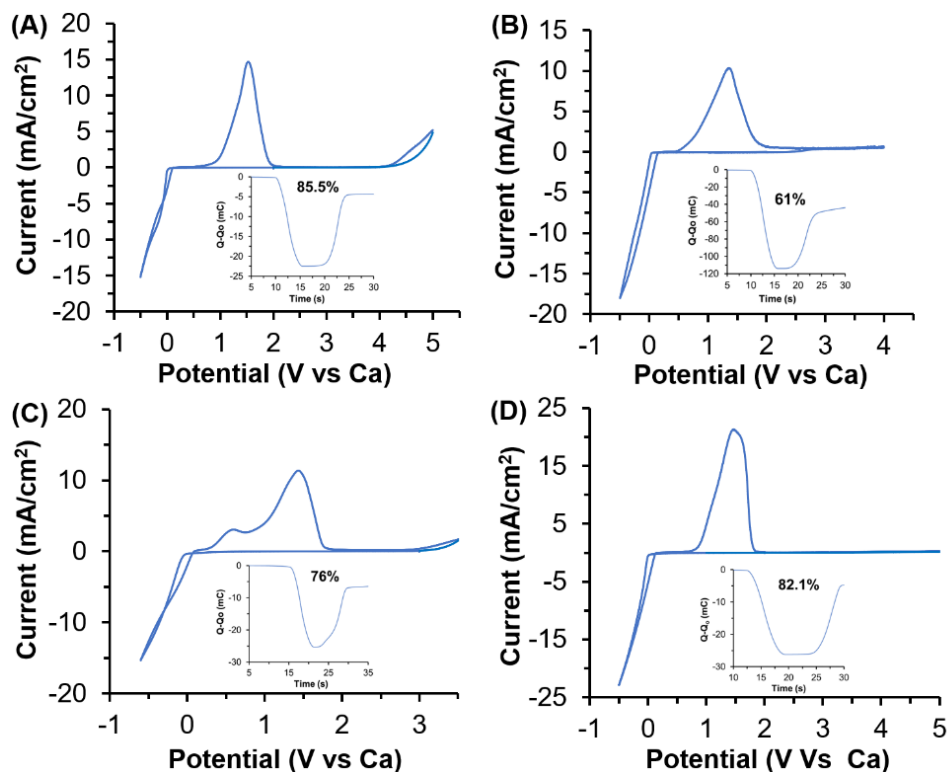


Figure 5-2. Cyclic voltammetry of a 0.25 M $\text{Ca}[\text{B}(\text{hfip})_4]_2/\text{DGM}$ electrolyte solution with glassy carbon rod counter electrode and a Ca reference electrode for A) Glassy Carbon working electrode. B) Al working electrode with inset showing accumulation of charge and Coulombic efficiency. C) Cu working electrode with Coulombic efficiency inset. D) Pt working electrode with Coulombic efficiency inset. All samples were cycled at 100 mV/s scan rate.

1D) which are both much better than the negligible reversibility observed in DME solvent. The DGM electrolyte had over 80% Coulombic efficiency and an anodic stability of near 5.0 V on a Pt electrode surface comparable to the literature report in DME (Figure 5-1B).

The electrolyte in the three different solvents was further tested in symmetric Ca/Ca cells using Ca deposited on Cu serving as both electrodes. The Current density was 1.0 mA/cm² for ten cycles then increased to 2.0, 4.0, and finally 8.0 mA/cm² while the overpotential of the cells was recorded. The cell with THF began to show voltage spikes greater than 1.0 V after 75 hours of cycling that became very severe (>3.0 V) at

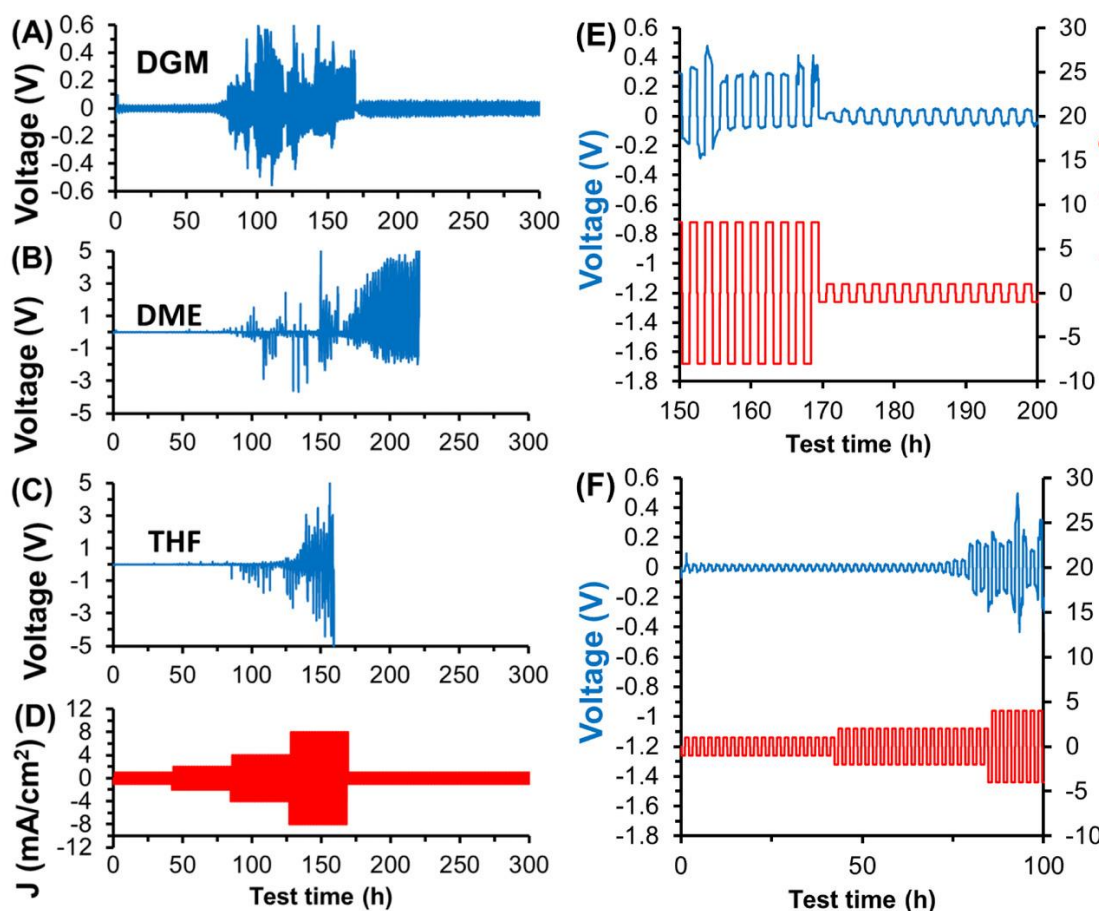


Figure 5-3. Symmetric cell evaluation of $\text{Ca}[\text{B}(\text{hfip})_4]_2$ in different solvents with Ca deposited on Cu serving as both electrodes for A) DGM, B) DME, C) THF. D) Test time and current density for the three cells, E) end cycling for DGM cell, and F) initial cycling of DGM cell.

8.0 mA/cm^2 and caused failing after 170 hours. The DME containing cell showed similar behavior to the THF cell. Voltage spikes greater than 3.0 V were observed at 4.0 mA/cm^2 current density and > 3.0 V spikes in overpotential were observed after 170 hours even at 1.0 mA/cm^2 current density. The DME containing cell failed after 220 hours (Figure 5-3B). The DGM electrolyte-based cell had better performance than both THF and DME electrolyte-based cells. The DGM electrolyte-based cell (Figure 5-3A) never had voltage spikes greater than 0.5 V even at 8.0 mA/cm^2 and remained stable with less than 100 mV overpotential at 1.0 mA/cm^2 for the entire 300 hours of testing. The spikes are believed

due to the increased cell resistance and resulting polarization at high current. According to the SEM and EDX studies (see Figure 5-3 below), it is believed that the electrolyte decomposition was accelerated at high current in the cells using the $\text{Ca}[\text{B}(\text{hfip})_4]_2/\text{DME}$ and $\text{Ca}[\text{B}(\text{hfip})_4]_2/\text{THF}$ electrolytes and led the formation of insulate CaF_2 (and possible organic) deposits on the electrode surface.

Scanning electron microscopy was employed to probe the mode of failure for the symmetric cells containing THF and DME solvents. Calcium dendrites observed on the current collector interface were observed in the DME electrolyte while the current collectors in the THF cell did not show dendrite formation. Thus, we propose the cell failure in THF and DME was caused by passivation from decomposed electrolyte. The deposition on Cu with THF solvent was very smooth and uniform. Only upon inspection of the elemental mapping was it observed that the atomic ratio of fluorine was much higher compared to Ca than the other samples suggesting that most of the deposition in THF solvent is actually CaF_2 rather than Ca metal. This observation is consistent with the complete lack of an oxygen signal from the THF sample where the Ca metal oxidized quickly in the atmosphere for the DGM and DME samples. In contrast, the CaF_2 did not undergo the same oxygenation process. The DGM cell also did not have dendritic growths but rather had islands of Ca and CaF_2 deposited in particle like morphologies.

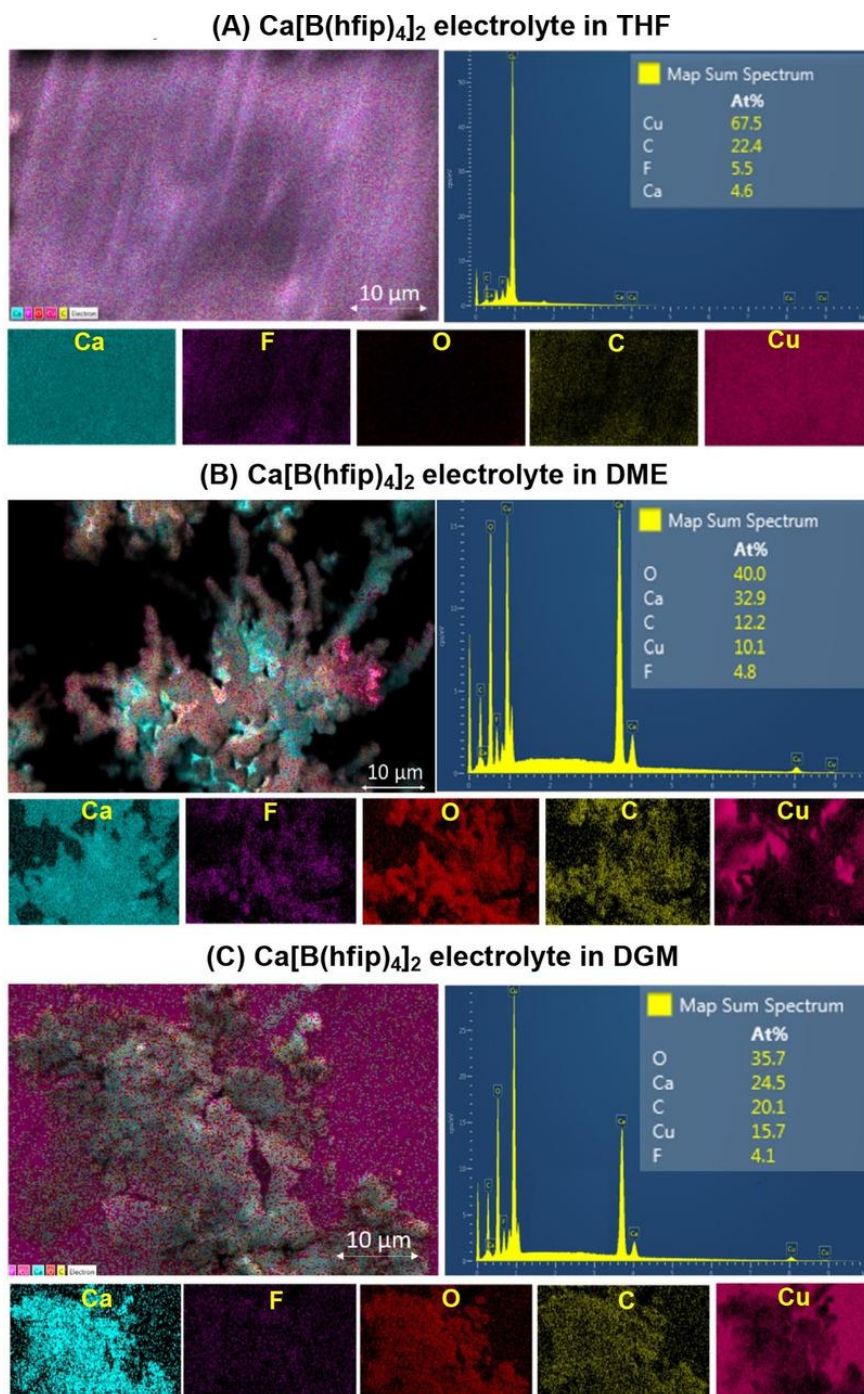


Figure 5-4. Post analysis by SEM and EDX elemental mapping of Cu current collectors from Ca|Ca symmetric cells for A) the cell using THF comprising mostly CaF_2 deposits, B) the cell using DME solvent with dendrites measured by a scale bar, and C) the cell using DGM solvent with smooth particle deposition morphology.

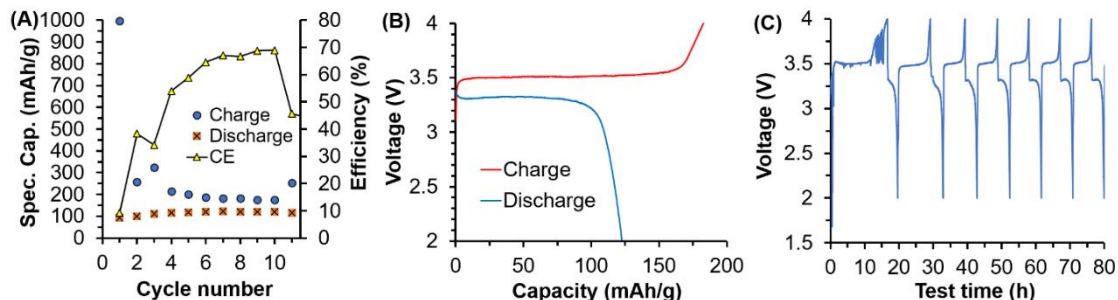


Figure 5-5 Electrochemical performance of a $\text{Ca[FePO}_4\text{]}$ rechargeable battery with a 0.25 M $\text{Ca[B(hfip)}_4\text{)]}_2\text{/DGM}$ electrolyte at 10 mA/g for charging and discharging processes. A) Charging and discharging capacities and Coulombic efficiency. B) Representative charging/discharging curves of the seventh cycle. C) Charging/discharging Voltage profile over testing time.

After the assessments of reversibility and stability of $\text{Ca[B(hfip)}_4\text{)]}_2$ electrolyte in three different solvents, it became of great interest to test the electrolyte in a full cell Ca metal battery configuration. An FePO_4 cathode was prepared by electrochemical delithiation of LiFePO_4 that was used as a Ca host. Ca metal deposited on Cu foil was used as the anode, a glass fiber separator was used as separator, and 0.25 M $\text{Ca[B(hfip)}_4\text{)]}_2$ in DGM was used as the electrolyte in a coin cell. The cell had a very high initial charge capacity possibly due to SEI formation. Then the cell was continuously tested for 10 cycles with up to a discharge capacity of 120 mAh/g and a coulombic efficiency of up to 70% (Figure 5-5A). The representative charge/discharge curves are given in Figure 5-5B and indicates a cell voltage of 3.4 V for the $\text{Ca/FePO}_4\text{/Ca[B(hfip)}_4\text{)]}_2$ battery. The cycling performance of the cell remains to be further improved but it did demonstrate that $\text{Ca[B(hfip)}_4\text{)]}_2$ could be used in a high voltage (4.0 V) application with enough anodic reversibility to achieve a relatively high discharge capacity for FePO_4 cathode (Figure 5-5). EDX mapping confirmed the Ca^{2+} presence in the FePO_4 cathode and was also used to calculate the

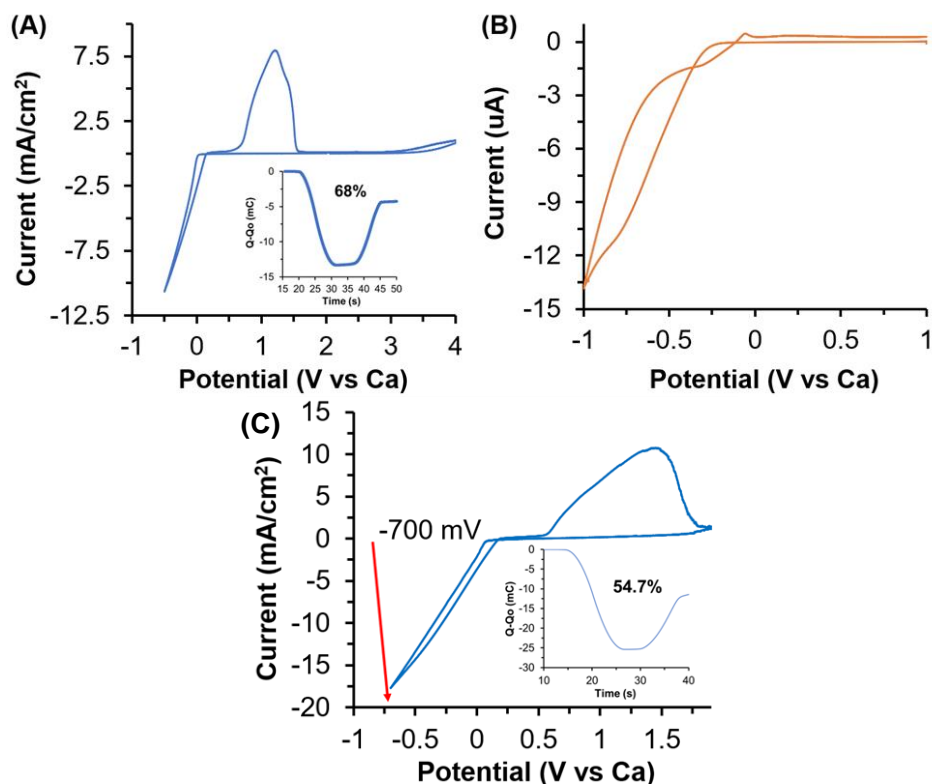


Figure 5-6. Cyclic voltammetry of 0.25M $\text{Ca}(\text{B}(\text{hfip})_4)_2$ in THF solvent with a Pt working electrode. (A) Sweeping to negative 300 mV vs CA with 68% coulombic efficiency and 3.25 V anodic stability. (B) Scanning to negative 1.0 V vs Ca with a complete loss of reversibility. (C) Cyclic voltammetry of 0.25M $\text{Ca}(\text{B}(\text{hfip})_4)_2$ in **DME** solvent with a Pt working electrode, GC counter electrode, and Ca reference electrode by sweeping to -700 mV vs Ca. Coulombic efficiency is shown in the insets with decreasing coulombic efficiency observed for increasingly negative CV sweeping voltages.

amount of Ca insertion in the FePO_4 cathode. The calculated ratio was Ca:Fe 0.43:1, giving a formula of $\text{Ca}_{0.43}\text{FePO}_4$ for the discharged state. ICP-MS was further employed to confirm the inserted Ca ions (0.43 equivalent for Fe) to the Fe Content and suggests a small amount of Li^+ in the cathode material ($\text{Li} : \text{Ca} < 1 : 4$). Table 5-1 provides the detailed element analysis of the calcinated FePO_4 cathode by EDX and ICP-MS. These preliminary Ca battery results give hope to improve long-term stability and coulombic efficiencies through future optimization.

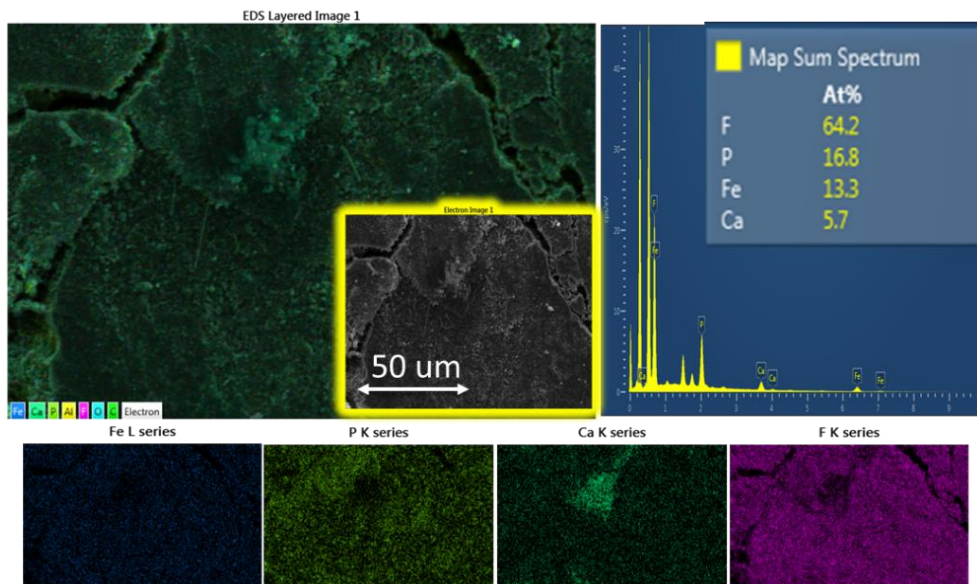


Figure 5-7. SEM-EDS post analysis of the FePO_4 electrode.

Table 5-1. Composition analysis of $\text{Li}(1-2x)\text{Ca}(x)\text{FePO}_4$ by EDS and ICP-MS analysis. Values are listed as atomic ratios. Li cannot be detected by EDS, so values were estimated based on the assumption of charge balance.

sample	method	Li	Ca	Fe	Formula
1	EDS	N.A.	0.42	1	$\text{Ca}_{0.42}\text{FePO}_4$
	ICP-MS	0.11	0.44	1	$\text{Li}_{0.11}\text{Ca}_{0.44}\text{FePO}_4$
2	EDS	N.A.	0.42	1	$\text{Ca}_{0.42}\text{FePO}_4$
	ICP-MS	0.15	0.42	1	$\text{Li}_{0.15}\text{Ca}_{0.42}\text{FePO}_4$
3	EDS	N.A.	0.40	1	$\text{Ca}_{0.42}\text{FePO}_4$
	ICP-MS	0.02	0.49	1	$\text{Li}_{0.02}\text{Ca}_{0.42}\text{FePO}_4$

5-4. Conclusions

The $\text{Ca}[\text{B}(\text{hfp})_4]_2$ electrolyte was tested using different electrodes in three different ethereal solvents to gage the current collector and solvent effects on the electrolyte stability. It was found that, the reversibility of Ca deposition and stripping of the $\text{Ca}[\text{B}(\text{hfp})_4]_2$ electrolyte in DGM (compared to DME and THF) was greatly improved

on common battery current collectors including Cu and Al and on glassy carbon. Symmetric Ca|Ca cell studies also confirmed that the DGM solvent based electrolyte showed the lowest polarization at all current densities and had the longest cycling stability over 300 hours. Only the $\text{Ca}[\text{B}(\text{hfip})_4]_2$ in the DGM cell had a smooth dendrite free morphology of mostly Ca deposits. These results suggest DGM may be a more suitable solvent for Ca electrolytes for future studies. In addition, a 3.4 V rechargeable Ca battery was demonstrated with using the $\text{Ca}[\text{B}(\text{hfip})_4]_2/\text{DGM}$ electrolyte and the FePO_4 cathode. Our results highlight the important solvent effect in developing advanced Ca electrolytes to realize durable and energy dense Ca batteries.

5-5. Experimental Section

Materials and operations: Chemicals and manipulations: $\text{Ca}(\text{BH}_4)_2 \cdot 2\text{THF}$ was purchased from TCI, dried at 100 °C in an Argon glovebox, and used directly. All experimental operations were conducted under an Argon atmosphere with H_2O and O_2 concentrations below 0.1 ppm. Hexafluoroisopropanol was stored over activated molecular sieves (4 angstroms) for at least one week before use. All solvents were purified and dried by distillation over Na whereby the initial and final 10% of solvent was separated away for less solvent sensitive chemistry.

Synthesis of $\text{Ca}[\text{B}(\text{hfip})_4]_2 \cdot 4\text{DME}$: $\text{Ca}(\text{BH}_4)_2 \cdot 2\text{THF}$ (1.0 mmol, 214 mg) was added slowly over one hour to a 5.0 ml, ultra-dry DME solution containing hexafluoroisopropanol (8.0 mmol, 1.34 g). The reaction temperature was then increased to reflux for 4 hours. Solvent was removed under reduced pressure until visibly dry then

further removed under vacuum at 80 °C for 6 hours. A fine white powder was obtained (1.13g, 85.0%). ^{19}F NMR (500 MHz CD_3CN): $\delta = -75.4$. ^{11}B NMR (500 MHz, CD_3CN): $\delta = 8.78(\text{s})$.

Cyclic voltammetry tests: All electrochemical measurements were collected with a Gamry 100E potentiostat. All cyclic voltammetry was conducted with a glassy carbon rod counter electrode and a Ca rod reference electrode. The Ca reference electrode was calibrated with ferrocene for all electrolyte solutions. Working electrodes were one of the following: Pt wire, Al wire, Cu wire, or glassy carbon disk. The surface area of the electrodes varied depending on what working electrode was in use, so all spectra are reported versus current rather than current density. All working electrodes were available commercially and used directly. All electrolytes were composed of 0.25 M $\text{Ca}(\text{B}(\text{hfp})_4)_2$ in DME, THF, or DGM. All CV tests were conducted at 100 mV/s scan rate.

SEM-EDS: SEM was done on a FEI Quanta FEG 650. SEM samples were prepared by scavenging current collectors from coin cells and affixing them to Carbon coated Al SEM sample substrates. Symmetric cells were assembled from Ca coated Cu foil as electrodes, glass fiber separator, and 50 μL specified electrolyte. All samples were soaked twice for 20 minutes in neat solvent according to which solvent (THF, DME, or DGM) was used for the electrolyte. The samples were loaded into a microscopy chamber under a cool stream of nitrogen that was quickly evacuated to less than 5×10^{-5} Torr pressure before the electron beam was initiated.

Symmetric cell tests: Symmetric cells were assembled using CR2025 coin cells with glass fiber type A separators. Cu discs deposited with Ca was used as both electrodes.

0.25M $\text{Ca}(\text{B}(\text{hfiP})_4)_2$ in either THF, DME, or DGM was used as the electrolyte. 50 μL electrolyte was used in all cells. Cells were tested galvanostatically at different current densities. A constant current was applied for one hour then the cell was rested for 10 minutes. Then the polarity was reversed, and current was applied for one hour followed by 10 minutes resting time. A safety measure was programmed into the battery tester to discontinue testing if cell voltage exceeded plus or minus 5 volts. For DME and THF containing cells the battery testing was automatically halted when overpotentials exceeded 5.0 V. For G2 containing cells the polarization of the cell never exceeded 0.5 V and continued running for more than 300 hours.

Battery tests: All batteries were tested on a Lanhe battery tester. Delithiated FePO_4 electrodes were prepared by electrochemical delithiation. 12 mm Aluminum discs containing LiFePO_4 , carbon black acetylene, and PVDF binder in a weight ratio of 80:10:10 respectively were loaded into CR2025 type coin cells with Li metal anode and 1.0 M LiTFSI in 1:1 DME:DOL electrolyte (20 μL) with a glass fiber type A separator. The batteries were charged to 4.0 V with constant current of 1.0 mA/g. The cell was then disassembled, and the cathode disc was soaked in neat DME for 20 minutes two times and then dried under vacuum at room temperature for one hour. The electrodes were then loaded into a new coin cell with Ca metal anode and 0.25 $\text{Ca}(\text{B}(\text{hfiP})_4)_2$ in THF, DME, or DGM electrolyte. Only the DGM containing cell could cycle as other solvent containing electrolytes did not allow the cell to charge with continuous current below 4.0 V vs Ca. The Ca metal batteries were cycled at 10 mAh/g with respect to the cathode active material corresponding to a C rate of C/15.

5-6. References

1. He, S.; Nielson, K. V.; Luo, J.; Liu, T. L., Recent advances on MgCl₂ based electrolytes for rechargeable Mg batteries. *Energy Storage Materials* **2017**, *8*, 184-188.
2. Canepa, P.; Sai Gautam, G.; Hannah, D. C.; Malik, R.; Liu, M.; Gallagher, K. G.; Persson, K. A.; Ceder, G., Odyssey of Multivalent Cathode Materials: Open Questions and Future Challenges. *Chem. Rev.* **2017**, *117*, 4287-4341.
3. Xu, K., Electrolytes and Interphases in Li-Ion Batteries and Beyond. *Chem. Rev.* **2014**, *114*, 11503-11618.
4. Mao, M.; Gao, T.; Hou, S.; Wang, C., A critical review of cathodes for rechargeable Mg batteries. *Chem. Soc. Rev.* **2018**, *47*, 8804-8841.
5. Luo, J.; He, S.; Liu, T. L., Tertiary Mg/MgCl₂/AlCl₃ Inorganic Mg²⁺ Electrolytes with Unprecedented Electrochemical Performance for Reversible Mg Deposition. *ACS Energy Lett.* **2017**, *2*, 1197-1202.
6. Luo, J.; Bi, Y.; Zhang, L.; Zhang, X.; Liu, T. L., A Stable, Non-Corrosive Perfluorinated Pinacolatoborate Mg Electrolyte for Rechargeable Mg Batteries. *Angewandte Chemie International Edition* **2019**, *58*, 6967-6971.
7. Liu, T.; Shao, Y.; Li, G.; Gu, M.; Hu, J.; Xu, S.; Nie, Z.; Chen, X.; Wang, C.; Liu, J., A facile approach using MgCl₂ to formulate high performance Mg²⁺ electrolytes for rechargeable Mg batteries. *J. Mater. Chem. A* **2014**, *2*, 3430-3438.
8. Herb, J. T.; Nist-Lund, C. A.; Arnold, C. B., A Fluorinated Alkoxyaluminate Electrolyte for Magnesium-Ion Batteries. *ACS Energy Lett.* **2016**, *1*, 1227-1232.

9. Zhao-Karger, Z.; Zhao, X.; Wang, D.; Diemant, T.; Behm, R. J.; Fichtner, M., Performance Improvement of Magnesium Sulfur Batteries with Modified Non-Nucleophilic Electrolytes. *Adv. Energy Mater.* **2015**, *5*, 1401155.
10. Zhao-Karger, Z.; Gil Bardaji, M. E.; Fuhr, O.; Fichtner, M., A new class of non-corrosive, highly efficient electrolytes for rechargeable magnesium batteries. *J Mater Chem A* **2017**, *5*, 10815-10820.
11. See, K. A.; Chapman, K. W.; Zhu, L.; Wiaderek, K. M.; Borkiewicz, O. J.; Barile, C. J.; Chupas, P. J.; Gewirth, A. A., The Interplay of Al and Mg Speciation in Advanced Mg Battery Electrolyte Solutions. *J. Am. Chem. Soc.* **2016**, *138*, 328-337.
12. Wen, J.; Shi, W.; Zhang, F.; Liu, D.; Tang, S.; Wang, H.; Lin, X.-M.; Lei, A., Electrooxidative Tandem Cyclization of Activated Alkynes with Sulfinic Acids To Access Sulfonated Indenones. *Org. Lett.* **2017**, *19*, 3131-3134.
13. Merrill, L. C.; Schaefer, J. L., Electrochemical Properties and Speciation in Mg(HMDS)₂-Based Electrolytes for Magnesium Batteries as a Function of Ethereal Solvent Type and Temperature. *Langmuir* **2017**, *33*, 9426-9433.
14. Merrill, L. C.; Schaefer, J. L., Conditioning-Free Electrolytes for Magnesium Batteries Using Sufone–Ether Mixtures with Increased Thermal Stability. *Chem. Mater.* **2018**, *30*, 3971-3974.
15. McArthur, S. G.; Geng, L.; Guo, J.; Lavallo, V., Cation reduction and comproportionation as novel strategies to produce high voltage, halide free, carborane based electrolytes for rechargeable Mg batteries. *Inorg. Chem. Front* **2015**, *2*, 1101-1104.

16. Jay, R.; Tomich, A. W.; Zhang, J.; Zhao, Y.; De Gorostiza, A.; Lavallo, V.; Guo, J., Comparative Study of Mg(CB11H12)2 and Mg(TFSI)2 at the Magnesium/Electrolyte Interface. *ACS Appl. Mater. Interfaces* **2019**, *11*, 11414-11420.
17. Tutusaus, O.; Mohtadi, R.; Arthur, T. S.; Mizuno, F.; Nelson, E. G.; Sevryugina, Y. V., An Efficient Halogen-Free Electrolyte for Use in Rechargeable Magnesium Batteries. *Angew. Chem. Int. Ed.* **2015**, *54*, 7900-7904.
18. Davidson, R.; Verma, A.; Santos, D.; Hao, F.; Fincher, C.; Xiang, S.; Van Buskirk, J.; Xie, K.; Pharr, M.; Mukherjee, P. P.; Banerjee, S., Formation of Magnesium Dendrites during Electrodeposition. *ACS Energy Lett.* **2019**, *4*, 375-376.
19. Lau, K.-C.; Seguin, T. J.; Carino, E. V.; Hahn, N. T.; Connell, J. G.; Ingram, B. J.; Persson, K. A.; Zavadil, K. R.; Liao, C., Widening Electrochemical Window of Mg Salt by Weakly Coordinating Perfluoroalkoxyaluminate Anion for Mg Battery Electrolyte. *Journal of The Electrochemical Society* **2019**, *166*, A1510-A1519.
20. Nielson, K. V.; Luo, J.; Liu, T. L., Dawn of Calcium Batteries. *Angew. Chem. Int. Ed.* **2020**, *59*, DOI: 10.1002/anie.201913465.
21. Ponrouch, A.; Frontera, C.; Bardé, F.; Palacín, M. R., Towards a calcium-based rechargeable battery. *Nat. Mater* **2015**, *15*, 169.
22. Wang, D.; Gao, X.; Chen, Y.; Jin, L.; Kuss, C.; Bruce, P. G., Plating and stripping calcium in an organic electrolyte. *Nature Materials* **2017**, *17*, 16.
23. Shyamsunder, A.; Blanc, L. E.; Assoud, A.; Nazar, L. F., Reversible Calcium Plating and Stripping at Room Temperature Using a Borate Salt. *ACS Energy Letters* **2019**, *4*, 2271-2276.

24. Ta, K.; Zhang, R.; Shin, M.; Rooney, R. T.; Neumann, E. K.; Gewirth, A. A., Understanding Ca Electrodeposition and Speciation Processes in Nonaqueous Electrolytes for Next-Generation Ca-Ion Batteries. *Acs Appl Mater Inter* **2019**, *11*, 21536-21542.

CHAPTER 6

PERFLOURINATED CHELATE ANION RAISES THE VOLTAGE

STABILITY FOR CA BATTERIES

6-1. Abstract

Ca metal batteries are a possible alternative to current Li technologies. Suitable electrolytes are currently underdeveloped and crucial for multivalent Ca ion batteries to be advanced. Here-in we report the synthesis and electrochemistry of a perflourinated pinacol borate Ca salt $\text{Ca}[\text{B}(\text{O}_2\text{C}_2(\text{CF}_3)_4)_2]_2$ (abbreviated as Ca-FPB). Ultra-high voltage stability (>4.5 V vs Ca) and highly efficient deposition/stripping with negligible overpotentials were found for this new electrolyte. Non passivating behavior was observed for Ca electrodes enabling long cycling (500 h) Ca|Ca symmetric cells. Full cell 3.0 V batteries featuring Prussian blue cathode delivered up to 170 mAh/g discharging capacity with Coulombic efficiencies surpassing 90%.

6-2. Introduction

Enormous ongoing growth in electrochemical energy storage calls for energy dense, sustainable alternatives to current systems.¹⁻² Moving beyond resource limited Li-ion technologies, earth abundant Ca metal has the technological merits to supplement or replace current Li-ion graphite anode architectures.³⁻⁷ Ca metal can provide high voltage (0.17 V vs Li) and volumetric energy density (2099 mAh/cm²). As such, a rich experimental research background for Ca²⁺ intercalation electrodes can be found in the literature for metal sulfides,⁸ metal oxides,⁹⁻¹³ polyanionic compounds,¹⁴ graphite,¹⁵ etc., among others. There are very limited reports however featuring Ca anode opposite to a

Ca^{2+} intercalation type cathode.¹⁶ This has been due to the historical inability to electrochemically deposit/strip Ca reversibly from an electrode. Within recent years the first example electrolyte $\text{Ca}(\text{BH}_4)_2 \cdot \text{THF}$ was found to reversibly deposit/strip Ca. Fascinating follow ups to this research have helped to understand the unique qualities of this prototype functioning electrolyte.¹⁷ Unfortunately, for all intents and purposes the highly reductive nature of the BH_4^- anion makes it unsuitable for high voltage applications. Rapidly increased attention to the Ca battery subject matter has been observed within the past year due to the introduction of an electrolyte that can plate/strip Ca^{2+} ions at room temperature, with decent efficiency, and most importantly at high voltage stability (>4.0 V). The electrolyte $\text{Ca}(\text{B}(\text{hfip})_4)_2$ makes use of a weakly coordinating fluorinated borate anion inspired by previous studies using Mg electrolytes.¹⁸⁻¹⁹ We were inspired by the effectiveness of the weakly coordinated anion motif for Ca electrolytes to test our own calcium fluorinated pinacol borate $\text{Ca}[\text{B}(\text{O}_2\text{C}_2(\text{CF}_3)_4)_2]_2$ (abbreviated as Ca-FPB, Figure 6-1). Our previous studies on non-corrosive, anodically stable, electrochemically active Mg electrolytes featured low coordinating anion FPB. In these studies, the FPB anion provided the distinct advantages of improved electrochemical stability and efficiency. Here-in we report on successful reversible Ca deposition/stripping at room temperature with Ca-FPB electrolyte. Remarkable improvements to the current voltage stability (4.5 V vs Ca) and negligible deposition overpotentials (20 mV) were afforded by Ca-FPB electrolyte. Ca anodes were found to be not impeded by decomposition products and a full cell 3.0 V battery with a Prussian blue cathode could be supported with 90% Coulombic efficiency during cycling which is unprecedented for Ca metal batteries at this time.

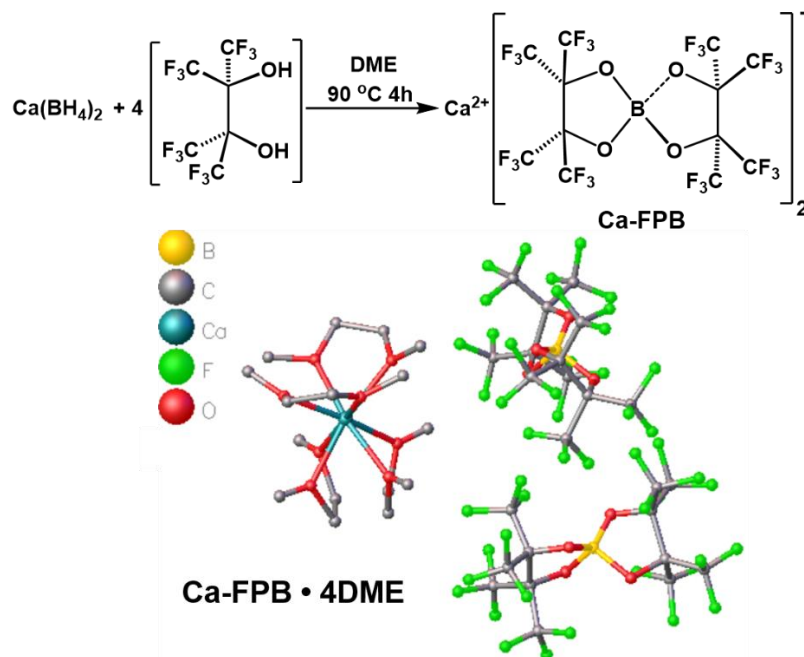


Figure 6-1. Synthesis and crystal structure for Ca-FPB (Ca, green; B, blue; O, red; C, gray; F, yellow)

6-3. Results and discussion

Ca[B(O₂C₂(CF₃)₄)₂]₂ abbreviated as Ca-FPB was prepared from Calcium Borohydride and two equivalents Hexafluoro-2,3-bis(trifluoromethyl)-2,3-butanediol were reacted in DME first at room temperature then at reflux for four hours. The solvent was removed under reduced pressure to afford a white microcrystalline solid. ¹⁹F and ¹¹B NMR spectra of the sample each contained only one signal confirming uniform product distribution. Single crystals suitable for X-ray diffraction were obtained reliably by slow evaporation of solvent from a concentrated solution at room temperature. Results from X-ray diffraction and elemental analysis confirmed the formula as C₄₀B₂O₁₆F₄₈Ca equivalent to Ca(FPB)₂ · 4DME (*M* = 1.750 g/mol). The structure was solved in the tetragonal, space group P4cc with lattice parameter *a* = 14.8309(2) Å, *c* = 28.5783(5) Å

and volume ($V = 6286.0(2) \text{ \AA}^3$) (Figure 6-1). The Ca^{2+} ions are coordinated to four chelating oxygens of DME solvent in a distorted square antiprismatic geometry. The charge is balanced by two tetrahedral FPB anions.

$\text{Ca}(\text{FPB})_2$ crystals were dissolved in DME to conduct electrochemical studies due to the high solubility (up to 0.8M) and high ionic conductivity (8.21 mS cm^{-1}) afforded by this solvent. Cyclic voltammetry (CV) was conducted at room temperature with a Pt electrode to test the ability of $\text{Ca}(\text{FPB})_2/\text{DME}$ electrolyte to deposit and strip Ca at the surface while avoiding possible alloying¹⁷ reactions. As shown in the CV in Figure 6-2A, the Ca -FPB electrolyte displayed reversible deposition/stripping behavior from the first cycle with an almost negligible overpotential for deposition (15 mV) and stripping (5 mV). After only two cycles, the electrolyte/electrode were properly conditioned to return over 70 percent round trip Coulombic efficiency that was maintained from cycle three to cycle ten. The very minimal observed overpotentials are beneficial due to improved deposition/stripping energy efficiency.

When compared to previously reported Ca electrolytes $\text{Ca}(\text{BH}_4)_2 \cdot \text{THF}$ (c.a. 100 mV), and $\text{Ca}(\text{B}(\text{hfp})_4)_2$ (>300 mV), Ca -FPB (20 mV) showed the lowest combined deposition/stripping overpotentials. Since it is of great interest to utilize Ca electrolytes in high voltage energy storage applications, the cathodic stability of the 0.8M Ca -FPB electrolyte was tested with various working electrodes. As seen in figure 6-2B, the onset voltage for electrolyte/solvent decomposition exceeded 4.5 V vs a Ca metal reference for all electrodes tested excluding Cu . Glassy carbon and Al showed stabilities greater than 5.0 V which is higher than the voltage stability of DME solvent. These results suggest Ca -FPB partially decomposes at the surface of the electrode in a favorable manner to

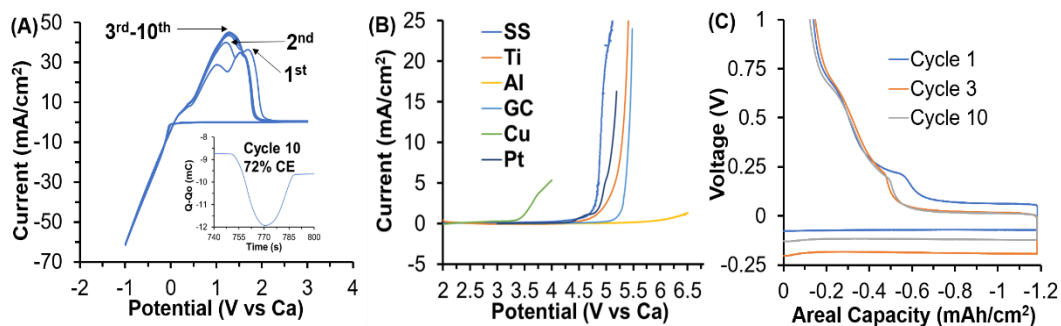


Figure 6-2. Electrochemical analysis of a 0.8M Ca-FPB electrolyte by (A) Cyclic voltammetry for ten cycles with Pt working, Ca reference, and glassy carbon rod counter electrodes. Scan rate 100 mV/s. Inset showing tenth cycle Coulombic efficiency. (B) Linear sweep voltammetry using labeled material as working electrode. (C) Reversible areal capacity on a Pt disc working electrode at 0.12 mA/cm² current density.

passivate the electrode surface against parasitic high voltage side reactions. At the same time the electrode is not passivated to Ca²⁺ ions deposition and stripping. Galvanostatic deposition/stripping with Ca-FPB electrolyte was next conducted to ascertain the electrochemical reversibility (Figure 6-2C). At a low current (0.12 mA/cm²), up to 88 percent Coulombic efficiencies were observed for a deposited areal capacity of 1.2 mAh/cm². The improved reversibility under galvanostatic conditions was attributed to the low deposition polarization of the electrolyte (70 mV).

With unprecedented overpotentials and high voltage stability in tow, it became incumbent to investigate the cause for the Coulombic efficiencies ($\approx 70\%$) calculated from cyclic voltammetry. As such, stainless steel (SS) galvanostatically plated to 1.2

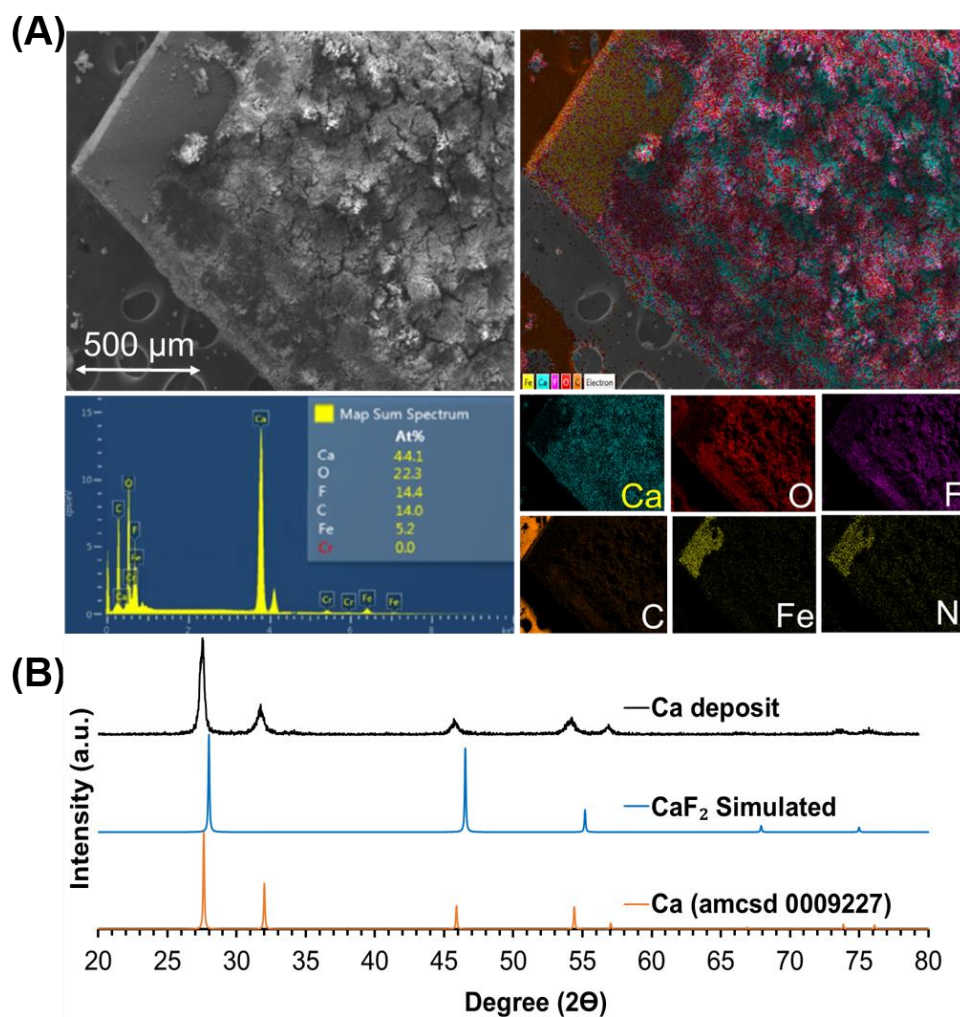


Figure 6-3. Characterization of deposition products from Ca-FPB by (A) SEM EDS of a SS substrate deposited to 1.2 mAh/cm^2 . EDS spectra, lower left, show Ca the major deposition product. And (B) Powder X-ray diffraction comparing the Ca deposits (black) to simulated spectra for CaF_2 (Blue) and Ca metal (orange).

mAh/cm^2 using a $0.8 \text{ M Ca(FPB)}_2/\text{DME}$ electrolyte (figure 6-3A). The major deposition product was Ca (45%) followed by surface oxides (17% on Cu, 22% on SS). Fluorine was detected (14% on SS, 17% on Cu) in addition to a small amount carbon indicating some reductive decomposition of Ca(FPB)_2 to CaF_2 or trapped electrolyte on the surface. To prove Ca deposition, powder X-ray diffraction of the deposits comparing the diffraction pattern of the deposits to the simulated spectra for Ca and CaF_2 gave clear evidence for the presence of metallic Ca. Especially with matching signals at 32, 57, and

76 Θ 2-theta that are present for both the deposits and metallic Ca but are missing for CaF_2 . To gain a better understanding of the decomposition products Fourier transform infrared spectroscopy was conducted on the deposits. A weak absorption at 3650 cm^{-1} indicates Ca(OH)_2 and stronger absorptions in the fingerprint region are characteristic of carbonate decomposition products (CO_3 , 800 cm^{-1} , w), (C-O, 1100 , w), (C=O, 1300 m). Since no carbonate solvents were present in this study, we attribute metallic Ca from the deposits had reacted with atmospheric CO_2 during testing. More interesting was the strong sharp peak at 1400 cm^{-1} . This peak was consistent for all deposits and we tentatively assigned it as C-F since it is in the appropriate range for such a bond. From the combined characterization of deposits, we concluded that Ca is indeed the major deposition product with CaF_2 being the major decomposition product hindering the round-trip Coulombic efficiencies for Ca(FPB)_2 electrolyte.

With less than 100% Coulombic efficiency, an electrolyte will eventually fail to conduct ions in an energy storage device as electrolyte is consumed. In the case of Ca metal batteries, the primary issue with long term cyclability has been passivation/deactivation of the electrode.^{2-3, 16, 20-21} Ca(FPB)_2 tends to not passivate the electrode in CV experiments so we tested the long-term cycling stability of a symmetric Ca|Ca cell using excess Ca (10mg) on each side. This symmetric type coin cell battery was tested galvanostatically at 0.2, 0.4, 0.8, 1.2, 1.6, and 2.0 mA/cm^2 current densities. As seen in figure 6-4A, the polarization of the cell was initially 60 mV but decreased to less than 5 mV within 10 cycles at 0.2 mA/cm^2 . The polarization remained negligible (<5mV) even at high current densities (2.0 mA/cm^2) consistent with the ultra-low overpotentials observed in CV. After high current density tests, the current was brought

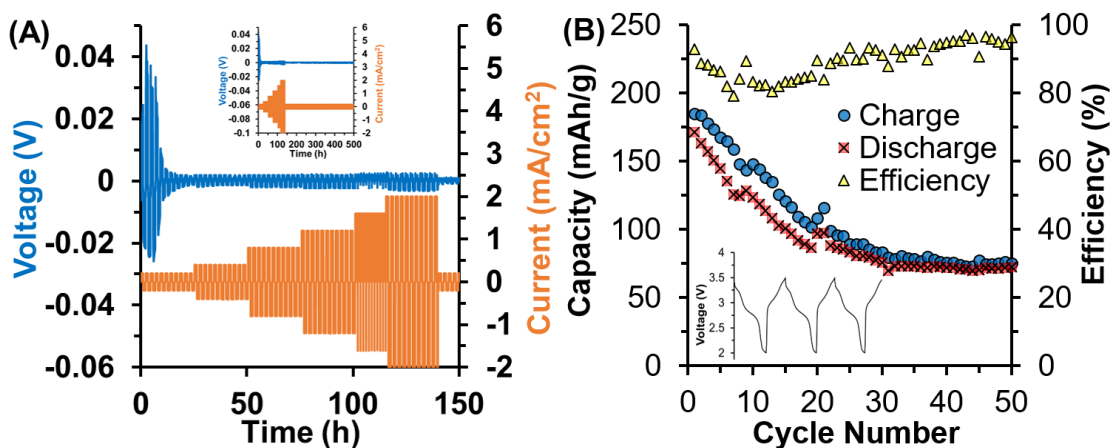


Figure 6-4. Battery tests with Ca-FPB using (A) a Ca|Ca symmetric cell tested at varying currents galvanostatically with polarization curve. Inset showing 500-hour longevity of the cell. And (B) A Ca|Fe(CN)₆ battery cycled between 2.0 and 3.5 V at 15 mA/g with inset showing voltage profile.

back to 0.2 mA/cm² for long term testing. The cell could cycle for 500 hours without failing which is to our knowledge the longest running symmetric Ca|Ca type coin cell to date with the lowest cell polarization.

To finalize the study of the high Voltage Ca(FPB)₂ / DME electrolyte it was of great interest to test a high Voltage Ca metal battery. For this study we chose (Prussian Blue) Na[Fe^{III}Fe^{II}(CN)₆] as a well-researched, high voltage Ca²⁺ intercalation type host material.²²⁻²⁷ First the material was desodiated electrochemically by charging to 4.0V Vs Na (figure 6-5A) before use in the Ca battery. The desodiated Prussian Blue was paired with a Ca metal anode and 0.8M Ca-FPB electrolyte with glass fiber separator to prepare a coin cell type battery. The cell was tested galvanostatically at 15 mA/g or approximately 0.1C current density for charging and discharging. The lower and upper cut-off voltages were 2.0 V and 3.5 V respectively. The average operating voltage of the

cell was 3.0 V and it could deliver a high discharge capacity of 171 mAh/g in the first cycle (Figure 4B). Upon charging a Coulombic efficiency of 92% was

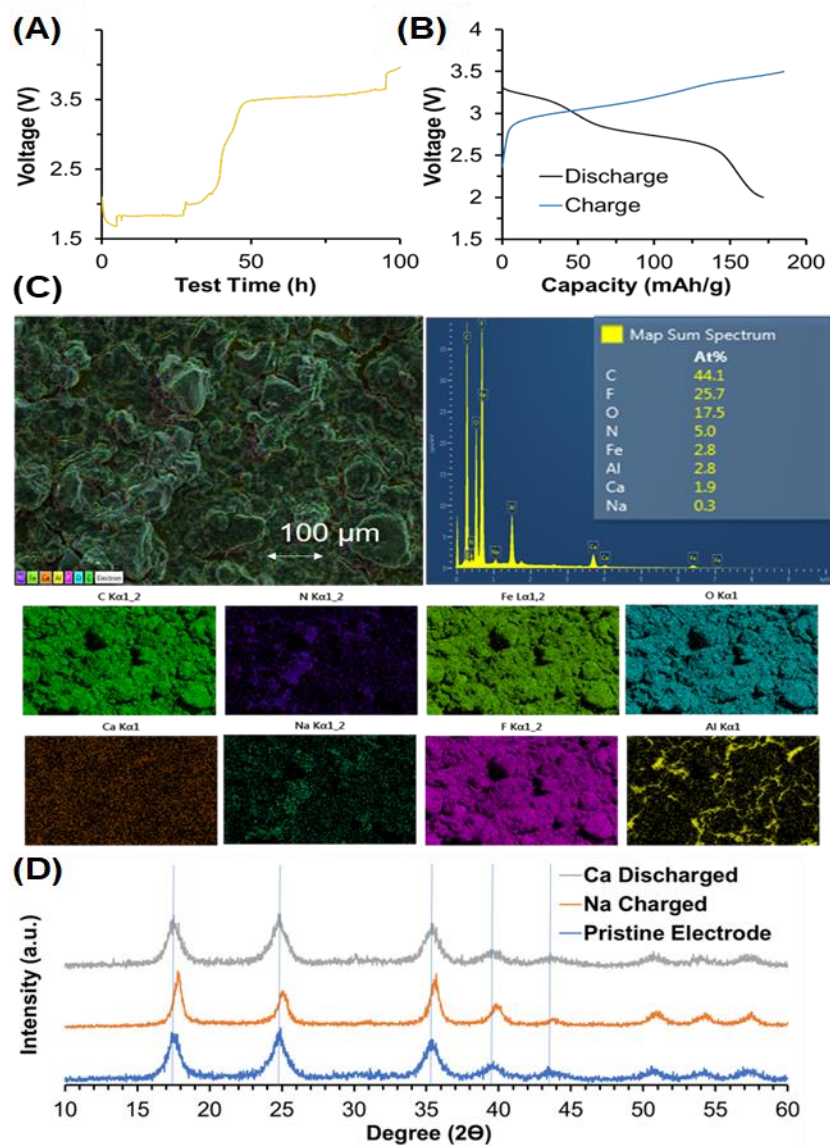


Figure 6-5. (A) Electrochemical desodiation process for $\text{NaFe}_2(\text{CN})_6$. (B) Charge/discharge profile taken from the first cycle for the $\text{Ca}|\text{Ca-FPB}|\text{Fe}_2(\text{CN})_6$ battery. (C) Post analysis of the $\text{Ca}_x\text{Fe}_2(\text{CN})_6$ electrode by scanning electron microscopy and electron dispersive spectroscopy. The electrode was harvested from the cell in the discharged (2.0 V) State. (D) Powder X-ray diffraction pattern of Prussian Blue electrodes that were pristine (blue), charged galvanostatically to 4.0 V (orange), and discharged to 2.0 V in a $\text{Ca}|\text{Ca-FPB}|\text{PB}$ cell (grey). The vertical blue lines are placed to easier visualize peak shift.

recorded for the first cycle and increased to as high as 94% in cycle 50. Reversible intercalation was confirmed by PXRD with characteristic peak shifting observed (Figure 5D). The discharge and charge capacities decayed by 50% in 50 cycles. The decay mechanism was attributed to instability of the cathode upon initial cycling and the possibility of parasitic irreversible side reactions. Large amounts of Fluorine (25%) were detected by EDS of the cathode after cycling indicative of SEI formation (Figure 5-5C). It is evident from the comparison of the symmetric cell data that reversibility at the anode is optimal. The 0.8M Ca-FPB electrolyte could evidently support the high voltage $\text{Fe}_2(\text{CN})_6$ battery with capacity decay originating from deleterious cathode side reactions .

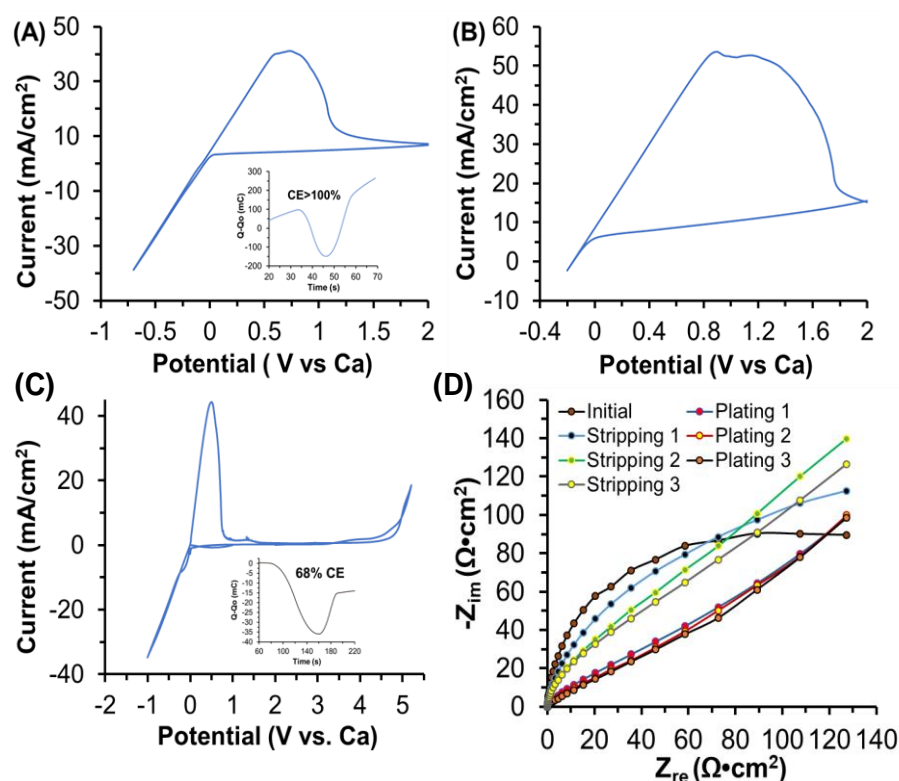


Figure 6-6. (A-B) Cyclic voltammograms of 0.8 M Ca-FPB using a flooded Ca electrode setup i.e. working, counter, and reference electrodes were Ca metal. Scan rate 100 mV/s. (C) Cyclic voltammetry showing full voltage window -1.0 V to 5.0 V versus a Ca metal reference electrode. Scan rate 20 mV/s. (D) Electrochemical impedance spectroscopy Nyquist plot. Data were collected interim galvanostatic deposition stripping processes performed in figure 6-1D.

6-4. Conclusion

In this work we introduced a new electrolyte, based on the weakly coordinating anion motif, to a very limited library of Ca salts that allow for reversible room temperature deposition/stripping at an electrode surface. The electrolyte 0.8M Ca-FPB/DME was found to possess superior qualities in terms of overpotentials and voltage stabilities. Coulombic efficiencies were attributed to reductive anion decomposition to CaF_2 . Symmetric Ca|Ca cells were not impeded by decomposition products and could function for 500 hours due to the proposed ion conducting nature or SEI on the surface. A 3.0 V Ca| $\text{Fe}_2(\text{CN})_6$ battery was demonstrated with high initial discharge capacities (170 mAh/g). As reversible Ca electrolytes continue to evolve, it is crucial at this point to develop positive electrode materials to match long term cycling with good stability.

6-5. Synthesis and Characterization

Chemicals and Manipulations.

$\text{Ca}(\text{BH}_4)_2 \cdot 2\text{THF}$ and CaH_2 were purchased from Sigma-Aldrich and used as received. Hexafluoro-2,3-bis(trifluoromethyl)-2,3-butanediol was purchased from TCI and stored on 4Å molecular sieves for one week before use. Ca metal (99.9%), purchased from GalliumSource, was scoured with a metal file and fine grit sandpaper to remove surface oxides. Cu and stainless-steel foil, also purchased from GalliumSource, were polished with n-methyl-2-pyrrolidinone to remove surface oxides then place under vacuum at 80 °C for 10 hours to completely dry. All preparation and electrochemical tests were conducted in an Argon atmosphere glovebox ($C_{\text{Oxygen}} < 1 \text{ ppm}$, $C_{\text{Water}} < 1 \text{ ppm}$). DME solvent was degassed via freeze pump thaw (4X), then distilled over a benzophenone sodium mixture, and finally stored over CaH_2 in the glovebox. H_2O

concentrations in the solvent were undetectable by ^1H -NMR (Bruker 500 MHz). All glassware used for synthesis or analysis was scrubbed with deionized water and acetone, dried at 150 °C before direct transport into the glovebox. Conductivities of electrolytes were measured using a Mettler Toledo conductivity meter at room temperature. ^1H -, ^{19}F -, and ^{11}B -NMR spectra were collected using a Bruker 500 MHz NMR spectrometer. All electrochemical experiments were conducted with a Gamry 1000e potentiostat. Scanning electron microscopy (SEM) measurements were conducted on a FEI Quanta 650 (FEI, USA). X-ray diffraction (XRD) spectra were collected on a Rigaku MiniflexII Desktop X-ray diffractometer. Battery tests were conducted using a Lanhe battery testing system. The working electrode and reference electrode were polished using Al_2O_3 before electrochemical tests. FT-IR was done on a Perkin Elmer Spectrum 100 FT-IR spectrometer with universal ATR sampling accessory. Elemental analysis was conducted by Atlantic Microlabs.

Synthesis of $\text{Ca}[\text{BO}_2\text{C}_2(\text{CF}_3)_4]_2$ (Ca-FPB).

In an Argon atmosphere glovebox at room temperature; 1.07 g solid $\text{Ca}(\text{BH}_4)_2 \cdot 2\text{THF}$ (5.00 mmol, 1.00 eq.) was added to a solution containing 6.68 g hexafluoro-2,3-bis(trifluoromethyl)-2,3-butanediol (20 mmol, 4.0 eq.) and 20 ml of DME. H_2 gas will evolve rapidly. The reaction mixture was stirred at room temperature for 12 h then under reflux at 95 °C for 4 h. Solvent was removed under vacuum; first at room temperature until visibly dry followed by 100 °C (vacuum oven) for 24 hours. Further purification steps were not required to yield the final product, $\text{Ca}[\text{BO}_2\text{C}_2(\text{CF}_3)_4]_2$ (Ca-FPB), as a rare white powder in quantitative yield. ^{19}F -NMR (MeCN-d_3 , 470 MHz, ppm): δ -70.48 (s,

48F). ¹¹B-NMR (MeCN-d₃, 160 MHz, ppm): δ 18.34 (s, 2B). Elemental analysis for Ca-FPB•4DME, C₄₀H₄₀B₂F₄₈CaO₁₆; calculated: C 27.45, H 2.30; found: C 26.87, H 2.35.

Preparation of Ca-FPB electrolyte.

To obtain a saturated 0.8 M Ca-FPB electrolyte, Ca-FPB (1.4 g, 0.8 mmol) was added to 1.0 ml DME solvent in a 4ml glass vial. 50 mg CaH₂ was added. The vial was capped and sealed with electrical tape. The mixture was stirred at 50 °C for 16 hours. A clear colorless solution was obtained after filtration through a 100µ PTFE syringe filter. Electrochemical tests were conducted immediately.

Preparation of Na[Fe(III)Fe(II)(CN)₆] (Prussian Blue).

A slightly modified version based on Kuperman et al²² was followed. Briefly, FeCl₃ (1.25 mmol) dissolved in 25 ml DI H₂O was added to a 60 °C 25 ml aqueous solution of 1.2 g Sodium ferrocyanide (Na₄Fe(CN)₆) (2.50 mmol) and left stirring for two hours. The solids were extracted via centrifugation and rinsing with a 1:2 V:V EtOH:H₂O mixture for three iterations. The product was then dried under vacuum at 60 °C for 16 hours then at 150 °C for 72 hours to remove lattice water. 730 mg, 100% yield, dark blue powder was obtained. Cubic and confirmed by PXRD.

Crystal Structural Determination.

Single crystals of C₄₀B₂O₂₄F₄₈Ca [Ca-FPB] were grown by leaving a concentrated DME solution of Ca-FPB in glovebox conditions for one week. A suitable crystal was collected. The crystal was kept at 100.00 K during data collection. Using Olex2 [1], the structure was solved with the ShelXT [2] structure solution program using Intrinsic

Phasing and refined with the ShelXL [3] refinement package using Least Squares minimization. All non-hydrogen atoms were refined with anisotropic thermal parameters.

1. Dolomanov, O.V., Bourhis, L.J., Gildea, R.J, Howard, J.A.K. & Puschmann, H. (2009), *J. Appl. Cryst.* 42, 339-341.
2. Sheldrick, G.M. (2015). *Acta Cryst.* A71, 3-8.
3. Sheldrick, G.M. (2015). *Acta Cryst.* C71, 3-8.

Table 6-1. Crystal data and structure refinement for Ca-FPB.

Identification code	Ca-FPB
Empirical formula	C40B2O16F48Ca
Formula weight	1750.1
Temperature/K	100.00(10)
Crystal system	tetragonal
Space group	P4cc
a/Å	14.8309(2)
b/Å	14.8309(2)
c/Å	28.5783(5)
$\alpha/^\circ$	90
$\beta/^\circ$	90
$\gamma/^\circ$	90
Volume/Å ³	6286.0(2)
Z	3
$\rho_{\text{calc}}/\text{cm}^3$	1.457
μ/mm^{-1}	0.239
F(000)	2682
Radiation	MoK α ($\lambda = 0.71073$)
2θ range for data collection/ $^\circ$	3.884 to 61.348
Index ranges	$-20 \leq h \leq 21, -21 \leq k \leq 20, -40 \leq l \leq 40$
Reflections collected	125801
Independent reflections	9594 [Rint = 0.0413, Rsigma = 0.0274]

Data/restraints/parameters	9594/1/476
Goodness-of-fit on F2	1.683
Final R indexes [$I \geq 2\sigma(I)$]	R1 = 0.1190, wR2 = 0.3486
Final R indexes [all data]	R1 = 0.1501, wR2 = 0.3922
Largest diff. peak/hole / e \AA^{-3}	3.72/-0.97
Flack parameter	0.54(2)

Electrochemical Measurements

Three electrode tests.

Electrochemical measurements were performed with a Gamry 1000e potentiostat with three-electrode setup. For cyclic voltammetry (CV), linear sweep voltammetry (LSV), and Galvanostatic deposition experiments, a Pt disc (1.0 mm diameter) was used as working electrode with Ca metal serving as both counter and reference electrodes. For electrochemical impedance spectroscopy, the reference electrode was removed from the cell. A saturated 0.8 M Ca-FPB / DME electrolyte was used for all measurements.

Ca|Fe₂(CN)₆ Battery.

Na[Fe(II)Fe(III)(CN)₆], Ketjen black acetylene, and PVDF binder were ground in a mortar with NMP to form a slurry. The slurry was coated onto Al foil via doctor blading. Discs (1.0 cm diameter) were punched then dried at 120 °C for 12 hours. Electrochemical desodiation of Prussian blue occurred in a CR2025 Coin cell with a

Na[Fe(II)Fe(III)(CN)₆] cathode (2.0 mg/cm² mass loading), Ca anode, glass fiber separator and 1.0M Ca(FPB)₂ in DME electrolyte charged to 4.0 V Galvanostatically at 0.01 mA/cm² current density. The cell was deconstructed to harvest the cathode which was soaked in neat DME for 20 minutes twice. The electrode was then dried under reduced pressure for 20 minutes before further utilization in batteries or before spectroscopy was done. Desodiated electrodes were transferred to new coin cells with fresh Ca metal anode and 0.8 M Ca-FPB electrolyte (50 μ L). Cells were first discharged (2.0 V) then charged (3.5 V) at 15 mA/g current density.

Symmetric Ca|Ca-FPB|Ca Cell Test.

The symmetric Ca|Ca-FPB|Ca tests were performed on 2032 type coin cell and assembled in an Ar-filled glovebox (H₂O < 1 ppm, O₂ < 1 ppm). The coin cell was assembled using Ca metal discs (d = 1.2 cm) on both working and counter electrodes and 50 μL 0.8 M Ca-FPB/DME as electrolyte. Galvanostatic charge-discharge tests were conducted on a Lanhe (Wuhan, China) tester.

6-6. References

1. Ponrouch, A.; Bitenc, J.; Dominko, R.; Lindahl, N.; Johansson, P.; Palacin, M. R., Multivalent rechargeable batteries. *Energy Storage Mater.* **2019**, *20*, 253-262.
2. Ponrouch, A.; Frontera, C.; Bardé, F.; Palacín, M. R., Towards a calcium-based rechargeable battery. *Nat. Mater* **2015**, *15*, 169.
3. Arroyo-de Dompablo, M. E.; Ponrouch, A.; Johansson, P.; Palacín, M. R., Achievements, Challenges, and Prospects of Calcium Batteries. *Chem. Rev.* **2019**.
4. Elia, G. A.; Marquardt, K.; Hoepfner, K.; Fantini, S.; Lin, R.; Knipping, E.; Peters, W.; Drillet, J.-F.; Passerini, S.; Hahn, R., An Overview and Future Perspectives of Aluminum Batteries. *Adv. Mater.* **2016**, *28*, 7564-7579.
5. Gummow, R. J.; Vamvounis, G.; Kannan, M. B.; He, Y., Calcium-Ion Batteries: Current State-of-the-Art and Future Perspectives. *Adv. Mater.* **2018**, *30*, 1801702.
6. Verrelli, R.; Black, A. P.; Pattanathummasid, C.; Tchitchekova, D. S.; Ponrouch, A.; Oró-Solé, J.; Frontera, C.; Bardé, F.; Rozier, P.; Palacín, M. R., On the strange case of divalent ions intercalation in V₂O₅. *J. Power Sources* **2018**, *407*, 162-172.
7. Wang, H.; Yu, D.; Kuang, C.; Cheng, L.; Li, W.; Feng, X.; Zhang, Z.; Zhang, X.; Zhang, Y., Alkali Metal Anodes for Rechargeable Batteries. *Chem* **2019**, *5*, 313-338.
8. Tchitchekova, D. S.; Ponrouch, A.; Verrelli, R.; Broux, T.; Frontera, C.; Sorrentino, A.; Bardé, F.; Biskup, N.; Arroyo-de Dompablo, M. E.; Palacín, M. R., Electrochemical Intercalation of Calcium and Magnesium in TiS₂: Fundamental Studies Related to Multivalent Battery Applications. *Chem. Mater.* **2018**, *30*, 847-856.

9. Arroyo-de Dompablo, M. E.; Krich, C.; Nava-Avendaño, J.; Palacín, M. R.; Bardé, F., In quest of cathode materials for Ca ion batteries: the CaMO₃ perovskites (M = Mo, Cr, Mn, Fe, Co, and Ni). *PCCP* **2016**, *18*, 19966-19972.
10. Cabello, M.; Nacimiento, F.; González, J. R.; Ortiz, G.; Alcántara, R.; Lavela, P.; Pérez-Vicente, C.; Tirado, J. L., Advancing towards a veritable calcium-ion battery: CaCo₂O₄ positive electrode material. *Electrochem. Commun.* **2016**, *67*, 59-64.
11. Torres, A.; Bardé, F.; Arroyo-de Dompablo, M. E., Evaluation of cobalt oxides for calcium battery cathode applications. *Solid State Ionics* **2019**, *340*, 115004.
12. Vo, T. N.; Kim, H.; Hur, J.; Choi, W.; Kim, I. T., Surfactant-assisted ammonium vanadium oxide as a superior cathode for calcium-ion batteries. *J. Mater. Chem. A* **2018**, *6*, 22645-22654.
13. Xu, X.; Duan, M.; Yue, Y.; Li, Q.; Zhang, X.; Wu, L.; Wu, P.; Song, B.; Mai, L., Bilayered Mg_{0.25}V₂O₅·H₂O as a Stable Cathode for Rechargeable Ca-Ion Batteries. *ACS Energy Lett.* **2019**, *4*, 1328-1335.
14. Lipson, A. L.; Kim, S.; Pan, B.; Liao, C.; Fister, T. T.; Ingram, B. J., Calcium intercalation into layered fluorinated sodium iron phosphate. *J. Power Sources* **2017**, *369*, 133-137.
15. Emery, N.; Hérold, C.; Lagrange, P., Structural study and crystal chemistry of the first stage calcium graphite intercalation compound. *J. Solid State Chem.* **2005**, *178*, 2947-2952.
16. Nielson, K. V.; Luo, J.; Liu, T. L., Optimizing Calcium Electrolytes by Solvent Manipulation for Calcium Batteries. *Batteries & Supercaps* **2020**, *n/a*.

17. Hahn, N. T.; Self, J.; Seguin, T. J.; Driscoll, D. M.; Rodriguez, M. A.; Balasubramanian, M.; Persson, K. A.; Zavadil, K. R., The critical role of configurational flexibility in facilitating reversible reactive metal deposition from borohydride solutions. *J. Mater. Chem. A* **2020**, *8*, 7235-7244.
18. Li, Z.; Fuhr, O.; Fichtner, M.; Zhao-Karger, Z., Towards stable and efficient electrolytes for room-temperature rechargeable calcium batteries. *Energy Environ. Sci.* **2019**.
19. Luo, J.; Bi, Y.; Zhang, L.; Zhang, X.; Liu, T. L., A Stable, Non-Corrosive Perfluorinated Pinacolatoborate Mg Electrolyte for Rechargeable Mg Batteries. *Angew. Chem. Int. Ed.* **2019**, *58*, 6967-6971.
20. Liu, X.; Elia, G. A.; Passerini, S., Evaluation of counter and reference electrodes for the investigation of Ca battery materials. *J. Power Sources Advances* **2020**, *2*, 100008.
21. Verrelli, R.; Black, A.; Dugas, R.; Tchitchekova, D.; Ponrouch, A.; Palacin, M. R., Steps Towards the Use of TiS₂ Electrodes in Ca Batteries. *J. Electrochem. Soc.* **2020**, *167*, 070532.
22. Kuperman, N.; Padigi, P.; Goncher, G.; Evans, D.; Thiebes, J.; Solanki, R., High performance Prussian Blue cathode for nonaqueous Ca-ion intercalation battery. *J. Power Sources* **2017**, *342*, 414-418.
23. Lee, C.; Jeong, S.-K., Modulating the hydration number of calcium ions by varying the electrolyte concentration: Electrochemical performance in a Prussian blue electrode/aqueous electrolyte system for calcium-ion batteries. *Electrochim. Acta* **2018**, *265*, 430-436.

24. Lipson, A. L.; Pan, B.; Lapidus, S. H.; Liao, C.; Vaughey, J. T.; Ingram, B. J., Rechargeable Ca-Ion Batteries: A New Energy Storage System. *Chem. Mater.* **2015**, *27*, 8442-8447.
25. Padigi, P.; Goncher, G.; Evans, D.; Solanki, R., Potassium barium hexacyanoferrate – A potential cathode material for rechargeable calcium ion batteries. *J. Power Sources* **2015**, *273*, 460-464.
26. Shiga, T.; Kondo, H.; Kato, Y.; Inoue, M., Insertion of Calcium Ion into Prussian Blue Analogue in Nonaqueous Solutions and Its Application to a Rechargeable Battery with Dual Carriers. *The Journal of Physical Chemistry C* **2015**, *119*, 27946-27953.
27. Wang, W.; Gang, Y.; Hu, Z.; Yan, Z.; Li, W.; Li, Y.; Gu, Q.-F.; Wang, Z.; Chou, S.-L.; Liu, H.-K.; Dou, S.-X., Reversible structural evolution of sodium-rich rhombohedral Prussian blue for sodium-ion batteries. *Nat. Commun.* **2020**, *11*, 980.

CHAPTER 7

CONCLUSION

Transition metal oxides (TMOs) currently used in Li-ion batteries are typically prepared by flame pyrolysis of Co, Ni, and Mn salts plus LiOH. These reactions often require continuous high temperatures greater than 700 °C for extended periods of time. In addition to the high energy demand for synthesis, this class of materials is Li⁺ intercalated in its pristine state. This results in cathode materials that are in the completely discharged state when batteries are assembled. As such, all Li-ion batteries must be charged, expending more resources, before they are sold. Overall, the preparation and use of TMOs as cathode materials in Li-ion batteries is incredibly energy (resource) expensive.

A key goal of the battery research presented in this dissertation was to develop practical methods for synthesizing electrode materials. Metal organic frameworks (MOFs) were chosen due their infinite modularity in metal and ligand as an alternative to TMOs. 2,5-dihydroxy-1,4-benzoquinone (DBQ) was chosen as the ligand for this research due to recently reported high conductivity MOFs featuring this ligand in addition to its facile 2-electron redox mechanism and ultra-small molecular weight. Reported syntheses of MOFs materials featuring this ligand were energy (resource) expensive and typically had negligible yields. In chapter 2 of this dissertation we successfully designed a facile aqueous benchtop reaction for DBQ MOFs. This method was much safer than the previously reported sealed glass vial solvothermal reactions. The most important finding our results in chapter 2 was the ability to produce 100% yield of crystalline MOFs in a reaction that can be scaled to produce grams or kilograms of

electrode materials. Our direct use of the DBQ (~2 \$/g) ligand also brought the monetary price of the materials down significantly compared to prior reports that required 2,5-diamino-1,4-benzoquinone (> 100 \$/g).

The facile benchtop synthesis was also applied to synthesize the MOFs materials featured in chapters 3 and 4. LiNiDBQ_{1.5} and LiFeDBQ_{1.5} were proposed as alternatives to the reported MOFs NBu₄MDBQ_{1.5} for two primary reasons. First, the tetrabutylammonium ion (NC₁₆H₃₆, 242 g/mol) has a very large mass that results in a reduction of theoretical gravimetric capacity to nearly one half of what LiNiDBQ_{1.5} or LiFeDBQ_{1.5} could obtain. Second, the tetrabutylammonium cation is bulky enough to completely fill the pores of NBu₄MDBQ_{1.5} materials. Facile ion diffusion through porous frameworks is considered beneficial to intercalation of MOFs electrodes materials. The non-porous nature of NBu₄FeDBQ_{1.5} led to poor ionic conductivity despite its unmatched electronic conductivity for three-dimensional MOFs materials. Our preliminary investigations of NBu₄M²⁺DBQ_{1.5} cathode materials confirmed this theory by having both lower gravimetric capacities and poor rate performance compared to Li⁺ charge balanced materials LiNiDBQ_{1.5} or LiFeDBQ_{1.5}. By rational materials design of LiM²⁺DBQ_{1.5} MOFs electrodes, batteries assembled are 100% charged in their pristine state. This is due to the reduction of benzoquinone required to intercalate Li⁺ ions. As mentioned previously, eliminating the first step charging requirement of Li-ion batteries is beneficial to practicality energy (resource) considerations.

Sustainability of resources used in rechargeable batteries was also covered in this dissertation. MOFs composed of earth abundant metals and renewable organics were demonstrated to have competitive energy storage capabilities compared to Co containing

TMOs. The scarcest resource used in Li-ion batteries today is the Li^+ ions in the cathodes and electrolytes. Chapters 5 and 6 contain our research to optimize and develop earth abundant Ca^{2+} electrolytes as a suitable replacement for Li^+ . This research was made possible by the recently reported results by Li et al, and Shyamsunder et al. They simultaneously reported on the first Ca^{2+} electrolyte that supports reversible electrochemical deposition of Ca and has voltage stability greater than 4.0 V ($\text{Ca}(\text{B}(\text{hfip})_4)_2$). When our research group began investigating this electrolyte there was currently no report of a battery featuring this electrolyte with a Ca metal anode. By the optimizations outlined in chapter 5, we were able to demonstrate a first of its kind 3.3 V $\text{FePO}_4|\text{Ca}$ battery with 120 mAh/g discharge capacity. Commercialized LiFePO_4 (3.5 V vs Li, 150 mAh/g) has higher energy density as a Li^+ host than as the Ca^{2+} host shown in our experiment. This limitation at the cathode can be easily overcome by the extreme gain in energy density at the Ca (1337 Ah/kg) anode versus the graphite (350 Ah/kg) used in current Li-ion batteries. This research exemplified the importance of optimizing all components in battery design including current collectors, electrolyte, electrodes, and battery hardware. Future work involving $\text{Ca}(\text{B}(\text{hfip})_4)_2$ electrolyte could take various forms. A noted weakness from this research was the low efficiency (<70%) and short lifetime of battery operation (11 cycles). Screening other electrodes or electrolyte additives are possible avenues to improve cycling life for Ca batteries. Improving electrode architecture could also be investigated by nanosizing active materials to increase surface area, varying conductive additives to improve electronic conductivity, or simply by improved homogenization techniques including but not limited to milling and calendaring.

$\text{Ca}(\text{B}(\text{hfip})_4)_2$ remains as the only high voltage option in the field of Ca electrolytes. As such its limitations need to be addressed. The low Coulombic efficiencies (~80%) and high overpotentials (~600 mV) disqualify this electrolyte as a suitable alternative to conventional Li^+ carbonate electrolytes that have facile deposition/stripping characteristics including virtually 100% efficiency and negligible overpotentials. As such, new Ca electrolytes were screened electrochemically in our lab. Based on previous success with Mg-FPB electrolyte and its weakly coordinating perfluorinated anion, the novel electrolyte Ca-FPB was synthesized, characterized, and tested electrochemically. In short, this electrolyte was found to have negligible overpotentials and similar Coulombic efficiencies to $\text{Ca}(\text{B}(\text{hfip})_4)_2$. Most significant was the vast improvement in high voltage stability from Ca-FPB that was greater than 5.0 V on all current collectors tested. This electrolyte also allowed for unprecedented stability in Ca|Ca symmetric cells and Ca| $\text{Fe}_2(\text{CN})_6$ full cells. The full cells could deliver ultra-high energy density (450 Wh/kg) greater than Li-ion batteries (>100 Wh/kg) for 50 stable cycles. The unprecedented stability for this Ca electrolyte was attributed to the strong chelating bonds and lack of acidic proton for the fluorinated pinacol moiety in comparison to monodentate hexafluoroisopropanol (hfip). Future work on Ca electrolytes will be vast due to infant nature of this field. Next steps will involve screening other weakly coordinating fluorinated anions for Ca electrolytes for additional beneficial electrolyte properties. A more detailed investigation of electrolyte decomposition products at electrodes surfaces is required to understand the fundamental properties and desirable attributes to engineer advanced Ca electrolytes with high efficiencies, low overpotentials, and high voltage stabilities.

The contents of this dissertation covered two seemingly disparate topics: (1) Metal organic frameworks (MOFs) as electrode active materials for Li batteries, and (2) Ca electrolytes for Ca batteries. The future work of this research will primarily require the marriage of these two efforts. The primary goal of this research was to achieve sustainability in energy storage devices that comprise earth abundant, renewable, and ethically sourced materials. At the same time, the highly competitive nature of energy storage research requires discoveries that overcome practical limitations to the current Li-ion battery architecture. Increasing energy density (Wh/kg, Wh/L), prolonging battery operation (cycling stability), reducing charging times, and minimizing safety concerns all must be prioritized.

In an ideal situation this dissertation would have featured a library of MOFs materials that had facile and highly reversible intercalation mechanisms for multivalent ions (Mg^{2+} , Ca^{2+} , Al^{3+} , etc.). This was in fact the original direction this research targeted. We projected the batteries tested would boast exceptionally high energy densities due the divalent nature of Mg^{2+} or Ca^{2+} . Also, the safety and resource issues associated with Li would be addressed .

Bringing MOFs and multivalent electrolytes together in batteries is much easier said than done. To date there have been extreme challenges with finding any suitable high voltage cathode materials for multivalent batteries. There is no report of a MOFs material that has enough electrochemical reversibility and energy density to combat state of the art Li-ion battery technology. Still, the state-of-the-art cathode for Mg^{2+} intercalation is Chevrel phase Mo_6S_8 (< 100 Wh/kg). There are no MOFs, excepting Prussian blue derivatives, that have been reported to reversibly intercalate Mg^{2+} or Ca^{2+} .

This seemingly inherent incompatibility was personally observed in attempts to extend the 2-5, dihydroxy-1,4-benzoquinone MOFs to multivalent batteries. Low capacities and poor efficiencies were often observed. Future work may involve a systematic experimental, and or computational screening of possible intercalation materials for multivalent batteries.

In conclusion, the work presented in this dissertation laid the groundwork for how to improve and develop metal organic framework electrodes and multivalent electrolytes. Sustainable, earth abundant materials were used with practical and scalable syntheses to prepare high performance electrodes and electrolytes that can compete with state-of-the-art technologies. The cathodes and electrolytes were shown to be competitive in terms of energy density, efficiency, and long-term cycling stability. There is still a great deal of work to be done in these burgeoning fields to develop MOFs electrodes and Ca electrolytes that can be paired together for high energy density batteries. Fundamental properties of MOFs such as porosity and conductivity need to be better understood regarding relation to desirable intercalation properties. A computational screening of potential multivalent cathodes may play a critical role in the discovery of optimal electrode materials for next generation multivalent battery technologies. At the same time, a better fundamental understanding on the limitations Ca electrolytes have in the deposition/stripping process and battery lifetimes needs to be had. Researchers are currently afforded great opportunities in this field due to the recently reported reversible Ca electrolytes. I expect this field to follow a path like other battery technologies. This means many advancements will likely be made incrementally as understanding increases.

There may be no “silver bullet” approach for a Ca battery that can directly replace Li-ion, but it doesn’t hurt to try.

APPENDICES

Appendix A. Tables and Figures

Table A-1. An overview of MOF cathodes to date.

Active Material	C _{th} mAh/g	C _{1st} - (C _{last}) mAh/g	Cycles- (Rate)	Retention- (Per Cycle) %	V vs Li- (Window) Volts	Reference
MIL-53(Fe)	210	80 (70)	50 (C/40)	87.50 (99.75)	~2.7 ca. (1.5-3.5)	1
MIL-68(Fe)	232	40 (32)	12 (C/50)	80.00 (98.33)	~3.0 V (1.5-3.8)	2
MIL-101(Fe)	107	65 (7)	30 (C/10)	10.77 (97.02)	~3.0 (2.0-3.5)	3
Cu-2,7-AQDC	300	147 (105)	50 (1C)	71.42 (99.42)	~2.5 (1.7-4.0)	4
Li ₂ DBQ	352	176 (138)	10 (C/3)	78.41 (97.84)	2.1 (1.5-3.5)	5
MIL-47	232	82 (82)	50 (C/12)	100.00 (100.0)	~3.0 (1.8-4.0)	6
Mn[Mn(CN) ₆]	176	197 (130)	10 (C/6.5)	66.00 (96.60)	~3.1 (2.0-4.2)	7
Mn(2,7-AQDC)	190	205 (190)	50 1 mA	93 99.86	2.6 1,3-4.5	8
CuTCNQ	255	214 (200)	50 C/5	93 99.87	3.3 2.0-4.0	9
LiNiDBQ _{1.5}	294	157 (128)	1000 (C/2.5)	82.00 (99.98)	2.3 (1.7-2.9)	This work
LiFeDBQ _{1.5}	397	241 (203)	500 C/5	80 (99.96)	2.5 (1.8-4.0)	This work

References for table A-1

1. Férey, G.; Millange, F.; Morcrette, M.; Serre, C.; Doublet, M.-L.; Grenèche, J.-M.; Tarascon, J.-M., Mixed-Valence Li/Fe-Based Metal–Organic Frameworks with Both Reversible Redox and Sorption Properties. *Angewandte Chemie International Edition* 2007, 46, 3259-3263.
2. Fateeva, A.; Horcajada, P.; Devic, T.; Serre, C.; Marrot, J.; Grenèche, J.-M.; Morcrette, M.; Tarascon, J.-M.; Maurin, G.; Férey, G., Synthesis, Structure, Characterization, and Redox Properties of the Porous MIL-68(Fe) Solid. *European Journal of Inorganic Chemistry* 2010, 2010, 3789-3794.
3. Shin, J.; Kim, M.; Cirera, J.; Chen, S.; Halder, G. J.; Yersak, T. A.; Paesani, F.; Cohen, S. M.; Meng, Y. S., MIL-101(Fe) as a lithium-ion battery electrode material: a relaxation and intercalation mechanism during lithium insertion. *Journal of Materials Chemistry A* 2015, 3, 4738-4744.
4. Zhang, Z.; Yoshikawa, H.; Awaga, K., Monitoring the Solid-State Electrochemistry of Cu(2,7-AQDC) (AQDC = Anthraquinone Dicarboxylate) in a Lithium Battery: Coexistence of Metal and Ligand Redox Activities in a Metal–Organic Framework. *Journal of the American Chemical Society* 2014, 136, 16112-16115.
5. Xiang, J.; Chang, C.; Li, M.; Wu, S.; Yuan, L.; Sun, J., A Novel Coordination Polymer as Positive Electrode Material for Lithium Ion Battery. *Cryst Growth Des* 2008, 8, 280-282.

6. Kaveevivitchai, W.; Jacobson, A. J., Exploration of vanadium benzenedicarboxylate as a cathode for rechargeable lithium batteries. *Journal of Power Sources* 2015, 278, 265-273.
7. Asakura, D.; Okubo, M.; Mizuno, Y.; Kudo, T.; Zhou, H.; Ikedo, K.; Mizokawa, T.; Okazawa, A.; Kojima, N., Fabrication of a Cyanide-Bridged Coordination Polymer Electrode for Enhanced Electrochemical Ion Storage Ability. *The Journal of Physical Chemistry C* 2012, 116, 8364-8369.
8. Zhang, Z.; Yoshikawa, H.; Awaga, K., Discovery of a “Bipolar Charging” Mechanism in the Solid-State Electrochemical Process of a Flexible Metal–Organic Framework. *Chemistry of Materials* 2016, 28, 1298-1303.

Table A-2. An overview of Ca electrolytes to date

Electrolyte	Coulombic Efficiency (%) (Scan Rate (mV/s))	Over-potential Plating, Stripping (mv)	Anodic Stability (V vs Ca)	Ionic Conductivity (mS/cm)	Reference
0.45M Ca(BF ₄) ₂ / PC:EC 100 °C	c.a. <40 (0.5)	-520, -420	3.5 (Al)	c.a. 5.5 25 °C	1
1.5M Ca(BH ₄) ₂ / THF	95 (25)	-200, 100	3.0 (Au)	n.a.	2
0.25M Ca[B(hfip) ₄] ₂ / DME	80 (80)	-220, 100	3.9 (Pt), >4.5 (Al)	8.3 23 °C	3
0.5M Ca[B(Ohfip) ₄] ₂ / DME	92 (25)	-400, 250	3.9 (Au), 4.2 (Al)	3.2	4
1.0M Ca(BF ₄) ₂ PC:EC	95 (25)	c.a. -700, 500	2.0 (Cu)	n.a.	5
Ca(BF ₄) ₂ EMIM OTF	56 (25)	-150, 1,500	2.8 (Cu)	n.a.	6
0.25M Ca[B(hfip) ₄] ₂ / G2	85 (100)	-20, 350	4.2 V (GC)	7.7	7
0.8M Ca-FPB / DME	72 (20)	-20, 5	4.5 V SS	8.2	This work

References for table 2.

1. Ponrouch, A.; Frontera, C.; Bardé, F.; Palacín, M. R. *Nature Materials* 2015, 15, 169.
2. Wang, D.; Gao, X.; Chen, Y.; Jin, L.; Kuss, C.; Bruce, P. G. *Nature Materials* 2017, 17, 16.
3. Li, Z.; Fuhr, O.; Fichtner, M.; Zhao-Karger, Z. *Energy Environ. Sci.* 2019, 12, 3496-3501.
4. Shyamsunder, A.; Blanc, L. E.; Assoud, A.; Nazar, L. F. *ACS Energy Lett.* 2019, 2271-2276.
5. Biria, S.; Pathreker, S.; Li, H.; Hosein, I. D. *ACS Applied Energy Materials* 2019, 2, 7738-7743.
6. Biria, S.; Pathreker, S.; Genier, F. S.; Li, H.; Hosein, I. D. *ACS Applied Energy Materials* 2020, 3, 2310-2314.
7. Nielson, K. V.; Luo, J.; Liu, T. L. *Batteries & Supercaps* 2020.

Appendix B. Copyright



Thank you for your order!

Dear Kevin Nielson,

Thank you for placing your order through Copyright Clearance Center's RightsLink® service.

Order Summary

Licensee:	Kevin Nielson
Order Date:	May 29, 2020
Order Number:	4838380442744
Publication:	Angewandte Chemie International Edition
Title:	Dawn of Calcium Batteries
Type of Use:	Dissertation/Thesis
Order Total:	0.00 USD

View or print complete [details](#) of your order and the publisher's terms and conditions.

Sincerely,

Copyright Clearance Center

Tel: [+1-855-239-3415](tel:+1-855-239-3415) / [+1-978-646-2777](tel:+1-978-646-2777)
customercare@copyright.com
<https://myaccount.copyright.com>



RightsLink®



RightsLink®



Home



Help



Email Support



Sign in



Create Account

A Strategic High Yield Synthesis of 2,5-Dihydroxy-1,4-benzoquinone Based MOFs

Author: Kevin V. Nielson, Liping Zhang, Qiang Zhang, et al

Publication: Inorganic Chemistry

Publisher: American Chemical Society

Date: Aug 1, 2019

Copyright © 2019, American Chemical Society



ACS Publications
Most Trusted. Most Cited. Most Read.

PERMISSION/LICENSE IS GRANTED FOR YOUR ORDER AT NO CHARGE

This type of permission/license, instead of the standard Terms & Conditions, is sent to you because no fee is being charged for your order. Please note the following:

- Permission is granted for your request in both print and electronic formats, and translations.
- If figures and/or tables were requested, they may be adapted or used in part.
- Please print this page for your records and send a copy of it to your publisher/graduate school.
- Appropriate credit for the requested material should be given as follows: "Reprinted (adapted) with permission from (COMPLETE REFERENCE CITATION). Copyright (YEAR) American Chemical Society." Insert appropriate information in place of the capitalized words.
- One-time permission is granted only for the use specified in your request. No additional uses are granted (such as derivative works or other editions). For any other uses, please submit a new request.

[BACK](#)
[CLOSE WINDOW](#)

Batteries & Supercaps

Chemistry Europe
European Chemical Societies Publishing

Article | [Full Access](#)

Optimizing Calcium Electrolytes by Solvent Manipulation for Calcium Batteries

Kevin V. Nielson, Dr. Jian Luo, Prof. Dr. T. Leo Liu

First published: 22 March 2020 | <https://doi.org/10.1002/batt.202000005>

[Check for Full Text](#)

Appendix C. Curriculum Vitae

Kevin V. NielsonEmail: nielkev2@isu.edu

Mobile: 2085693980

Address: 0300 Old Main Hill, Logan, UT 84322

Education

Utah State University

United States

Ph.D. in Chemistry

Spring 2021

Logan, Utah,

Idaho State University

Pocatello, ID

B.A. in Chemistry

May 2015

Research Experience

Utah State University

United States

Ph.D. Researcher

Logan, Utah,

August 2015 – August 2021

- Synthesized and characterized crystalline intercalation materials for rechargeable battery applications.
- Prepared and tested nonaqueous Mg and Ca electrolytes for high performance multivalent ion batteries.
- Performed SEM post analysis on components from coin cell batteries.
- Synthesized and tested organic electrode materials for Li metal batteries

Awards

Marjorie H. Gardner Teaching Excellence award 2018

Publications and Scholarly Work

1. He, S.; **Nielson, K.**; Luo, J.; Liu, T.*, “Recent Advances in MgCl₂ Based Electrolytes for Rechargeable Mg Batteries”, *Energy Storage Materials*. **2016**, 12, 001
2. Bi, Yujing.; Luo, J.; Hu, B.; He, S.; **Nielson, K.**; Liu, T. L.*, “Chemistry and Electrochemical Performance of Mg Electrolytes for Rechargeable Mg Batteries: A Study of Mg Powder Scavenger”, *ECS Trans.*, **2017**
3. Moss, J. B.; Zhang, L.; **Nielson, K. V.**; Bi, Y.; Wu, C.; Scheiner, S.; Liu, T. L. *, “Computational Insights into Mg-Cl Complex Electrolytes for Rechargeable Magnesium Batteries”, *Batteries & Supercaps* **2019**, 2, 792-800.
4. **Nielson, K. V.**; Zhang, L.; Zhang, Q.; Liu, T. L.*, “A Strategic High Yield Synthesis of 2,5-Dihydroxy-1,4-benzoquinone Based MOFs”, *Inorg. Chem.* **2019**, 58, 10756-10760.

5. **Nielson, K. V.**; Liu, T. L.*, “Dawn of Calcium Batteries” , *Angew. Chem. Int. Ed.* **2020**, 59, 3368-3370.
6. **Nielson, K. V.**; Luo, J.; Liu, T. L.*, “Optimizing Calcium Electrolytes by Solvent Manipulation for Ca Batteries” , *Batteries & Supercaps.* **2020**, <https://doi.org/10.1002/batt.202000005>

Presentations

1. Inorganic/organometallic research symposium at BYU 2017. Coordination polymer cathode materials for rechargeable Li-ion batteries.
2. MRS Spring 2019, Structure and Function of Novel Hybrid MOFs Electrode Materials.